ABSTRACT

Title of Dissertation: **COLLECTIVE EXCITATIONS AND EXCHANGE INSTABILITIES IN SEMICONDUCTOR QUANTUM WELLS**

Pablo Ignacio Tamborenea, Doctor of Philosophy, 1994

Dissertation directed by: Sankar Das Sarma, Professor of Physics

Department of Physics

Calculations of far-infrared optical absorption for $Al_xGa_{1-x}As$ perturbed parabolic quantum wells (PQW) with a magnetic field in the plane of the electron slab are presented within the linear response theory. We study two different types of samples. The first type consists of PQWs with controlled δ-planar perturbations. These samples were recently used in an experimental study aimed at measuring the magneto-roton dispersion relation of a three dimensional electron gas. We construct a magneto-plasmon dispersion relation and critically discuss whether the experimental results are consistent with the bulk magneto-roton picture originally invoked to understand the data. The second system is an asymmetric parabolic well; we study the absorption spectra as function of the areal density and compare them with recent experimental results.

We also study, employing the time-dependent local-density approximation (TDLDA), the elementary excitation energies and the associated inelastic light scattering spectra of a strongly coupled two-component plasma in a double quantum well system. We find, consistent with the results of a recent experimental Raman scattering study, that the intersubband spin density excitations tend to merge with the single particle excitations (i.e. the excitonic shift decreases monotonically) as the Fermi energy increases beyond the symmetric-antisymmetric energy gap. On the other hand, we predict that exchange-correlation induced many-body excitonic vertex correction may lead to an instability in the normal ground state of this system by suppressing the symmetric-antisymmetric gap at low but accessible ($\sim 0.7 \times 10^{11}\ cm^{-2}$) electron densities. We predict as a consequence a novel electronic phase transition to, possibly, a new many-body triplet excitonic liquid ground state.

Finally, we study the ferromagnetic transition in quasi-two-dimensional electron systems, employing the local-spin density (LSD) formalism. We conclude that the intersubband spin-density instability reported before in this dissertation does not correspond to the ferromagnetic transition. We also apply the LSD formalism to single square quantum wells and determine the dependence of the critical areal density on the well width.

COLLECTIVE EXCITATIONS
AND EXCHANGE INSTABILITIES
IN SEMICONDUCTOR QUANTUM WELLS

by

Pablo Ignacio Tamborenea

Dissertation submitted to the Faculty of the Graduate School
of The University of Maryland in partial fulfillment
of the requirements for the degree of
Doctor of Philosophy
1994

Advisory Committee:

Professor Sankar Das Sarma, Chairman/Advisor
Professor Howard D. Drew
Professor Arnold J. Glick
Professor Richard E. Prange
Associate Professor Neil Goldsman

DEDICATION

To the United States and Argentina,
which gave me the freedom and the means
to pursue knowledge
and devote my best efforts to Science.

ACKNOWLEDGEMENTS

I would like to thank my advisor, Professor Sankar Das Sarma, for his guidance and support, without which this dissertation would have not been possible. Professor Das Sarma not only suggested good projects to work on and showed me the right tools to attack them, but also taught me with his vivid example countless skills that a successful physicist should possess.

I am grateful to Professors H. D. Drew, A. J. Glick, R. E. Prange and N. Goldsman for agreeing to serve on my Advisory Committee. I am indebted to Professor H. D. Drew for explaining to me several aspects of the experiments on parabolic quantum wells and for very helpful discussions. I thank Dr. Khaled Karrai for useful discussions. I am also grateful to Drs. R. Decca and A. Pinczuk for providing us their data and for useful discussions, to Professor E. D. Williams for useful discusssions and for her help during the postdoc search, and to Dr. N. C. Bartelt for his assistance with computers. The financial support of the U.S. Army Research Office and the U.S. Office of Naval Research is gratefully acknowledged.

During my several years as a graduate student at Maryland I have been blessed with the company of many friends who more than made up for the absence of my loved ones at home. I start with the list (already quite long) of those who not only shared their leisure time with me but also taught me some physics. I thank Tetsuo Kawamura, the "quiet joker", for reducing my stress level during the writing of this dissertation, by making me laugh to tears with his rich repertoire of jokes and impersonations. On the other hand, he questioned me about my work and insisted that I should try to explain things in more clear, physical terms. With

Sanjay Kodiyalam I shared many discussions about my and his projects as well as cups of coffee after midnight. I am grateful to Ben Y-K. Hu for accompanying me to many concerts of the University of Maryland Orchestra, even though I know that his motives (and mine) were not always only auditory, but also visual. I also thank the other members of the "Das Sarma Institute", Charles Stafford, Rod Price, Eam Khor, Dongzi Liu, Chris Lanczycki, Jin Min Kim, Ioannis Marmorkos, Jose Senna, Vera Campos, Xincheng Xie, Subhash Ghaisas, Michael Ortalano, Euyheon Hwang, Roza Kotlyar, Peter Li, Herb Fertig and Song He, with whom I shared meals, movies, tennis or physics. My "spiritual advisor", Rodolfo Jalabert, helped me in many ways, from taking me to the driver's license test to advising me to join Professor Das Sarma's group.

Among those who did not teach me much physics but made my life more fun, thus increasing (probably) my productivity, I would like to thank Lubna Rana, for countless walks around campus and visits to her or my office during the long hours of work at night. I thank my most special (only!) mongolian friend, Chagarn Whan; I enjoyed many tennis games and talks about life and computers with him. Mahendra Verma inspired me with his love for the high principles of life, and Cesar Mancini balanced Mahendra's idealism with his practical and humorous viewpoints.

I thank Daniel Martinez for our chats back in Buenos Aires that motivated me to come to the U.S. for a Ph.D., and my family for supporting me in spite of the painful separation. Finally, a very special thank goes to Peiling Wang for her loving care and support. All the happy moments that we shared added another dimension to these years of physics and friends at Maryland.

Table of Contents

List of Figures

CHAPTER 1

Introduction

This chapter is divided into several short introductory sections. In Sections 1.1, 1.2, and 1.3 the systems studied in this dissertation are introduced, sometimes in the form of brief reviews of the evolution of the subjects up to the point in which our work started. In Section 1.4 the foundations of the main calculational method employed in this dissertation, i.e. the density-functional theory, are briefly discussed. In Section 1.5 an outline of the dissertation is given.

1.1 Semiconductor microstructures

The quantum mechanical theory of the electron gas is one of the most interesting and intricate subjects of modern physics. Even in the simplest situation of an homogeneous electron gas, all the known theoretical and numerical treatments lead only to approximate results for most of its basic properties. On the experimental side, metals are good systems where electron-interaction effects can be studied, but many of the interesting aspects of the electron gas, which occur at low densities, cannot be observed there. In doped bulk semiconductors lower electron densities can be obtained, but the strong interactions between the electrons and the positively charged donor impurities mask the effects coming from electron-electron interactions. The advent of modulation doped semi-

conductor microstructures, where a confined electron gas with greatly reduced electron-impurity interactions can be realized, lead to an enormous progress in our understanding of the consequences of electron-electron interactions and to the discovery of unexpected quantum phenomena in the last two decades.

Semiconductor microstructures are artificially created systems in which an electron gas can be confined within length scales of the order of tens or hundreds of angstroms. These semiconductor systems are often called "mesoscopic" because the confinement length is in between the typical interatomic distances and the macroscopic sizes of bulk materials. Depending on whether the confinement is applied in one, two, or three dimensions, the resulting low-dimensional structures are called, respectively, quantum wells (quasi-2D), quantum wires (quasi-1D), or quantum dots (quasi-0D). The fabrication of such systems has become possible in recent years thanks to the advances in crystal-growth techniques like molecular-beam epitaxy (MBE) [1, 2]. These techniques allow the growth of semiconductor crystals in a layer-by-layer manner, leading to virtually perfect crystal structures. To produce a quasi-2D electron gas, a semiconductor quantum well is grown, consisting of a slab of a given semiconducting material (for example, GaAs), surrounded by slabs of another semiconducting material (for example, $Al_xGa_{1-x}As$) with a larger energy gap between its valence and conduction bands. A gas of free electrons is added into this quantum well by doping the sample with negative donors, for example Si atoms, in atomic layers placed outside the well region occupied by electrons. This technique, called modulation doping, which was first applied by Dingle et al. and Störmer to AlGaAs heterostructures [3], allowed the achievement of very high electron mobilities by eliminating electron-impurity scattering, and thereby opened the possibility to experimentally studying purely

electron-electron interaction effects in low-dimensional systems.

1.2 Parabolic quantum wells

In 1987, Gossard and Halperin [4] indicated the possibility of constructing a quasi-2D electron layer sufficiently thick and uniform that would permit the observation of electron-electron interaction effects predicted to occur in the three-dimensional jellium model. A simple harmonic potential $V(z) = Az^2$ could be used to that effect, since it mimics a uniform slab of positive charge with density $n_0 = A\epsilon/2\pi e^2$, as can be seen by solving the one-dimensional Poisson equation $V''(z) = \frac{4\pi e^2}{\epsilon} n_0$ (ϵ is the static dielectric constant of the host semiconductor. The harmonic oscillator frequency in $V(z) = \frac{1}{2} m^* \omega_0^2 z^2$ is given by $\omega_0 = \sqrt{4\pi e^2 n_0 / m^* \epsilon}$, where m^* is the electron effective mass). An electron gas introduced in such parabolic potential rearranges itself to acquire the uniform density n_0 in order to screen the fictitious positive charge. Those authors suggested that this idea could be implemented employing a semiconductor alloy like $Al_xGa_{1-x}As$, where the conduction-band edge can be tailored by varying the concentration x of aluminum during the layer-by-layer growth of the crystal with MBE. A quadratic variation of x produces a parabolic confining potential in the effective mass approximation, and, therefore, the desired one-dimensional parabolic well. Shortly after being proposed, parabolic quantum well (PQW) structures were produced by Gossard and co-workers [5], and by Shayegan and co-workers [6].

The long-wavelength optical and magneto-optical absorption properties of parabolic quantum wells turned out to be unexpectedly simple. The single-particle energy levels of independent electrons placed in a uniform magnetic field B are given by $E_{nk} = (n + \frac{1}{2})\hbar\omega_c$, where $\omega_c = \frac{eB}{mc}$ is the cyclotron frequency, and

$n = 0, 1, \ldots$ labels the different Landau levels. Cyclotron resonance occurs when a homogeneous radiation field of frequency $\omega = \omega_c$ is applied, inducing transitions between Landau levels. In 1961, Kohn [7] showed that cyclotron resonance in a translationally invariant system is not altered by electron-electron interactions, and the resonant frequency is still the bare cyclotron frequency ω_c. In 1989, Brey, Johnson, and Halperin [8] proved the so-called generalized Kohn's theorem, which also states that electron-electron interactions do not affect long-wavelength optical absorption, but, in this case, in an electron gas in a parabolic well in the presence of an arbitrary uniform magnetic field. Their theorem has been extended to systems confined in two or three dimensions by parabolic potentials, with arbitrary values of the harmonic oscillator frequencies in different directions [9]. The generalized Kohn's theorem and its extensions tell us that in parabolically confined electron systems in the presence of arbitrary magnetic fields, long wavelength optical absorption frequencies are equal to those of a *single* electron under the same external potential and magnetic field. Das Sarma explains this rather surprising result [10]: "The essence of Kohn's theorem is the separability of the system Hamiltonian into two distinct parts, one depending purely on the center of mass coordinates of the system and the other depending purely on the relative (inter-electron) coordinates of the system. The electron-electron interaction part of the Hamiltonian, by definition, depends on the relative coordinates while any long wavelength electromagnetic radiation obviously couples only to the center of mass part of the Hamiltonian. Therefore, the long wavelength optical absorption frequency is unaffected by electron-electron interaction effects. In a translationally invariant system the separation of the Hamiltonian into a center of mass and a relative coordinate part is obvious. It turns out that a parabolic

potential is the only possible form for an external potential which preserves this separability of the system Hamiltonian."

After a complete understanding of the long wavelength excitations of electron systems confined in parabolic potentials was obtained with the aid of the generalized Kohn's theorem, interest shifted to confining potentials with quasi-parabolic shapes. A simple and interesting example is that of an asymmetric parabolic quantum well (APQW), that is, a well consisting in two half parabolas of different curvature [11, 12, 13, 14, 15]. Since the parabolic potential mimics a uniform positive background, an APQW can be thought of as a bimetallic jellium system, where the electron gas adopts a nonuniform density. The focus of the study of APQW has been mainly on the transition of collective properties from 2D to 3D behavior. Ying et al. [11] studied experimentally collective cyclotron resonance in the Voigt geometry (with a magnetic field in the plane of the confined electron gas), as function of the electron slab width (or equivalently the electronic areal density N_S). Their far-infrared (FIR) optical spectra show a crossover from a *quantum regime* for $N_S/n_0 \ll l_0$ to a *classical regime* for $N_S/n_0 \gg l_0$, where $l_0 = \sqrt{\hbar c/eB}$ is the magnetic length. The inhomogeneous electron gas is identified as three-dimensional when the absorption spectrum shows two resonances, corresponding to the two "Kohn modes" of the parabolic half-potentials. This condition is found to be satisfied when the electron slab is wide enough to accommodate a full second Landau orbit on each half of the well. Yuh et al. [12], on the other hand, studied theoretically and experimentally the evolution of excitations of this quasi-2D electron gas into surface plasmons as the system widens, in the absence of external magnetic field.

The original idea that motivated the construction of parabolic quantum wells

was to realize a quasi-three-dimensional electron gas as an approximation to the ideal three-dimensional jellium model. The first concrete application of PQWs to the study of a 3D phenomenon was the recent experimental measurement of the bulk magneto-plasmon dispersion relation by Karrai et al. [16]. The bulk magneto-plasmon dispersion calculated in the single-mode approximation [16] for wavevector perpendicular to the magnetic field, exhibits a minimum or *magneto-roton* feature at $q \simeq 2/l_0$. This feature is analogous to the magneto-roton minimum found in both the inter- and intra-Landau-level collective excitations of a two-dimensional fractional quantum-Hall system [17]. Since in perfect PQW the only modes excited in FIR experiments are the center-of-mass Kohn modes, which have $q = 0$, Karrai et al. employed PQWs with small superimposed perturbations to be able to excite modes with high values of q and thereby measure the magneto-plasmon dispersion curve. The perturbations to the underlying parabolic potential were made by inserting thin layers of higher (or lower) concentration of Al during the growth of the parabolic well sample. Two types of samples were studied: in one type a single narrow Al spike at the center of the parabola was introduced, and the other type had a periodic array of such Al spikes with period a. The FIR spectra measured with a magnetic field applied in the plane of the electron gas (Voigt geometry) showed a resonance corresponding to the usual Kohn mode with frequency $\omega_K = \sqrt{\omega_0^2 + \omega_c^2}$, and one or more satellite resonances. The interpretation of these satellite resonances was made as follows by Drew et al. [16]: "In the case of a single Al spike the satellites correspond to the excitation of dimensional modes in which the thickness of the electron slab corresponds to an integer number n of half wavelengths of the magneto-plasma wave. Therefore, the wavevector of the excited magneto-plasmon depends on the

well width as $q = 2\pi n/W$. This leads to a shifting of the frequency of these satellite modes [...] For the case of symmetric filling of the well only even n leads to a finite dipole moment and optical absorption. For the grating samples magneto-plasmons of wave vector $q = 2\pi/a$ are excited in addition to the dimensional modes." Combining the data from different samples, magnetic fields and densities N_S, a magneto-plasmon dispersion relation was constructed which shows a minimum at $q \simeq 2/l_0$, in agreement with the 3D magneto-plasmon calculation. This experiment constitutes the first observation of the three-dimensional magneto-roton minimum. However, as pointed out by the authors, there is a quantitative discrepancy in the theoretical and experimental frequencies of the resonances, which indicates that the applicability of the three-dimensional theory to the quasi-3D experiment may not be complete.

1.3 Intersubband excitations in quasi-2D electron systems

The single-particle electronic energy levels in a quantum well are discretized into subbands $E_n(\mathbf{k}) = \varepsilon_n + \frac{\hbar^2 k^2}{2m^*}$, where n is the subband index and $\mathbf{k}$ is the momentum in the plane perpendicular to the confined dimension. It is often adequate to describe the electronic properties of semiconductor quantum wells in terms of an *effective* single-particle, for which the energy levels ε_n are not just the bare-well eigenenergies but rather the levels of a potential well renormalized by the many-body interactions. The subband structure taking into account many-body effects of numerous semiconductor systems (like Si inversion and accumulation layers, GaAs-based semiconductor heterojunctions and quantum wells, etc.) has been extensively studied in the past two decades [18, 19]. We only mention here that the density-functional theory (see Section 1.4) in its local-density ap-

proximation (LDA) form has been a very successful tool to investigate subband structures since it was applied for the first time to space-charge layers by Ando [20]. The study of GaAs-based systems employing the LDA started with the work of Stern and Das Sarma [21].

The subband structure gives rise to excitations of the electron that can be classified as *intersubband* and *intrasubband* transitions (this classification is strictly valid only for symmetric quantum confinement [73]). As we will see in Chapter 2, the excitation of an *intersubband* transitions in, for example, an optical absorption experiment, requires a photon energy which is not equal to the energy difference between the final and original subband. The many-body corrections that affect the resonance energy of intersubband transitions can be classified into two types. The first type is due to the dynamic screening of the external radiation field, which is operative through the direct Coulomb interaction, and is known as the depolarization shift [22, 23, 24]. This type of correction is included when the dynamic response is calculated in the random-phase approximation (RPA) [25, 26]. According to Ando, Fowler, and Stern [18]: "Physically the depolarization effect arises because each electron feels a field which is different from the external field by the mean Hartree field of other electrons polarized by the external field." Since the depolarization shift is due to an effective reduction of the external electric field, it is always positive. The second type of correction is motivated by the same authors in the following way: "As has frequently been mentioned, however, the Hartree approximation overestimates the Coulomb repulsive force of other electrons, and the exchange-correlation effect greatly reduces the effective repulsive potential. Therefore we expect that the exchange-correlation effect on the depolarization effect greatly reduces the shift of the resonance energy." This

negative correction is usually referred to as the excitonic shift, because it reflects the attractive interaction between the electron excited to the higher subband and the hole left in the original subband. In diagrammatic perturbation theory this effect is accounted for by the vertex corrections to the irreducible polarizability function [27], when it is given by, for example, the ladder-bubble diagrams [25].

Resonant inelastic light-scattering spectroscopy is an ideal experimental technique to study many-body effects in confined electron systems since it can provide detailed information on both the energy and wave-vector of the collective excitations (see Chapter 5). Also, by changing the polarization configuration of the experiment, it can measure the energy of *charge-density* or *spin-density excitations*, from which the many-body corrections introduced above can be extracted.

In GaAs, where the electron effective mass is small and the dielectric constant is large, the effective Bohr radius $a^* = \hbar^2\epsilon/me^2 \approx 100$Å is large (compared to that of Si, for example), and therefore, the dimensionless inter-particle distance parameter $r_s = r_0/a^*$ is small for the usual electron densities of $n \sim 10^{16}\, cm^3$. For this reason, the RPA is often a good approximation for GaAs systems, and for many years exchange-correlation corrections where thought to be negligible in this context [28, 29]. However, in recent years a number of interesting effects associated to exchange-correlation corrections were discovered. We mention only a few of these developments which are directly related to our work. In 1989, Pinczuk et al. [30] reported the first observation of large exchange interactions through inelastic light-scattering measurements in GaAs quantum wells. More recently, Das Sarma and Marmorkos [27] predicted that in square and parabolic wells there is a critical density below which the excitonic vertex corrections overcome the Hartree depolarization shift, and therefore the charge-density-excitation

energy becomes lower than the single-particle-excitation energy ($= \varepsilon_{n'} - \varepsilon_n$, if n and n' are the initial and final subbands, respectively). This effect was very recently experimentally observed in inelastic light-scattering experiments [31]. Another recent experimental study [32] revealed that the excitonic vertex corrections abruptly vanish in coupled double-quantum wells as N_S increases beyond occupancy of the two lowest subbands is attained [33]. In this dissertation we predict a new interesting exchange-correlation effect in double-quantum wells, namely, an enhancement of vertex corrections at low density N_S, so strong that it leads to the vanishing of the lowest intersubband spin-density excitation energy [34] (see Chapter 7). The softening of the spin-density mode indicates the possibility of an instability in the electron gas in double quantum wells and the existence of a phase transition to a novel ground-state. Inelastic light-scattering experiments to observe this new phenomenon are currently under way [35].

1.4 Density-functional theory

There are several formulations of many-body quantum mechanics that can be applied to the study of electronic properties of semiconductor microstructures. One alternative method to the powerful but often intractable Green's function technique [25] to study inhomogeneous many-particle systems is the density-functional theory. The precursors of this theory are the early attempts of Thomas and Fermi [36] to express the ground-state energy in terms of the density $n(\mathbf{r})$ alone. This kind of approach, where the density plays the central role, flourished after Hohenberg and Kohn [37] proved that an exact representation of the ground-state properties in terms of the ground-state energy alone is possible, at least in principle. They showed that for a collection of particles under the

influence of an external potential $v(\mathbf{r})$ and their mutual Coulomb interaction, the functional

$$E_v[n] \equiv \int d^3r\, v(\mathbf{r})\, n(\mathbf{r}) + F[n] \tag{1.1}$$

(where $F[n] = \langle \Psi | T + U | \Psi \rangle$ is a *universal* functional, independent of $v(\mathbf{r})$) assumes its minimum value for the correct ground-state density, and this value equals the ground-state energy. Therefore, the problem reduces to finding the universal functional $F[n]$ characteristic of a system with Coulomb interparticle interactions. Unfortunately, the functional $F[n]$ is not known and one has to resort to some approximation scheme. Kohn and Sham [38, 39] introduced a widely used method, the local-density approximation (LDA), which applies to systems with slowly varying density. They wrote the functional $F[n]$ as

$$F[n] \equiv \frac{1}{2} \int d^3r' d^3r \frac{n(\mathbf{r}) n(\mathbf{r}')}{|\mathbf{r} - \mathbf{r}'|} + T[n] + E_{xc}[n], \tag{1.2}$$

where $T[n]$ is the kinetic energy of a noninteracting system with density $n(\mathbf{r})$, and $E_{xc}[n]$ is, by definition, the exchange-correlation energy of the interacting system with density $n(\mathbf{r})$. Next they assumed that for a system of slowly varying density $n(\mathbf{r})$, $E_{xc}[n]$ could be written (like for an uniform system) as

$$E_{xc}[n] = \int d^3r\, \epsilon_{xc}(n(\mathbf{r})) n(\mathbf{r}), \tag{1.3}$$

where $\epsilon_{xc}(n)$ is the exchange-correlation energy per electron of a uniform electron gas of density n. By minimizing $E_v[n]$ in Eq. (1.1) with respect to $n(\mathbf{r})$, they found that the interacting problem simplifies to one of noninteracting electrons, subject to the effective potential

$$v_{\text{eff}}(\mathbf{r}) = v(\mathbf{r}) + \varphi(\mathbf{r}) + \mu_{xc}(n), \tag{1.4}$$

where

$$\varphi(\mathbf{r}) = \int d^3r' \frac{n(\mathbf{r}')}{|\mathbf{r} - \mathbf{r}'|} \tag{1.5}$$

and

$$\mu_{xc}(n) = \frac{d[n\,\epsilon_{xc}(n)]}{dn}. \tag{1.6}$$

Therefore, in LDA one only needs to solve the one-particle Schrödinger equation (the "Kohn-Sham" equation)

$$\left[-\frac{1}{2}\nabla^2 + v_{\text{eff}}(\mathbf{r})\right] \varphi_i(\mathbf{r}) = \epsilon_i \varphi_i(\mathbf{r}) \tag{1.7}$$

coupled to Eqs. (1.4,1.5,1.6) and $n(\mathbf{r}) = \sum_{i=1}^{N} |\varphi_i(\mathbf{r})|^2$, where N is the number of electrons.

The LDA treatment was adapted by Ando [40] to time-dependent situations, to calculate the optical absorption spectrum of the quasi-2D dimensional electron gas. This time-dependent local-density approximation (TDLDA) theory is equivalent to including vertex corrections in the irreducible polarizability function, but assuming an energy and wave-vector independent proper vertex part [40, 27]. This approximation for the vertex correction is consistent with the exchange-correlation self-energy shift of the subbands when it is calculated self-consistently in LDA. In this dissertation we adopt the density-functional approach in the LDA to study the ground-state properties of the electron gas in semiconductor microstructures, and the TDLDA to study the dynamic response functions which describe the optical absorption and light-scattering spectra. The applicability of the LDA to our problem and its limitations are discussed in Appendix B. Finally, we mention that the density-functional theory has been extended to many situations not considered in the original formulation of Hohenberg, Kohn

and Sham, like systems with degenerate ground-states, finite temperatures, relativistic systems, spin-polarized ground-states, etc. For further details and extensions of the original formulation of density-functional theory, we refer the reader to the vast literature on the subject. Recent reviews are given in Refs. [41, 42].

1.5 Outline of dissertation

In Chapter 2 we present the theory of intersubband optical absorption in semiconductor microstructures. In Section 2.1 we describe in detail the LDA calculation of energy subbands without magnetic fields and in Section 2.3 we cover the Voigt geometry problem, in which a magnetic field is applied in the plane of the electron slab. In Sections 2.2 and 2.4 the time-dependent local-density approximation (TDLDA) theory is presented, in the cases of no applied magnetic field and of the Voigt geometry, respectively.

In Chapter 3 we study, employing the theories developed in Chapter 2, the collective excitations and FIR optical absorption spectra of asymmetric parabolic wells [14, 15]. We study FIR absorption spectra in the Voigt geometry as function of the electron density N_S, which in quasi-parabolic systems is equivalent to saying as function of the width of the electron slab. We compare our results with recent experimental measurements [11] and obtain good agreement in the limits of low and high N_S (thin and thick electron slabs), but quantitative disagreement in the evolution of the spectra in the intermediate N_S range. Possible reasons for this disagreement are suggested. We also present introductory results for perfect parabolic wells, which serve as a starting point for the study of imperfect or *quasi*-parabolic wells.

In Chapter 4, a study of magneto-optical spectra of parabolic samples with Al-

spike perturbations in the Voigt geometry is presented [15]. We study two types of samples: one type has only one perturbation in the center and the other type has a periodic array of perturbations, similar to a superlattice structure. The main purpose of the study is to analyze the interpretation made of recent magneto-optical absorption experiments [16], where the bulk magneto-plasmon dispersion relation was measured employing wide parabolic quantum wells. It is found that for the systems under study, confined intersubband plasmons can be related to bulk collective modes following a well defined procedure, that generalizes an earlier study of the relation between excitations in confined systems to excitations in bulk systems in the absence of magnetic fields [43].

In Chapter 5 we give a brief review of the theory of resonant inelastic-light-scattering experiments. We outline the calculation of the linear response functions that describe the electron-electron interaction many-body effects operative in electronic Raman scattering. This theory is applied to coupled double-quantum wells in Chapters 6 and 7.

In Chapter 6, we study, within the TDLDA, the absence of the lowest intersubband spin-density excitations at high density N_S recently discovered in coupled double-quantum well systems in resonant inelastic light-scattering experiments [33]. Our calculations show that the excitonic vertex corrections monotonically decrease with increasing N_S, in agreement with the experimental results. However, the abrupt disappearance of vertex corrections at a finite value of the subband occupancy parameter $\eta \equiv \Delta_{SAS}/E_F$, where $\Delta_{SAS} = \varepsilon_2 - \varepsilon_1$ is the symmetric-antisymmetric energy gap and E_F is the Fermi energy, is not obtained. It is pointed out that the limitations of the theoretical approximation scheme are the possible reasons for this disagreement, although additional

experimental evidence may also be needed to resolve this issue.

In Chapter 7 we predict a novel instability of the electron gas confined in coupled double-quantum wells, due to the vanishing of the intersubband spin-density excitation energy in an accessible range of N_S [34]. The calculations that indicate this instability are performed in the TDLDA. Resonant inelastic light-scattering experiments are suggested to observe the approach to the instability from the high N_S side.

In Chapter 8 we introduce the generalization of LDA that takes into account the possibility of electron spin polarization, namely, the local-spin-density (LSD) approximation. LSD is applied to coupled double-quantum wells, and it is found that the ground-state suffers a ferromagnetic transition, favoring a completely spin-polarized state at low N_S. The ferromagnetic critical density is at least an order of magnitude smaller than the critical density of the spin-density instability mentioned above, which rules out an identification between these two instabilities. The same ferromagnetic transition is found in single square wells, and its well-width versus N_S phase diagram is calculated.

Appendix A contains a compendium of the exchange-correlation potentials used in the dissertation, and Appendix B discusses the limitations and applicability of the local-density approximation.

CHAPTER 2

Theory of intersubband optical absorption

In this chapter we describe the theory of optical absorption due to intersubband collective excitations in the quasi-two dimensional (2D) electron gas formed in remotely doped semiconductor heterostructures. I will present the theory of optical absorption in semiconductor wells both without an external magnetic field and in the so-called Voigt geometry, that is, with a static external magnetic field applied in the plane of the electron gas (perpendicular to the growth direction). This theory will be applied in the next two chapters to imperfect parabolic wells, where we will be interested mostly in the Voigt geometry. Our interest in the Voigt geometry problem arises from recent experimental studies, which will be explained in detail in the next chapters. However, for completeness, and to compare with the Voigt geometry results, we will also study the imperfect parabolic wells without any external magnetic field. Also, the electronic structure of quantum wells (an intermediate result necessary in the optical absorption calculation) without magnetic field will be employed throughout Chapters 6 and 7 in the calculations of resonant inelastic light-scattering spectra and the dispersion relations of the intersubband collective modes of coupled double-quantum wells.

The self-consistent framework of the Hohenberg-Kohn-Sham local-density-approximation (LDA) that we describe in this chapter is the most widely used

technique for calculating intersubband response in confined semiconductor structures. This method consists of two steps. First, the subband energies and wavefunctions are calculated self-consistently by solving the single-particle Schrodinger-like Kohn-Sham equation. In this equation, the potential is separated into a Hartree term due to the electrostatic potential of the total electron density (which is just the solution of Poisson's equation), and an exchange-correlation term treated within the local-density approximation. Then, a linear response calculation using the self-consistent LDA subband energies and wavefunctions can be performed to obtain the intersubband response functions, whose poles give the intersubband collective modes of the system. This self-consistently coupled linear-response calculation that we will describe in detail in Section 2.2 and 2.4 is sometimes referred to as the time-dependent local-density approximation (TDLDA) in the same spirit of the random-phase approximation (RPA) being the time-dependent Hartree approximation.

The problems with no applied magnetic field and magnetic field applied in the plane of the electron gas are similar to each other in the sense that the single particle energies form subbands and are non-degenerate unlike the case of a 2D electron gas in a perpendicular magnetic field (the geometry of the Quantum Hall effect). However, they have important differences in terms of the theoretical description and their physical properties. The in-plane magnetic field considerably complicates the theoretical treatment (especially its numerical implementation) because the z-dependent part of the Kohn-Sham equation (the effective single particle Schrödinger equation) depends in this case on a component of the in-plane wavevector of the electron. Therefore, in the Voigt geometry, the electric subbands acquire a non-parabolic dispersion. These technical differences will be

described in this chapter, where we present the formalism for the zero magnetic field and the in-plane magnetic field cases. There are two physical consequences of the application of an in-plane magnetic field that are relevant to the experimental systems that we study in the next two chapters with the formalism introduced here. The first has to do with the fact that to induce intersubband transitions the oscillating electric field must have a component along the confinement direction. Therefore, in an absorption experiment in the absence of a magnetic field it would be necessary to apply the incident radiation at an angle far from normal incidence or to use an external grating. On the other hand, normal incidence can be used to induce intersubband transition if an in-plane magnetic field is applied, because it introduces a Lorentz force perpendicular to the layer and therefore a non-zero component of the local oscillating electric field in the confined dimension. Second, and perhaps more importantly, an in-plane applied magnetic field allows control of the spatial extent of the electron wave function in the direction of confinement, which is useful in studying the transition from two- to three-dimensionality of the confined electron gas.

Throughout this dissertation we work in the effective mass approximation to account for the presence of the underlying periodic lattice, and take the effective mass to be a constant equal to the bare GaAs effective mass, $0.067\, m_e$. We also assume the static dielectric constant across the semiconductor structure to be constant.

2.1 Self-consistent electronic structure without magnetic field

In this section we begin the study of the electronic structure of quasi-2D electron systems. Here we treat the case of no applied magnetic field and in

Section 2.3 we cover the situation with a magnetic field perpendicular to the growth direction. The goal is to calculate energy levels and wave functions of electrons in modulation doped semiconductor quantum wells, taking into account the interaction with other electrons in an average sense, and going beyond the Hartree approximation to include additional many-body effects. As discussed in Section 1.4, we achieve this by employing the self-consistent approach based on the density functional theory of Hohenberg, Kohn and Sham, within the local-density approximation [37, 38, 39, 41]. In most of this dissertation we perform spin-unpolarized calculations, i.e., we use an exchange-correlation potential μ_{xc} which has no explicit spin dependence. In Chapter 8 we remove this constraint and perform spin-polarized calculations to study the ferromagnetic transition in the confined electron gas. There we find that the quasi-2D electron gas could become spin-polarized, but only at densities lower than the ones studied in the rest of this dissertation, which justifies the usage of the unpolarized theory in the rest of our work. A number of self-consistent electronic structure studies of quasi-2D electron systems without magnetic field can be found in the literature. For work on semiconductor inversion and accumulation layers see Ref. [18] and references therein, for $Al_xGa_{1-x}As$ based heterostructures and quantum wells see Refs. [28, 21, 19], and for an introduction to the subject, mostly within the Hartree approximation, see Ref. [2].

Let us choose a coordinate system such that the z-axis is along the direction of confinement of the electrons, or the growth direction. The effective single-particle Schrödinger equation or Kohn-Sham equation for our system reads

$$\left(-\frac{\hbar^2}{2m^*}\nabla^2 + V_{EFF}(z)\right)\Psi(\boldsymbol{x}) = E\Psi(\boldsymbol{x}), \tag{2.1}$$

where we have assumed that the effective mass m^* is constant across the well,

which has been shown to be a good approximation in parabolic wells [6, 44]. The self-consistent effective potential $V_{EFF}(z)$ is given below. The in-plane (x-y) and z-dependences can be separated, and due to the assumed translational invariance in the x-y plane (the localized donor charges are assumed to be smeared out in the x-y plane), the eigenenergies and wavefunctions become

$$E_{nk_xk_y} = \varepsilon_n + \frac{\hbar^2 k^2}{2m^*}, \tag{2.2}$$

$$\Psi_{nk_xk_y}(\boldsymbol{x}) = \frac{1}{\sqrt{A}} e^{i(k_x x + k_y y)} \varphi_n(z). \tag{2.3}$$

In this expression, A is the sample area, $\boldsymbol{k} = (k_x, k_y)$ is the in-plane wave vector of the electron, and ε_n and $\varphi_n(z)$ are the solution to the one-dimensional Kohn-Sham equation

$$\left(-\frac{\hbar^2}{2m^*} \frac{d^2}{dz^2} + V_{EFF}(z) \right) \varphi_n(z) = \varepsilon_n \varphi_n(z). \tag{2.4}$$

The effective single-particle potential

$$V_{EFF}(z) = V_{CONF}(z) + V_H(z) + V_{XC}(z) \tag{2.5}$$

contains the confining potential of the bare quantum well $V_{CONF}(z)$, and the self-consistent Hartree and exchange-correlation potentials, $V_H(z)$ and $V_{XC}(z)$, respectively. The Hartree potential takes into account the average electrostatic interaction due to the rest of the electrons and the positively charged donor ions, and is given by the Poisson equation

$$\frac{d^2 V_H(z)}{dz^2} = -\frac{4\pi e^2}{\epsilon} [n(z) - N_D(z)], \tag{2.6}$$

where ϵ is the static dielectric constant of GaAs, $n(z)$ is the electron density, and $N_D(z)$ is the density of positive donor charge. We assume the positive donors to be located far removed from the quantum well, so that they enter in the

solution of the Poisson equation only through the boundary conditions (i.e., the electrostatic force far from the well is zero due to the charge neutrality of the system of electrons in the well plus the positive donor charges). If Eq. (2.6) is integrated twice one obtains

$$V_H(z) = -\frac{4\pi e^2}{\epsilon}\left(\int_0^z dz'(z-z')n(z') + z\int_{-\infty}^0 dz' n(z') - \frac{N_S}{2}z\right). \tag{2.7}$$

As mentioned in Section 1.4 and earlier in this chapter, we include many-body effects beyond the Hartree approximation by means of the density functional theory in the local-density approximation. For the exchange-correlation potential, we have used the parametrizations due to Hedin and Lundqvist [45], and to Ceperley and Alder [46]. Hedin and Lundqvist's expression is given by

$$V_{XC}(z) = -\left(\frac{9\pi}{4}\right)^{1/3}\left(\frac{2}{\pi r_s}\right) Ry^*\left(1 + 0.0368\, r_s \ln\left(1 + \frac{21}{r_s}\right)\right), \tag{2.8}$$

where

$$r_s = r_s(z) \equiv r_0/a^*, \qquad \text{and} \qquad r_0 \equiv \left(\frac{4\pi}{3}n(z)\right)^{-1/3}, \tag{2.9}$$

and the potential due to Ceperley and Alder is given by

$$V_{XC}(z) = \frac{-1.2145}{r_s} + \gamma\,\frac{\left(1 + \frac{7}{6}\beta_1\sqrt{r_s} + \frac{4}{3}\beta_2 r_s\right)}{\left(1 + \beta_1\sqrt{r_s} + \beta_2 r_s\right)^2}, \tag{2.10}$$

where $\gamma = -0.1471$, $\beta_1 = 1.1581$, and $\beta_2 = 0.3446$. Once the subband energies ε_n and wave functions $\varphi_n(z)$ are known, the z-dependent electron density can be calculated as

$$n(z) = g_s \sum_{n,\boldsymbol{k}} f(E_{nk_xk_y})|\Psi_{nk_xk_y}(\boldsymbol{x})|^2, \tag{2.11}$$

where the factor g_s accounts for the spin degeneracy and

$$f(E) = \frac{1}{e^{(E-\mu)/k_BT} + 1} \tag{2.12}$$

is the Fermi-Dirac distribution function, and we introduced the Boltzmann constant k_B, the absolute temperature T, and the chemical potential μ. The density can be rewritten as

$$n(z) = \sum_n N_n |\varphi_n(z)|^2, \tag{2.13}$$

where the subband occupancy N_n is given by

$$N_n \equiv \frac{g_s}{(2\pi)^2} \int dk_x dk_y f(E_{nk_xk_y}). \tag{2.14}$$

The chemical potential is determined by the relation

$$N_s = \int dz\, n(z) = \sum_n N_n. \tag{2.15}$$

At zero temperature, N_n becomes

$$\begin{aligned} N_n &= g_s \int \frac{kdk}{2\pi}\, \Theta\left(\varepsilon_F - \varepsilon_n + \frac{\hbar^2 k^2}{2m^*}\right) \\ &= \frac{g_s m^*}{2\pi\hbar^2}(\varepsilon_F - \varepsilon_n)\Theta(\varepsilon_F - \varepsilon_n), \end{aligned} \tag{2.16}$$

where Θ is the step function and ε_F is the Fermi energy.

The self-consistent procedure to solve the single-electron Kohn-Sham equation, Eq. (2.4), proceeds as follows. First, we guess the initial density profile $n(z)$, typically taken from a previous solution for the same quantum well and for a similar density, if such a solution is available. Then, Eqs. (2.7) and (2.8) or (2.9) are used to calculate the Hartree and exchange-correlation potentials, respectively, for the given density $n(z)$. The Schrödinger equation, Eq. (2.4), is then solved numerically, to obtain the subband energies and wave functions. The numerical method that we use is based on the Runge-Kutta method for integration of ordinary differential equations [47]. Once ε_n and $\varphi_n(z)$ are found, a new

density is computed through Eq. (2.13). The new and old densities are compared through

$$\eta \equiv \frac{\int dz\, |n_{new}(z) - n_{old}(z)|}{\int dz\, n_{old}(z)}. \tag{2.17}$$

If the convergence factor η is larger than a given tolerance (typically 10^{-4}–10^{-6}), we redefine the new density as a weighted sum of n_{new} and n_{old}, and repeat the calculation described. This procedure is iterated until convergence is achieved.

In Section 2.3 we will introduce the modifications necessary to include in-plane magnetic fields, and in Chapter 8, we will generalize the formalism to allow for the possibility of spin-polarized ground states of the electron gas. In Appendix B the applicability of the local-density approximation to our quantum well problem is analyzed.

2.2 Intersubband optical absorption without magnetic field

In this section we present the theory of optical absorption due to intersubband excitations with no magnetic field applied in the semiconductor structure. Ours is a linear response calculation, and was first introduced by Ando [40], who applied it to accumulation and inversion layers on Si. The approximation scheme employed is based on the local-density approximation to the density functional theory, and was introduced to account for the exchange-correlation or exciton-like effects in intersubband optical absorption. The TDLDA represents an alternative to more involved many-body techniques such as directly solving the so-called Bethe-Salpeter equation [48], and has been employed in a number of studies of intersubband collective modes and optical absorption [49, 29, 50, 27, 51].

The early experimental results of intersubband optical absorption in quasi-2D electron systems where interpreted implicitly assuming that the resonance takes

place when the energy of the incident infrared light equals the corresponding subband separations [52]. Soon, it was realized that this is not the case. If the dynamic Hartree screening of the resonance is included in the response calculation, the intersubband resonances are shifted by a positive amount—the so-called depolarization shift [22, 23, 24]. The depolarization-shift-corrected energies actually give a poorer agreement with experiment than the self-consistent subband separations. The agreement is substantially improved when the exciton-like or vertex-correction effect is taken into account [40]. Strictly speaking, the absorption peaks correspond to the collective modes of the system, which are given by the poles of the appropriate response function [53]. The calculation of this response function within the TDLDA is the subject matter of this section.

Since the wavelength of infrared light (whose frequency is of the order of the subband separations) is much larger than the width of typical semiconductor quantum wells, our theory assumes the dipole approximation. We also neglect retardation effects [24]. Let the z-axis label the growth or confinement direction in the quantum well. Since we are interested in intersubband transitions, we study the response to a radiation field $\boldsymbol{d}(\omega) = De^{-i\omega t}\boldsymbol{z}$ applied in the z-direction. The total electric field E, the current density j, and the polarization P are also given expressions of the form:

$$\begin{aligned} E(z,\omega,t) &= E(z,\omega)e^{-i\omega t}, \\ j(z,\omega,t) &= j(z,\omega)e^{-i\omega t}, \\ P(z,\omega,t) &= P(z,\omega)e^{-i\omega t}, \end{aligned} \tag{2.18}$$

and are related by the equations

$$-i\omega P(z,\omega) = j(z,\omega), \tag{2.19}$$

$$E(z,\omega) = D - \frac{4\pi}{\epsilon} P(z,\omega). \tag{2.20}$$

The power absorbed by the electron gas per unit area is

$$\mathcal{P}(\omega) = \frac{1}{2} \int dz \; Re\left[\, j(z,\omega) E^*(z,\omega)\right]. \tag{2.21}$$

Noting that

$$\begin{aligned} j(z,\omega)E^*(z,\omega) &= j(z,\omega)\left[D^* - \frac{4\pi}{\epsilon} P^*(z,\omega)\right] \\ &= j(z,\omega)\left[D^* + \frac{4\pi i}{\epsilon\omega} j^*(z,\omega)\right] \\ &= j(z,\omega)D^* + \frac{4\pi i}{\epsilon\omega}|j(z,\omega)|^2, \end{aligned} \tag{2.22}$$

we obtain

$$\mathcal{P}(\omega) = \frac{1}{2} \int dz \; Re\left[\, j(z,\omega) D^*\right]. \tag{2.23}$$

The zz-component of the irreducible and reducible conductivity tensors σ_{zz} and $\tilde{\sigma}_{zz}$, which give the response of the system to the total and external probe, respectively, are defined as

$$j(z,\omega) \equiv \sigma_{zz}(z,\omega) E(z,\omega) \equiv \tilde{\sigma}_{zz}(z,\omega) D. \tag{2.24}$$

Using this definition and Eq. (2.23) we obtain

$$\begin{aligned} \mathcal{P}(\omega) &= \frac{1}{2} \int dz \; Re\left[\, \tilde{\sigma}_{zz}(z,\omega)|D|^2\right], \\ &= \frac{1}{2}|D|^2 Re\left[\, \tilde{\sigma}^{2D}_{zz}(\omega)\right], \end{aligned} \tag{2.25}$$

where we have introduced the modified two-dimensional conductivity

$$\tilde{\sigma}^{2D}_{zz} \equiv \int dz \tilde{\sigma}_{zz}(z,\omega) = \frac{1}{D} \int dz j(z,\omega). \tag{2.26}$$

The external electric field induces a time-dependent change in the electronic density, denoted by $\Delta n(z,\omega)e^{-i\omega t}$. In turn, the density fluctuations create an effective perturbing potential

$$\mathcal{H}'e^{-i\omega t} = \left[eDz + \Delta V_H(z) + \Delta V_{XC}\right] e^{-i\omega t}, \tag{2.27}$$

with

$$\Delta V_H(z) = -\frac{4\pi e^2}{\epsilon}\int_{-\infty}^{z} dz' \int_{-\infty}^{z'} dz''\Delta n(z''), \tag{2.28}$$

$$\Delta V_{XC}(z) = \frac{\partial V_{XC}}{\partial n}\Delta n(z). \tag{2.29}$$

As we will see below, $\Delta V_H(z)$ gives rise to the depolarization shift and $\Delta V_{XC}(z)$ to the exciton-like effect. Using time-dependent perturbation theory, the density variation is found to be

$$\Delta n(z,\omega) = \sum_{n\,n'} g_{nn'}\varphi_n(z)\varphi_{n'}(z)\frac{-2\hbar\omega_{n'n}}{(\hbar^2\omega_{n'n}^2 - \hbar^2\omega^2)}\langle n'|\mathcal{H}'|n\rangle, \tag{2.30}$$

where

$$g_{nn'} = g_s\sum_{\boldsymbol{k}} f_n(\boldsymbol{k})\left[1 - f_{n'}(\boldsymbol{k})\right], \tag{2.31}$$

takes care of the occupation of the initial and final states in the intersubband transition. The spin degeneracy is denoted by g_s, $f_n(\boldsymbol{k})$ is the Fermi factor defined in Eq. (2.12), $\varphi_n(z)$ is the self-consistent wave function with eigenenergy ε_n (cf. Eq. (2.4)), $\omega_{n'n} \equiv \varepsilon_{n'} - \varepsilon_n$, and the summation is over $n \neq n'$. Note that Eq. (2.30) is valid for any number of subbands occupied, and it allows transitions to an arbitrary number of higher subbands. In particular, if only the lowest subband (denoted by 1) is occupied in the ground state, we have $g_{nn'} = N_s\delta_{n1}$, where N_s is the electron concentration per unit area. The induced current density is obtained using the equation of continuity:

$$j(z,\omega) = -\int_{-\infty}^{z} dz'(-e)(-i\omega)\Delta n(z',\omega)$$

$$= 2i\omega e \sum_{n\,n'} \int_{-\infty}^{z} dz' g_{nn'} \varphi_n(z') \varphi_{n'}(z') \frac{\hbar\omega_{n'n}}{(\hbar^2\omega_{n'n}^2 - \hbar^2\omega^2)} \langle n'|\mathcal{H}'|n\rangle, \tag{2.32}$$

and, therefore

$$\tilde{\sigma}_{zz}^{2D}(\omega) = \frac{1}{D}\int_{-\infty}^{\infty} dz j(z,\omega)$$

$$= \frac{2i\omega e}{D} \sum_{n\,n'} \int_{-\infty}^{\infty} dz \int_{-\infty}^{z} dz' g_{nn'} \varphi_n(z') \varphi_{n'}(z') \frac{\hbar\omega_{n'n}}{(\hbar^2\omega_{n'n}^2 - \hbar^2\omega^2)} \langle n'|\mathcal{H}'|n\rangle$$

$$= -\frac{2i\omega e}{D} \sum_{n\,n'} z_{nn'} g_{nn'} \frac{\hbar\omega_{n'n}}{(\hbar^2\omega_{n'n}^2 - \hbar^2\omega^2)} \langle n'|\mathcal{H}'|n\rangle, \tag{2.33}$$

where $z_{nn'} = \int_{-\infty}^{\infty} dz \varphi_n(z) z \varphi_{n'}(z)$. Taking a matrix element of Eq. (2.27) we obtain

$$eDz_{nn'} = \langle n'|\mathcal{H}'|n\rangle - \langle n'|\Delta V_H|n\rangle - \langle n'|\Delta V_{XC}|n\rangle$$

$$= \langle n'|\mathcal{H}'|n\rangle + \sum_{m\,m'} g_{mm'}(\alpha_{nn',mm'} - \beta_{nn',mm'}) \frac{\hbar\omega_{n'n}}{(\hbar^2\omega_{n'n}^2 - \hbar^2\omega^2)} \langle m'|\mathcal{H}'|m\rangle, \tag{2.34}$$

where

$$\alpha_{nn',mm'} = -2\frac{4\pi e^2}{\epsilon} \int_{-\infty}^{\infty} dz \varphi_{n'}(z)\varphi_n(z) \int_{-\infty}^{z} dz' \int_{-\infty}^{z'} dz'' \varphi_{m'}(z'')\varphi_m(z'') \tag{2.35}$$

$$\beta_{nn',mm'} = -2\int_{-\infty}^{\infty} dz \varphi_{n'}(z)\varphi_n(z) \frac{\partial V_{XC}}{\partial n}(z) \varphi_{m'}(z)\varphi_m(z). \tag{2.36}$$

With the definitions

$$\begin{aligned} A_{nn',mm'} &\equiv \delta_{nm}\delta_{n'm'}(\hbar\omega_{m'm})^2 \\ &+ g_{mm'}^{1/2} g_{nn'}^{1/2} (\alpha_{nn',mm'} - \beta_{nn',mm'})(\hbar\omega_{m'm}\hbar\omega_{n'n})^{1/2}, \end{aligned} \tag{2.37}$$

$$u_{mm'} \equiv \frac{(\hbar\omega_{m'm})^{1/2} g_{mm'}^{1/2} \langle m'|\mathcal{H}'|m\rangle}{(\hbar^2\omega_{m'm}^2 - \hbar^2\omega^2)}, \tag{2.38}$$

Eq. (2.34) becomes

$$eD(\hbar\omega_{n'n})^{1/2} g_{nn'}^{1/2} z_{n'n} = \sum_{mm'} \left[A_{nn',mm'} - (\hbar\omega)^2 \delta_{nm}\delta_{n'm'}\right] u_{mm'} \tag{2.39}$$

Using Eq. (2.38) and Eq. (2.39) we rewrite the last line of Eq. (2.33) as

$$\begin{aligned}\tilde{\sigma}_{zz}^{2D}(\omega) &= -\frac{2i\omega e}{D}\sum_{n\,n'}\frac{1}{eD}\left[eD(\hbar\omega_{n'n})^{1/2}g_{nn'}^{1/2}z_{n'n}\right]u_{nn'} \\ &= -\frac{2i\omega}{D^2}\sum_{n\,n'}\sum_{m\,m'}u_{nn'}\left[A_{nn',mm'}-(\hbar\omega)^2\delta_{nm}\delta_{n'm'}\right]u_{mm'} \qquad (2.40)\end{aligned}$$

Defining the transformation matrix U such that $\tilde{A}=U^{-1}AU$ is diagonal, we get

$$u_{nn'}=eD\sum_{\eta\,n\,n'}\frac{U_{nn',\eta}U^{-1}_{\eta,mm'}z_{mm'}(\hbar\omega_{m'm})^{1/2}}{\tilde{A}_{\eta\eta}-\omega^2} \qquad (2.41)$$

and,

$$\tilde{\sigma}_{zz}^{2D}(\omega)=-2i\omega e^2\sum_{\eta nn'mm'}\frac{z_{nn'}U_{nn',\eta}U_{mm',\eta}z_{mm'}(\hbar\omega_{n'n})^{1/2}(\hbar\omega_{m'm})^{1/2}}{\tilde{A}_{\eta\eta}-\omega^2} \qquad (2.42)$$

(The subindex η has a one-to-one correspondence to the double index (n,n').) Finally, one gets

$$\tilde{\sigma}_{zz}^{2D}(\omega)=-\frac{i\omega e^2N_s}{m^*}\sum_{\eta}\frac{\tilde{f}_\eta}{\tilde{\omega}_\eta^2-\omega^2-2i\omega/\tau}, \qquad (2.43)$$

where

$$\tilde{f}_\eta=\left[\left(\frac{2m^*}{N_s\hbar^2}\right)^{1/2}\sum_{nn'}(\hbar\omega_{n'n}g_{n'n})^{1/2}\,z_{n'n}U_{nn',\eta}\right]^2, \qquad (2.44)$$

and $\hbar\tilde{\omega}_\eta=(\tilde{A}_{\eta\eta})^{1/2}$. In Eq. (2.43) we have introduced a phenomenological relaxation time τ. The resonances or intersubband collective modes of the system occur at $\omega=\tilde{\omega}_\eta$, and their strength is determined by the oscillator strength $\tilde{f}_\eta$. Let us consider the particular case where only one subband is populated, the frequency ω is close to $\tilde{\omega}_{n1}$, and we can neglect coupling to transitions to subbands other than the n^{th} subband. In this case one gets

$$\tilde{\sigma}_{zz}^{2D}=-\frac{i\omega e^2N_s\tilde{f}_{n1}}{m^*}\left[\tilde{\omega}_{n1}^2-\omega^2-2i\omega/\tau\right]^{-1}, \qquad (2.45)$$

where

$$\tilde{f}_{n1}=\frac{2m^*}{\hbar^2N_s}\hbar\omega_{n1}z_{n1}^2, \qquad (2.46)$$

and the resonance energy is given by

$$\hbar\tilde{\omega}_{n1} = \left[\hbar^2\omega_{n1}^2 + N_S\hbar\omega_{n1}\left(\alpha_{n1,n1} - \beta_{n1,n1}\right)\right]^{1/2}. \tag{2.47}$$

Since $\alpha_{nn',mm'} > 0$ and $\beta_{nn',mm'} > 0$, we see that the depolarization shift (the $\alpha_{nn',mm'}$ term originated in the ΔV_H of Eq. (2.27)) tends to increase the resonance energy, and the exciton-like shift (the $\beta_{nn',mm'}$ term originated in the ΔV_{XC} of Eq. (2.27)) has the opposite effect.

The density fluctuations (Eq. (2.30)) associated with the collective modes of the system give a very useful physical picture of the excitations which we will take advantage of repeatedly in the next two chapters. For the fluctuations associated with the resonant energy $\tilde{\omega}_\eta$ one gets

$$\Delta n_\eta(z) \propto \sum_{n\,n'} \omega_{n'n}^{1/2} g_{nn'}^{1/2} \varphi_n(z)\varphi_{n'}(z) U_{nn',\eta}. \tag{2.48}$$

2.3 Self-consistent electronic structure with in-plane magnetic field

In this section we extend the electronic structure calculation (the calculation of self-consistent single-particle energies and wavefunctions, and ground-state electron density) that we started in Section (2.1), to the case of a semiconductor quasi-2D structure with a magnetic field applied in the plane of the electron gas, that is, in the so-called Voigt geometry. Ando calculated electronic structure in the Voigt geometry in accumulation layers within the Hartree approximation [54], and later extended the treatment to include exchange-correlation effects [55]. More recently, Stopa and Das Sarma [44] studied the electronic structure of parabolic quantum wells in the in-plane magnetic field geometry within the local-density approximation.

Again we consider an electron gas confined in the z-direction, and work in the effective mass approximation, assuming a constant effective mass. The treatment

is analogous to the case of no magnetic field applied, with the difference that an in-plane magnetic field couples the z-motion with the in-plane momenta, say k_x, causing the quantum subbands to acquire a dispersion in k_x. If a magnetic field $\boldsymbol{B} = (0, B, 0)$ is applied, and working in the Landau gauge $\boldsymbol{A} = (Bz, 0, 0)$, the single-particle Kohn-Sham equation reads, ignoring the Zeeman splitting,

$$\left[\frac{(-i\hbar\boldsymbol{\nabla} + \frac{e}{c}\boldsymbol{A})^2}{2m^*} + V_{EFF}(z)\right]\Psi_{nk_xk_y}(\boldsymbol{x}) = E_{nk_xk_y}\Psi_{nk_xk_y}(\boldsymbol{x}). \tag{2.49}$$

The effective potential $V_{EFF}(z)$ has the same form as in the absence of a magnetic field,

$$V_{EFF}(z) = V_{CONF}(z) + V_H(z) + V_{XC}(z) \tag{2.50}$$

and $V_H(z)$ (see Eq. (2.7)) and $V_{XC}(z)$ (see Eq. (2.8)) depend on the magnetic field only through the electron density $n(z)$. We point out that the expression for the exchange-correlation potential used does not take into account the presence of a magnetic field, and therefore its use is not fully justified in this case. The most appropriate treatment of this problem within LDA would be a spin-polarized calculation, like the one applied in Chapter 8 to the $B = 0$ case, but we have not attempted such approach in this dissertation. However, we expect the unpolarized exchange-correlation potential not to give rise to serious errors, since the magnetic fields considered here are only moderately high ($< 6T$).

Factorizing the total eigenfunction as

$$\Psi_{nk_xk_y}(\boldsymbol{x}) = \frac{1}{\sqrt{L_xL_y}}e^{i(k_xx+k_yy)}\varphi_{nk_x}(z), \tag{2.51}$$

(L_x and L_y are the sample dimensions) Eq. (2.49) simplifies to the following ordinary differential Kohn-Sham equation for the z-dependence

$$\left[-\frac{\hbar^2}{2m^*}\frac{d^2}{dz^2} + \frac{(\hbar k_x + m^*\omega_c z)^2}{2m^*} + V_{EFF}(z)\right]\varphi_{nk_x}(z) = \varepsilon_{nk_x}\varphi_{nk_x}(z), \tag{2.52}$$

where $\varepsilon_{nk_x} = E_{nk_xk_y} - \frac{\hbar^2 k_y^2}{2m^*}$, and $\omega_c = \frac{eB}{m^*c}$ is the cyclotron frequency. Following the notation introduced in Section 2.1, we write the electronic density as

$$\begin{aligned} n(z) &= g_s \sum_{n,\boldsymbol{k}} f(E_{nk_xk_y}) |\Psi_{nk_xk_y}(\boldsymbol{x})|^2 \\ &= \sum_{nk_x} N_{nk_x} |\varphi_{nk_x}(z)|^2 = \frac{L_x}{2\pi} \sum_n \int N_{nk_x} |\varphi_{nk_x}(z)|^2, \end{aligned} \tag{2.53}$$

where the subband occupancies are given by

$$N_{nk_x} \equiv \frac{g_s}{2\pi L_x} \int dk_y f(E_{nk_xk_y}) \tag{2.54}$$

The chemical potential is fixed again by the requirement that the total number of electrons equals the areal density N_s, and is obtained by solving numerically the equation

$$N_s = \sum_{nk_x} N_{nk_x} = \frac{L_x}{2\pi} \sum_n \int dk_x N_{nk_x}. \tag{2.55}$$

At zero temperature, N_{nk_x} reduces to

$$N_{nk_x} = \frac{g_s}{2\pi L_x} \left(\frac{2m^*}{\hbar^2} \right)^{1/2} \sqrt{\varepsilon_F - \varepsilon_{nk_x}}\, \Theta(\varepsilon_F - \varepsilon_{nk_x}). \tag{2.56}$$

The iterative scheme to solve for the self-consistent electronic states and energies is analogous to the zero-magnetic-field one described in Section 2.1. The main difference is that the Kohn-Sham equation (Eq. (2.52)) now depends on the quasi-continuous (after periodic boundary conditions are assumed) quantum number k_x. In practice, we discretize this variable into a grid and solve Eq. (2.52) for each value of k_x on the grid. This finite set of solutions $(\varepsilon_{nk_x}, \varphi_{nk_x})$ of the Kohn-Sham equation are then used in the calculation of the subband occupancies, the density and the chemical potential. Typically, 40 to 80 points in half of the k_x–grid (for asymmetric wells, like the asymmetric parabolic wells of Chapter 3, one needs twice as many points to cover separately negative and positive k_x

values) are enough to obtain the degree of convergence necessary in the response calculations presented in the next section.

2.4 Intersubband optical absorption with in-plane magnetic fields

Now we proceed to generalize the theory of intersubband optical absorption to the Voigt geometry problem, where a dc magnetic field is applied in the plane of the confined electron gas, and the incident radiation propagates in the growth direction, with polarization perpendicular to the magnetic field. The formalism is analogous to the one employed in the case of intersubband optical absorption without magnetic field (Section 2.2), and was also introduced by Ando to study silicon-based quasi-two dimensional electron systems [55]. We keep the simplifying assumptions stated in the previous section, and assume as well that there is an external magnetic field $\boldsymbol{B} = (0, B, 0)$. In this geometry intersubband transition are possible even if the polarization of the incident radiation is in the plane of the electron slab, because the Lorentz force couples the motion of the carriers in the x- and z-direction. If a radiation field of long wavelength is applied with normal incidence, $\boldsymbol{D}(\omega, t) = De^{-i\omega t}\boldsymbol{x}$, the total electric field $\boldsymbol{E}$, the current density $\boldsymbol{j}$, and the polarization $\boldsymbol{P}$ are also given by expressions of the form:

$$\begin{aligned}
\boldsymbol{E}(z, \omega, t) &= \boldsymbol{E}(z, \omega)e^{-i\omega t}, \\
\boldsymbol{j}(z, \omega, t) &= \boldsymbol{j}(z, \omega)e^{-i\omega t}, \\
\boldsymbol{P}(z, \omega, t) &= \boldsymbol{P}(z, \omega)e^{-i\omega t}.
\end{aligned} \tag{2.57}$$

The absorbed power per unit area by the electron gas is

$$\mathcal{P}(\omega) = \frac{1}{2}\int dz Re\left[\boldsymbol{j}(z, \omega) \cdot \boldsymbol{E}^*(z, \omega)\right]. \tag{2.58}$$

Taking into account that

$$\begin{aligned}\boldsymbol{j}\cdot\boldsymbol{E}^* &= \boldsymbol{j}\cdot\left[\boldsymbol{D}^* - \frac{4\pi}{\epsilon}\boldsymbol{P}^*\right] \\ &= \boldsymbol{j}\cdot\left[\boldsymbol{D}^* + \frac{4\pi i}{\epsilon\,\omega}\boldsymbol{j}^*\right] \\ &= j_x(z,\omega)D^* + \frac{4\pi i}{\epsilon\,\omega}|\boldsymbol{j}(z,\omega)|^2, \end{aligned} \tag{2.59}$$

we can rewrite the absorbed power as

$$\mathcal{P}(\omega) = \frac{1}{2}\int dz Re\left[j_x(z,\omega)D^*\right]. \tag{2.60}$$

Therefore,

$$\mathcal{P}(\omega) = \frac{1}{2}\int dz Re\left[\tilde{\sigma}^{2D}_{xx}(\omega)\right] \tag{2.61}$$

where the xx-component of the conductivity tensor is related to the zz-component at non-zero frequency through the expression [56]

$$Re\left[\tilde{\sigma}^{2D}_{xx}(\omega)\right] = \frac{\omega_c^2}{\omega^2} Re\left[\tilde{\sigma}^{2D}_{zz}(\omega)\right]. \tag{2.62}$$

In what follows we will calculate the zz-component $\tilde{\sigma}^{2D}_{zz}(\omega)$, similarly to what was done in Section 2.2. The external electric field induces a time-dependent change in the electronic density, denoted by $\Delta n(z,\omega)e^{-i\omega t}$, and these density fluctuations generate an effective perturbing potential which ought to be found self-consistently:

$$\mathcal{H}' e^{-i\omega t} = \left[eDZ + \Delta V_H(z) + \Delta V_{XC}\right] e^{-i\omega t}, \tag{2.63}$$

with

$$\Delta V_H(z) = -\frac{4\pi e^2}{\epsilon}\int_{-\infty}^{z} dz' \int_{-\infty}^{z'} dz'' \Delta n(z''), \tag{2.64}$$

$$\Delta V_{XC}(z) = \frac{\partial V_{XC}}{\partial n}\Delta n(z). \tag{2.65}$$

Applying time-dependent perturbation theory to first order in the perturbing Hamiltonian $\mathcal{H}'$, we obtain for the density fluctuation field:

$$\begin{aligned}\Delta n(z,\omega) &= \frac{g_s}{L_x L_y}\sum_{n n' k_x}\varphi_{n k_x}(z)\varphi_{n' k_x}(z)\frac{(-2\hbar\omega_{n'n}(k_x))}{(\hbar^2\omega_{n'n}(k_x)^2-\hbar^2\omega^2)} \\ &\times f(E_n(\boldsymbol{k}))\left[1-f(E_{n'}(\boldsymbol{k}))\right]\langle n' k_x|\mathcal{H}'|n k_x\rangle, \end{aligned} \tag{2.66}$$

where we have introduced the energy differences

$$\hbar\omega_{n'n}(k_x) = E_{n'}(\boldsymbol{k}) - E_n(\boldsymbol{k}) = \varepsilon_{n'}k_x - \varepsilon_n k_x, \tag{2.67}$$

and $E_n(\boldsymbol{k})$ are the self-consistent single-particle energies (see Eq. (2.49)). The notation for other quantities in Eq. (2.66) has been introduced in the section on electronic structure in the Voigt geometry, Section 2.3. The continuity equation gives the current density

$$j_z(z,\omega) = -\int_{-\infty}^{z} dz'(-e)(-i\omega)\Delta n(z',\omega), \tag{2.68}$$

from which we obtain the modified two-dimensional conductivity

$$\tilde{\sigma}_{zz}^{2D}(\omega) \equiv \frac{1}{D}\int_{-\infty}^{\infty} dz j_z(z,\omega). \tag{2.69}$$

For the values of the magnetic field studied in this Thesis (B $\sim 5T$), only one subband is occupied at the usual areal electron densities in GaAs quantum wells ($N_s \sim 10^{11}\mathrm{cm}^{-1}$), therefore we shall assume that only the lowest subband (denoted by 1) is occupied. Let $\omega_n(k_x) \equiv E_n(\boldsymbol{k}) - E_1(\boldsymbol{k})$. Substituting $j_z(z,\omega)$ in the definition of $\tilde{\sigma}_{zz}^{2D}(\omega)$ we get

$$\tilde{\sigma}_{zz}^{2D}(\omega) = -\frac{2i\omega e}{D}\sum_{n k_x} z_n(k_x) g_n(k_x)\frac{\hbar\omega_n(k_x)}{(\hbar^2\omega_n(k_x)^2-\hbar^2\omega^2)}\langle n k_x|\mathcal{H}'|1 k_x\rangle, \tag{2.70}$$

where

$$z_n(k_x)\int_{-\infty}^{\infty} dz\varphi_{n k_x}(z)\varphi_{1 k_x}(z), \tag{2.71}$$

$$g(k_x) = \frac{g_s \Delta k_x}{(2\pi)^2} \int dk_y f(E_1(\boldsymbol{k})), \tag{2.72}$$

and Δk_x is the step in the numerical integration over the k_x variable. Next we take a matrix element of Eq. (2.63) between the states $|nk_x\rangle$ and $|1k_x\rangle$:

$$\begin{aligned} eD\langle nk_x|z|1k_x\rangle = & \\ & \sum_{mk'_x} \{\delta_{nm}\delta_{k_x k'_x}\omega_n(k_x)^2 - \delta_{nm}\delta_{k_x k'_x}\omega^2 \\ & + g(k'_x)\omega_m(k'_x)\omega_n(k_x)^{3/2}\left[\alpha_{nm}(k_x,k'_x) - \beta_{nm}(k_x,k'_x)\right]\} \\ & \times \frac{\langle nk_x|\mathcal{H}'|1k_x\rangle}{(\hbar^2\omega_n(k_x)^2 - \hbar^2\omega^2)}, \end{aligned} \tag{2.73}$$

where

$$\alpha_{nm}(k_x,k'_x) = -\frac{8\pi e^2}{\epsilon}\frac{S_{nm}(k_x,k'_x)}{[\omega_n(k_x)\omega_m(k'_x)]^{1/2}}, \tag{2.74}$$

$$\beta_{nm}(k_x,k'_x) = -2\frac{X_{nm}(k_x,k'_x)}{[\omega_n(k_x)\omega_m(k'_x)]^{1/2}}, \tag{2.75}$$

and

$$S_{nm}(k_x,k'_x) = \int_{-\infty}^{\infty} dz \varphi_{nk_x}(z)\varphi_{1k_x}\int_{-\infty}^{z} dz'(z-z')\varphi_{1k'_x}(z')\varphi_{mk'_x}(z'), \tag{2.76}$$

$$X_{nm}(k_x,k'_x) = \int_{-\infty}^{\infty} dz \varphi_{nk_x}(z)\varphi_{1k_x}\frac{\partial V_{xc}}{\partial n}(z)\varphi_{1k'_x}(z)\varphi_{mk'_x}(z). \tag{2.77}$$

Introducing the following quantities

$$\begin{aligned} A_{nm}(k_x,k'_x) = & \delta_{nm}\delta_{k_x k'_x}\omega_n(k_x)^2 \\ & + g(k_x)^{1/2}\omega_n(k_x)[\alpha_{nm}(k_x,k'_x) - \beta_{nm}(k_x,k'_x)]\omega_m(k'_x)g(k'_x)^{1/2}, \end{aligned} \tag{2.78}$$

$$u_m(k_x) = \frac{g(k_x)^{1/2}\omega_m(k_x)^{1/2}\langle mk_x|\mathcal{H}'|1k_x\rangle}{\omega_m(k_x)^2 - \omega^2}, \tag{2.79}$$

Eq. (2.73) becomes

$$eDg(k_x)^{1/2}\omega_n(k_x)^{1/2}z_n(k_x) = \sum_{mk'_x}[A_{nm}(k_x,k'_x) - \delta_{nm}\delta_{k_x k'_x}\omega^2]u_m(k'_x). \tag{2.80}$$

Introducing U such that $\tilde{A} = U^{-1}AU$ is diagonal we can eliminate the unknown matrix element $\langle mk'_x|\mathcal{H}'|1k_x\rangle$. Eq. (2.79) becomes

$$u_\alpha = eD \sum_{\beta\,\gamma} \frac{U_{\alpha\beta} U^{-1}_{\beta\gamma} g_\gamma^{1/2} \omega_\gamma^{1/2} z_\gamma}{\tilde{A}_{\beta\beta} - \omega^2} \tag{2.81}$$

where the new index α is equivalent to the double index (n, k_x), and, after some additional manipulations we finally obtain

$$\tilde{\sigma}^{2D}_{zz}(\omega) = -\frac{2i\omega e}{D} \sum_\alpha \frac{\tilde{f}_\alpha}{\tilde{\omega}^2_\alpha - \omega^2 - 2i\omega/\tau}, \tag{2.82}$$

where

$$\tilde{f}_\alpha = \frac{2m^*}{N_s\hbar^2} \left(\sum_\alpha (\hbar\omega_\alpha)^{1/2} g_\alpha^{1/2} z_\alpha \right)^2, \tag{2.83}$$

and the resonant energies are given by $\hbar\tilde{\omega}_\alpha = (\tilde{A}_{\alpha\alpha})^{1/2}$. Notice that the expression for $\tilde{\sigma}^{2D}_{zz}(\omega)$ is formally analogous to the expression obtained without magnetic field in Section 2.2, provided the subindices are appropriately reinterpreted. In Eq. (2.82) we have introduced a constant phenomenological relaxation time τ, although this is not strictly valid in the presence of a magnetic field, and may have some influence in the lineshape of the resonances [55]. Before concluding this section we write down the expression for the density fluctuations associated with the resonant modes of the system, which will be employed in the study of quasi-parabolic wells:

$$\Delta n_\alpha(z) \propto \sum_{n,k_x} \omega_n(k_x) g(k_x)^{1/2} \varphi_{nk_x}(z) \varphi_{1k_x}(z) U_{nk_x,\alpha} \tag{2.84}$$

CHAPTER 3

Perfect and asymmetric parabolic quantum wells

3.1 Introduction

Remotely doped $Al_xGa_{1-x}As$ parabolic quantum wells (PQW) are systems where a wide, high mobility quasi-2D electron gas can be realized [10]. Such systems have been proposed as candidates for the observation of three dimensional electron-electron interaction effects in an environment free of impurities [4]. The generalized Kohn's theorem [8], which states that an electron gas in a perfect parabolic confinement with a magnetic field applied in an arbitrary direction absorbs long-wavelength light at the two frequencies that correspond to excitations in the center of mass (CM) motion, fully explained the results of far-infrared optical absorption experiments in perfect PQWs. It then became clear that this type of experiments could reveal characteristics of the electron-electron interaction only if slight imperfections were introduced in the parabolic confinement. Thereafter, a number of imperfect parabolic well systems have been investigated experimentally [57, 16, 11], and theoretically without magnetic fields [50], and with tilted [58] and in-plane magnetic fields [56].

In this chapter we will first enunciate the generalized Kohn's theorem for PQWs [8] and present some preliminary results for perfect PQWs without any perturbations, to demonstrate the basic properties of PQWs. Once the accuracy

of our numerical procedures is established in the case of perfect PQWs, we proceed to discuss our results for asymmetric parabolic wells [14, 15]. Although we will give some results for asymmetric PQW without magnetic field, we will concentrate on the case of the Voigt geometry, i. e., with a magnetic field $\vec{B}$ applied in the plane of the electron slab and radiation propagating perpendicular to that plane with polarization $\vec{E}^{RAD} \perp \vec{B}$. Our calculations will be compared in detail with recent far-infrared (FIR) absorption experiments in asymmetric PQWs in the Voigt geometry [11].

3.2 Perfect parabolic quantum wells

Before going into the main results of this chapter—the magneto-optical absorption spectra of asymmetric PQWs—in this section we enunciate the generalized Kohn's theorem and present a representative set of results for perfect parabolic wells without perturbations. Basically, our aim is to illustrate the two main characteristics of PQWs: first, the fact that the ground-state electronic density distribution is approximately constant throughout the electron slab, with a constant value given by the curvature of the parabolic potential; and, second, the validity of the generalized Kohn's theorem, which fixes the frequencies at which long-wavelength optical-absorption takes place, both with an without an applied magnetic field. The generalized Kohn's theorem provides a stringent test on the accuracy of our numerical calculations, which, as we shall see, is passed satisfactorily.

Let the confining potential have a quadratic dependence along the z-direction

$$V_{\text{conf}}(z) = \frac{1}{2} m^* \omega_0^2 z^2, \tag{3.1}$$

where m^* is the electron effective mass and ω_0 is the design harmonic frequency.

By solving Poisson's equation for a constant charge density n_0

$$\frac{d^2V_{\rm conf}(z)}{dz^2} = \frac{4\pi e^2}{\epsilon} n_0, \tag{3.2}$$

one obtains

$$V_{\rm conf}(z) = \frac{2\pi e^2 n_0}{\epsilon} z^2, \tag{3.3}$$

and using Eqs. (3.1) and (3.3) one gets

$$n_0 = \frac{m^*\epsilon\omega_0^2}{4\pi e^2}. \tag{3.4}$$

n_0 is the density of a positive background that produces a parabolic potential given by Eq. (3.1). The basic property of the parabolic confinement potential of Eq. (3.1) is to emulate a positive background of density n_0.

The generalized Kohn's theorem states that the energies at which a parabolically confined electron gas absorbs long-wavelength radiation in the presence of an arbitrary uniform magnetic field do not depend on the electron-electron interactions, and therefore are the same as those of a *single* electron in the same potential and magnetic field. For the parabolic confinement of Eq. (3.1) and a magnetic field $\mathbf{B} = (B\sin\theta, 0, B\cos\theta)$ tilted an angle θ with respect to the z-direction, the resonant frequencies are

$$\omega_{1,2} = \left[\frac{1}{2}\left(\omega_{\rm c}^2 + \omega_0^2\right) \pm \frac{1}{2}\left(\omega_{\rm c}^4 + \omega_0^4 - 2\,\omega_0^2\,\omega_{\rm c}^2\cos 2\theta\right)^{1/2}\right]^{1/2}, \tag{3.5}$$

where $\omega_{\rm c} = \frac{eB}{m^*c}$ is the cyclotron frequency. In the Voigt geometry, that is, for an in-plane magnetic field, $\theta = 90^0$ and $\omega_{1,2} = \sqrt{\omega_{\rm c}^2 + \omega_0^2}$, 0. In the absence of any magnetic field, $\omega_{\rm c} = 0$, and $\omega_{1,2} = \omega_0$, 0. The solution $\omega_2 = 0$ has zero weight in absorption experiments.

We start the presentation of numerical results by showing in Fig. 3.1 the LDA self-consistently calculated wavefunctions, energy levels, and effective potentials

for a cutoff parabolic potential, with a design density of $n_0 = 2.24 \times 10^{16}\, cm^{-3}$, or a characteristic energy $\omega_0 = \sqrt{4\pi e^2 n_0/m^*\epsilon} = 6.1\ meV$. The calculational technique employed is described in detail in Section 2.1. The bare confining potential is not perfectly parabolic because, by design, the parabolic region eventually ends abruptly. The width of the parabolically varying potential region is 2000Å in this particular sample. The abrupt end of the parabolicity has a negligible effect on the basic issues considered in this section, as long as the electron slab does not reach the edge of the parabolic region. As we can see in Fig. 3.1, the electronic density is almost constant over the entire width of the electron slab, and the self-consistent potential is remarkably constant over the same region. This illustrates the virtually perfect screening of the parabolic potential—equivalent to a uniform positive background—carried out by the electron gas, correctly described thanks to the self-consistent nature of the calculation. In Fig. 3.2 we show how, for the same sample, the density profile varies as the areal density N_S is increased. Once the design density n_0 is reached inside the electron slab, further increase in N_S gives rise to a widening of the slab, but keeping the bulk density approximately constant and equal to n_0. The edge oscillation is very pronounced at $N_S = 4.0 \times 10^{11}\, cm^{-2}$, because the electron gas is wide enough to see the abrupt end of the parabolic region (at 1000Å). In Fig. 3.3 we compare the electron density profiles with and without an in-plane magnetic field (for another parabolic well, with design density $n_0 = 2.4 \times 10^{16}\, cm^{-3}$). Since the in-plane magnetic field localizes the electron wavefunctions to roughly within a magnetic length $\ell_c = \sqrt{\hbar c/eB}$ in the z-direction, screening is more effective that in the absence of a magnetic field. As a consequence, the electron density $n(z)$ in the middle region of the slab is more uniform and closer to n_0 in the magnetic field case.

Fig. 3.4 shows absorption spectra calculated within TDLDA (see Sections 2.2 and 2.4 for a description of the formalism), with and without magnetic field, for a parabolic well with $n_0 = 2.4 \times 10^{16}\, cm^{-3}$. The calculated spectra have only one peak, in agreement with the generalized Kohn's theorem, at ω_0 and $(\omega_0^2 + \omega_C^2)^{1/2}$, in the absence and presence of an in-plane magnetic field, respectively. We have verified that this result is independent of the areal electron density N_S, also in agreement with Kohn's theorem. The resonant mode described by Kohn's theorem corresponds to a rigid motion of the electron slab in the confinement direction. Thus, in linear response theory, the density fluctuations $\delta n(z)$ (see Eqs. (2.48) and (2.84) associated with this Kohn mode are proportional to the derivative of the equilibrium density distribution, $\frac{dn}{dz}(z)$. This relationship between $\delta n(z)$ and $\frac{dn}{dz}(z)$ is illustrated in Fig. 3.5, for the case of no applied magnetic field. The good agreement between our numerical results and the known analytical predictions, seen in Figs. 3.4 and 3.5, constitute a reassuring sign of the accuracy of our numerical procedures, before we apply them to more complex situations where no exact analytical predictions are available.

3.3 Asymmetric parabolic quantum wells

A simple departure from perfect parabolicity is given by the case of an asymmetric parabolic well consisting of two half-parabolas of slightly different curvatures. In such asymmetric PQW the generalized Kohn's theorem is no longer valid, and therefore the long-wavelength absorption spectra is expected to depend on the areal density N_S. This is indeed the case, as demonstrated by recent far-infrared (FIR) optical absorption experiments [11]. Given the simplicity of the non-parabolicity of the asymmetric PQW, the idea behind the experimental

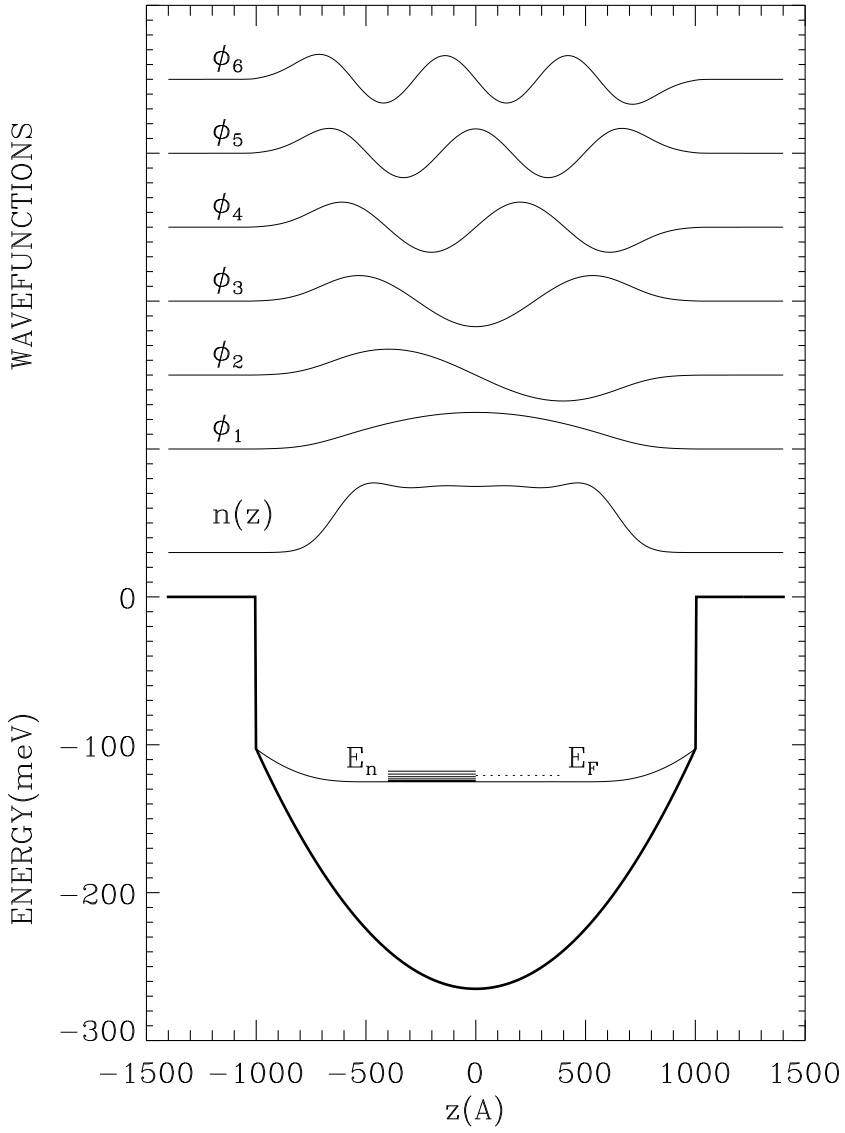

Figure 3.1: A cutoff parabolic quantum well structure, given by the bare confining potential (thick line), and its zero-magnetic-field self-consistent LDA subband energy levels E_n, eigenfunctions ϕ_n, electron density $n(z)$, Fermi energy E_F, and effective potential V_{EFF} (thin line). The parabolic region, which has a design density of $n_0 = 2.24 \times 10^{16}\, cm^{-3}$, is 2000Å wide. The areal density is $N_s = 3.0 \times 10^{11}\, cm^{-2}$; at this density, 4 subbands are populated.

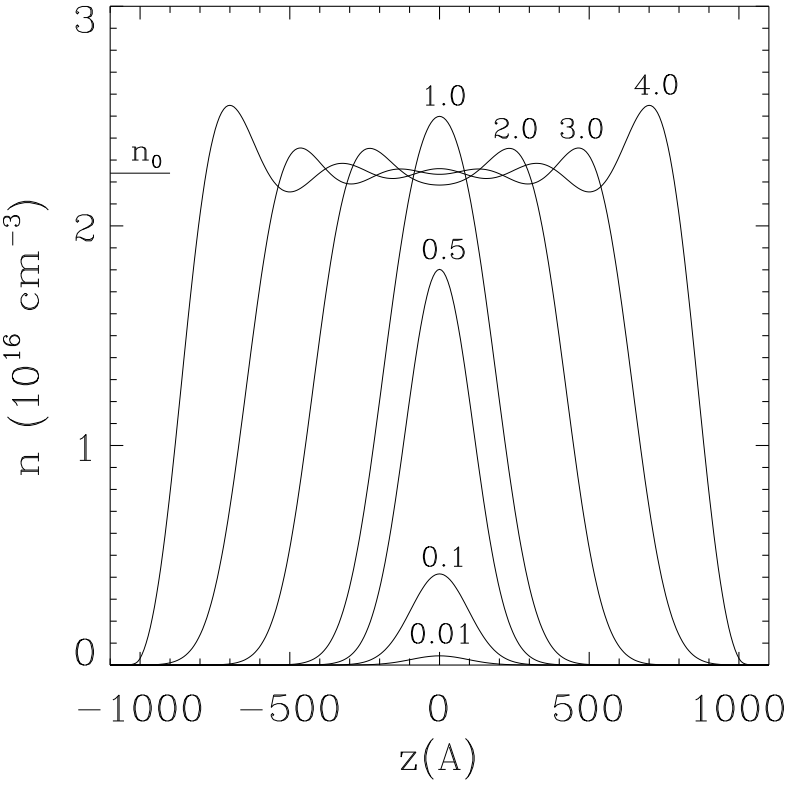

Figure 3.2: Self-consistent LDA electronic densities $n(z)$ for the parabolic well shown in Fig. 3.1, for various areal densities N_S, given in $10^{11}\,cm^{-2}$, and no magnetic field applied. The design density n_0 is marked for reference. The figure shows that as the areal density is increased, the electron slab becomes wider, but it conserves an approximately constant value in the middle region, equal to n_0.

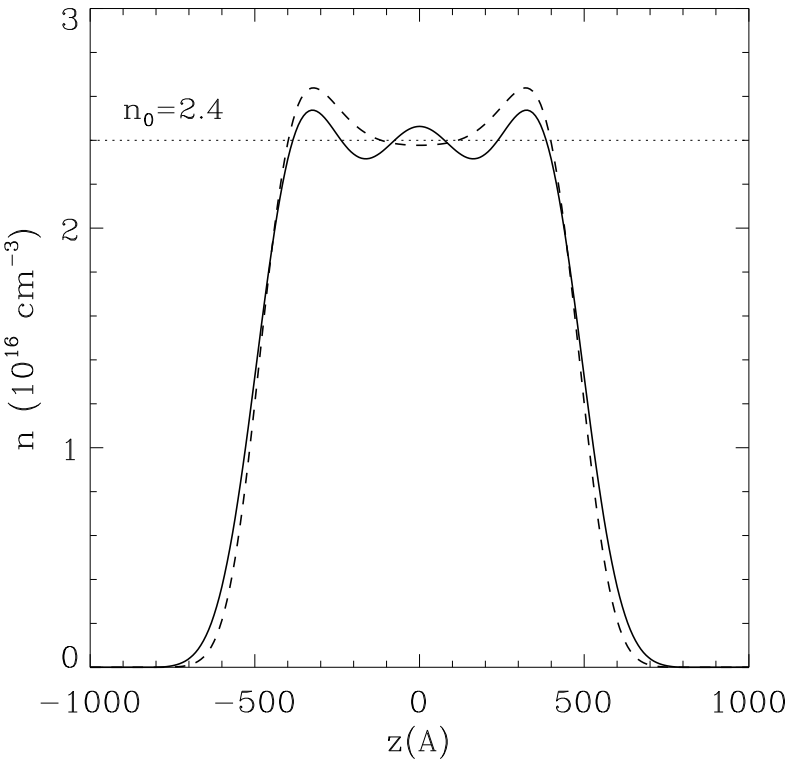

Figure 3.3: Comparison of self-consistent density profiles with and without magnetic field for a parabolic quantum well. Solid line: no magnetic field, dashed line: in-plane magnetic field $B = 4T$. The parabolic potential has a design density of $n_0 = 2.4 \times 10^{16}\, cm^{-3}$. The areal density is $N_s = 2.5 \times 10^{11}\, cm^{-2}$. The magnetic field improves the screening ability of the electron gas by reducing the extent of the electron wavefunctions in the z-direction.

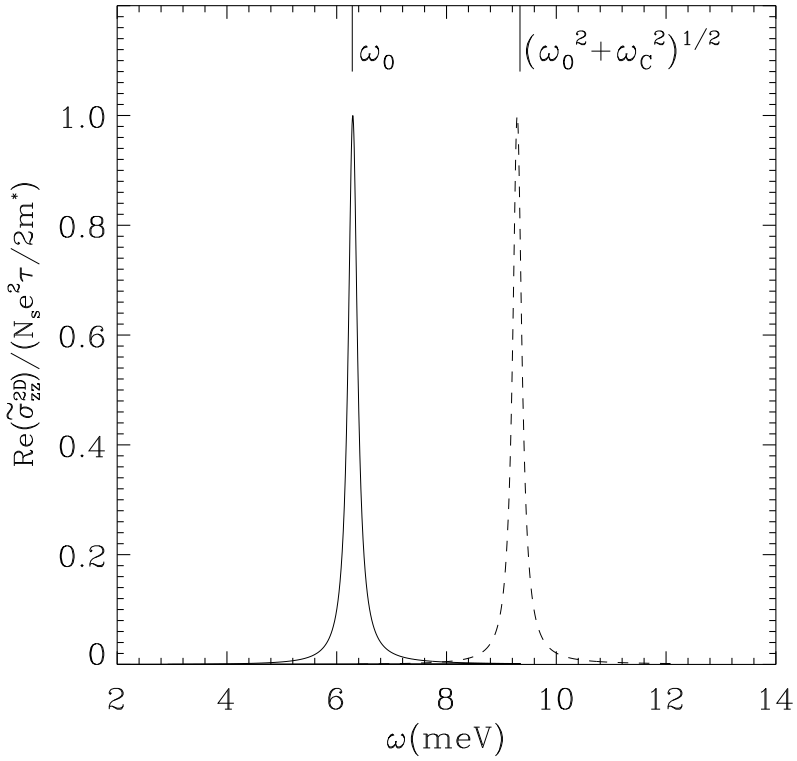

Figure 3.4: Optical absorption spectra for a parabolic quantum well, without (solid line) magnetic field, and with an in-plane magnetic field of $B = 4T$ (dashed line). The frequencies ω_0 (which gives the curvature of the well) and $(\omega_0^2 + \omega_C^2)^{1/2}$, are the resonant frequencies predicted by the generalized Kohn's theorem, without and with magnetic field, respectively. The figure shows the agreement between the calculated spectra and the analytical result, both with and without applied magnetic field.

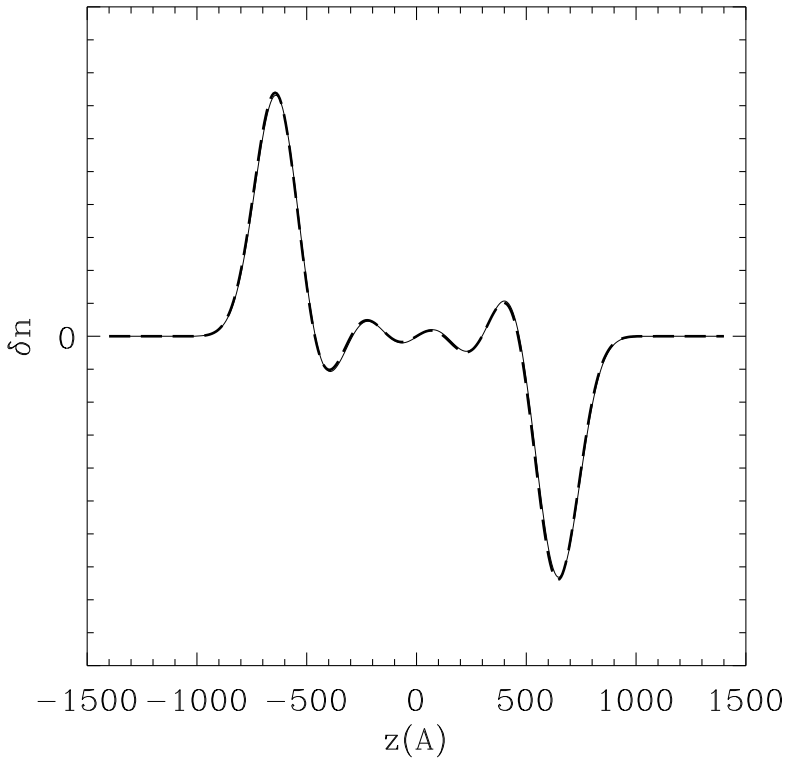

Figure 3.5: Density fluctuations $\delta n(z)$ associated with the Kohn mode for the parabolic well shown in Fig. 3.1 in the absence of magnetic field, calculated using Eq. (2.48) (thick dashed line). Also shown is the derivative of the ground-state density distribution $\frac{dn}{dz}(z)$ (thin solid line). The two curves fall on top of each other (after including an appropriate proportionality factor), demonstrating that the Kohn mode corresponds to a rigid oscillation of the electron slab as a whole in the z-direction.

study was to determine the conditions for a quasi-two-dimensional electron gas to crossover from two- to three-dimensional behavior. The FIR spectra showed such a crossover when going from the low N_S limit to the high N_S limit, where the electron slab is wide (or three-dimensional) enough to "see" the two different curvatures of the well. The spectra evolve, as the areal density increases (and with it, the width of the electron slab), from having one peak at the inter-Landau level energy difference of the bare well to having two peaks located at the Kohn frequencies of the half parabolas. The crossover region over which a unique resonance (at low N_s) splits into two "Kohn modes" (at high N_s) is roughly given by the condition $2\ell_1 < N_s/\overline{n}_0 < 4\ell_1$, where $\ell_1 = \sqrt{3}\,\ell_c$ is the radius of the second Landau orbit. The upper limit shows that to obtain two separate resonances at the Kohn frequencies the slab has to be wide enough to accommodate one excited Landau orbit in each half of the well. Here we calculate absorption spectra for an asymmetric PQW modeled following the parameter values of the sample used in Ref. [11], and compare our results with experiment in the relevant range of areal densities.

We consider the model potential shown in Fig. 3.6(a) to describe the asymmetric PQW sample studied in Ref. [11]. It consists of two half-parabolas with curvatures $\alpha_1 = 5.1 \times 10^{-5}\ meV/\text{Å}^2$ and $\alpha_2 = 6.2 \times 10^{-5}\ meV/\text{Å}^2$, and is 3000 Å wide. We choose a magnetic field in the region of the observed resonances of $B = 5.8\ T$. In Fig. 3.6(a) we show the calculated self-consistent potentials for some values of the sheet density N_s, which, as expected, become flattened over a wider region in the center of the well, as the electron slab width increases with N_s. Note, however, that the density profiles $n(z)$ shown in Fig. 3.6(b) are not flat as in the pure parabolic wells as might have been expected naively. For the

values of N_s considered in the experiment, and in our calculations with magnetic field, only the lowest subband is occupied at zero temperature. We checked that the abrupt change in the curvature at $z = 0$ does not produce unphysical results by using a similar potential with a graded change in curvature, and the density profile was identical to the original one within our numerical precision.

The calculated optical absorption spectra for the asymmetric quantum well and for several densities N_s in the range used in Ref. [11] are shown in Fig. 3.7. The frequencies associated with the half-parabolas of curvatures $\alpha_{1,2}$ are $\omega_{1,2} = 2\alpha_{1,2}/m^*$. The frequencies $w_{K1,K2}$ marked for reference on each panel of Fig. 3.7 are the "Kohn" frequencies of each half-parabola, $w_{K1,K2} = (\omega_{1,2}^2 + \omega_C^2)^{1/2}$. The phenomenological scattering time $\tau = 20 \times 10^{-12} s$, taken to be a constant in our calculations, was obtained from the linewidth of the narrower resonance in the experiment [11]. For a perfect PQW the generalized Kohn's theorem predicts a unique resonance independent of the electron density. In our case, in contrast, we obtain a strong dependence on N_s. For small $N_s \lesssim 4.7 \times 10^{10}\ cm^{-2}$ there is one strong resonance (which, for example at $N_s = 0.1 \times 10^{10}\ cm^{-2}$, has energy $\tilde{\varepsilon} = 10.644\ meV$), corresponding to the optical transition between the first two energy levels of the bare confining potential in the presence of the in-plane magnetic field, whose energy is $\varepsilon_1(k_x = 0) - \varepsilon_0(k_x = 0) = 10.648\ meV$. (Resonances to higher subbands are also possible, but have much smaller oscillator strength.) As N_s increases another resonance appears at an energy lower than ω_{K1}, and gradually moves to ω_{K1} while the other resonance also shifts to end up at ω_{K2} for high N_s. At a sheet density $N_s = 7.5 \times 10^{10}\ cm^{-2}$ (the highest N_s reported in the experiment) we obtain two resonances $\omega_{1,2}^{RES}$ very close to the "Kohn" frequencies $\omega_{K1,K2}$. We note that a direct comparison of the the-

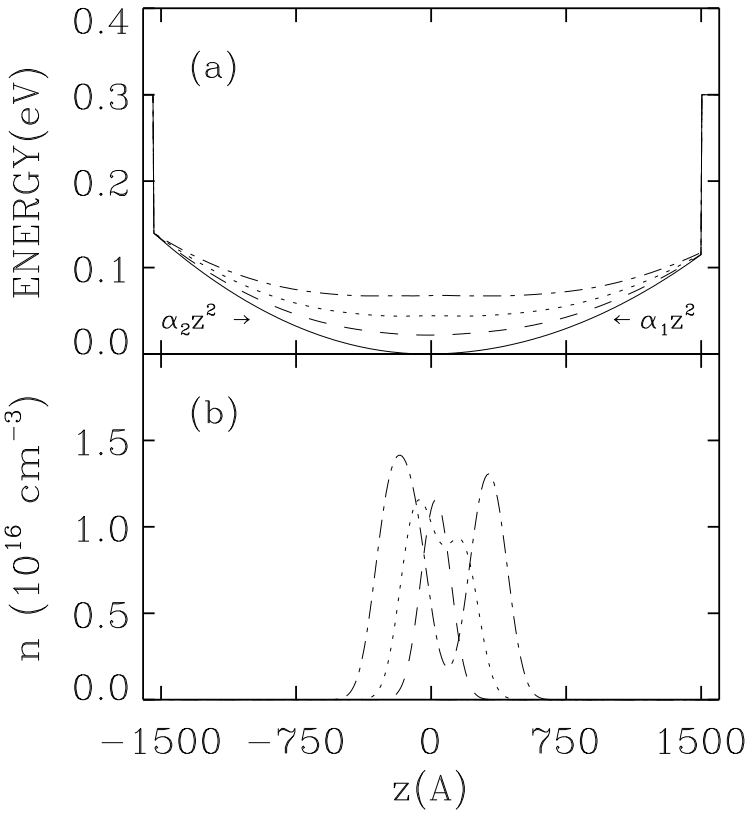

Figure 3.6: (a) Model bare potential of the asymmetric parabolic well (solid line), and calculated self-consistent potentials with an in-plane magnetic field of $B = 5.8T$, for $N_s = 2.4$ (dash line), 4.7 (dotted line), and 7.5×10^{10} cm^{-2} (dash-dot line); (b) corresponding calculated self-consistent densities.

oretical and calculated spectra is not possible because the experimental results correspond to a magnetic field sweep at a constant resonance frequency whereas the calculated optical spectra are given as a function of frequency at a fixed magnetic field. In order to make a quantitative comparison with experiment, we use the resonant frequencies $\omega_{1,2}^{RES}$ to compute the harmonic oscillator frequencies of the well halves $\omega_{1,2}^{CALC} = ((\omega_{1,2}^{RES})^2 - \omega_C^2)^{1/2}$, and obtain their difference $\omega_2^{CALC} - \omega_1^{CALC} = 0.378\ meV$. This shows an 8% discrepancy with the input value $\omega_2 - \omega_1 = 0.350\ meV$ ($\omega_{1,2}$ are the values used in the definition of the confining potential) which is comparable to the 4% discrepancy found in experiment between the design parameters and the observed resonances, at the same sheet density. The 8% theoretical discrepancy is expected to reduce further as the density N_S is increased and the electron gas covers to a larger extent the two halfs of the asymmetric parablic well.

Therefore, we obtain a very good agreement with the experimental results of Ref. [11] for low and high N_s. The agreement at high N_s also confirms the strong magnetic field classical arguments based on the Magarill-Chaplik [59] theory given in Ref. [11]. At intermediate N_s, however, the position of the weaker resonance seems to evolve in different ways as a function of N_s in theory and experiment. In the experiment, the two "Kohn" resonances found at high N_s appear to merge into one absorption peak as N_s is reduced, in contrast to the separation and vanishing of one of the resonances found in our calculation. Among the approximations incurred in our calculation which may be responsible for this discrepancy are the fact that spin effects are neglected, the temperature is assumed to be zero, and the general limitations of LDA (discussed in Appendix B) are operative here, with the aggravation that the exchange-correlation potential employed does not take

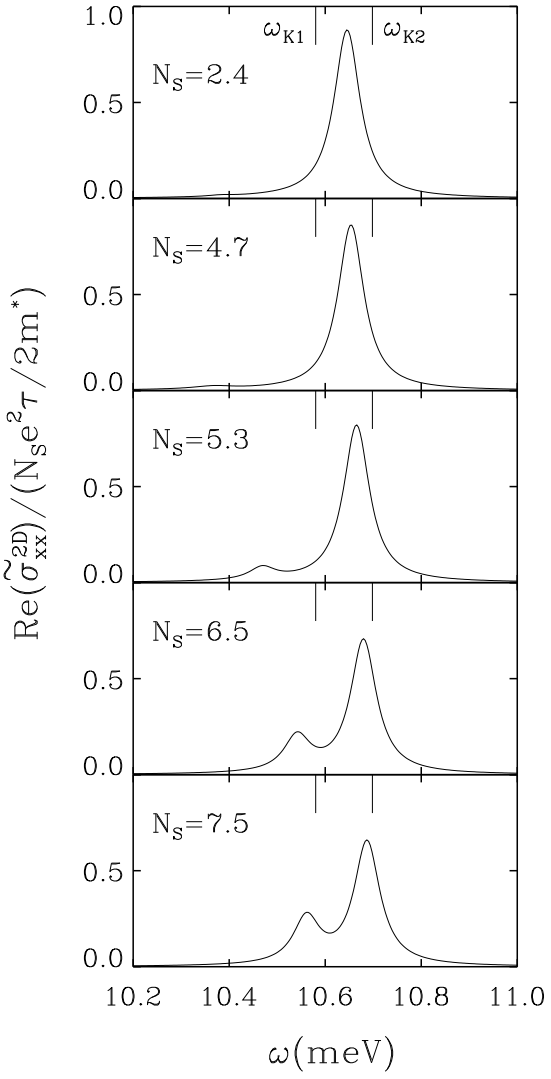

Figure 3.7: Calculated absorption spectra for the asymmetric parabolic quantum well with a magnetic field $B = 5.8T$ in the Voigt geometry for various areal densities N_s (given in units of $10^{10}cm^{-2}$). ω_{K1} and ω_{K2} are the "Kohn" frequencies associated with the curvatures of the two half-parabolas of the well.

into account explicitly the presence of a strong static magnetic field. Another possibility is that this discrepancy is only apparent and due to the differences in lineshapes of the resonances. These differences in lineshapes may be the result of the different type of spectra obtained in theory and experiment (frequency versus magnetic field sweep) and then an improved fit to the experimental results at intermediate N_s could be obtained if a magnetic field and density dependent scattering time $\tau(B, N_s)$ is included in the calculation.

Now we comment on two aspects of the collective excitations of the electron gas in the asymmetric parabolic well in the presence of an in-plane magnetic field. The CM mode predicted by the generalized Kohn's theorem for a perfect parabolic confinement is a rigid oscillatory motion of the electron slab. In linear response, its density fluctuations $\delta n(z)$ are proportional to $dn(z)/dz$, as illustrated in Fig. 3.5 for a perfect parabolic well. In Fig. 3.8 we show the fluctuation profiles $\delta n(z)$ for the resonant modes at $N_s = 7.5 \times 10^{10}\ cm^{-2}$ together with the derivative $dn(z)/dz$. We see that the resonant modes very accurately describe rigid translations of the electron gas in the corresponding halves of the well—right and left halves for the resonances with ω_{K1} and ω_{K2}, respectively. Finally, a notable difference between our results for the asymmetric PQW of Ref. [11] and a previous study of an overfilled PQW in the Voigt geometry [56] is the interplay between the main resonances or "Kohn modes" and the continuum of inter-Landau-level transitions. For the overfilled PQW the CM mode is broadened into a continuum, whereas for the asymmetric PQW the "Kohn modes" of the two half parabolas are split off from the continuum of inter-Landau-levels at high densities, and at lower densities one of them becomes a broad continuum resonance while the other one remains an isolated resonance as in the case of

perfect parabolic confinement. We mention that this interplay between the Kohn resonances and the continuum of single-particle modes may help explain the differences in linewidths between the two absorption peaks observed in experiment [11], and should be kept in mind in future extensions of the work presented here.

Figure 3.9 shows the calculated IR optical spectra for the asymmetric PQW without magnetic field for N_s in the range $0.1 - 1.6 \times 10^{11}\ cm^{-2}$. The number of occupied subbands goes from 1 to 4, and we keep 10 subbands in the calculation of the optical spectra. Again, for low N_s there is only one resonance corresponding to the lowest optical transition of the bare well, and at high N_s there are two resonances close to the frequencies ω_1 and ω_2. A surprising feature is the appearance of two resonances of similar weight at $N_s = 0.6 \times 10^{11}\ cm^{-2}$, when the second subband is populated, which disappears at higher N_s.

3.4 Summary

In this chapter we first presented a set of numerical results that illustrate the most salient features of quantum wells with a purely parabolic profile. Once the properties of the perfect parabolic wells were established, we studied the FIR optical absorption spectra of an asymmetric PQW with a magnetic field in the Voigt geometry and without a magnetic field using the self-consistent LDA approach. We compare our magnetic field results with recent experimental spectra and find good quantitative agreement with experiment for low and high N_s and quantitative differences in the spectra at intermediate N_s. The origin of this disagreement remains an open question, but can probably be attributed to the magnetic field sweep used in the experiment (rather than a frequency sweep), which could be taken into account in the calculation through a magnetic field

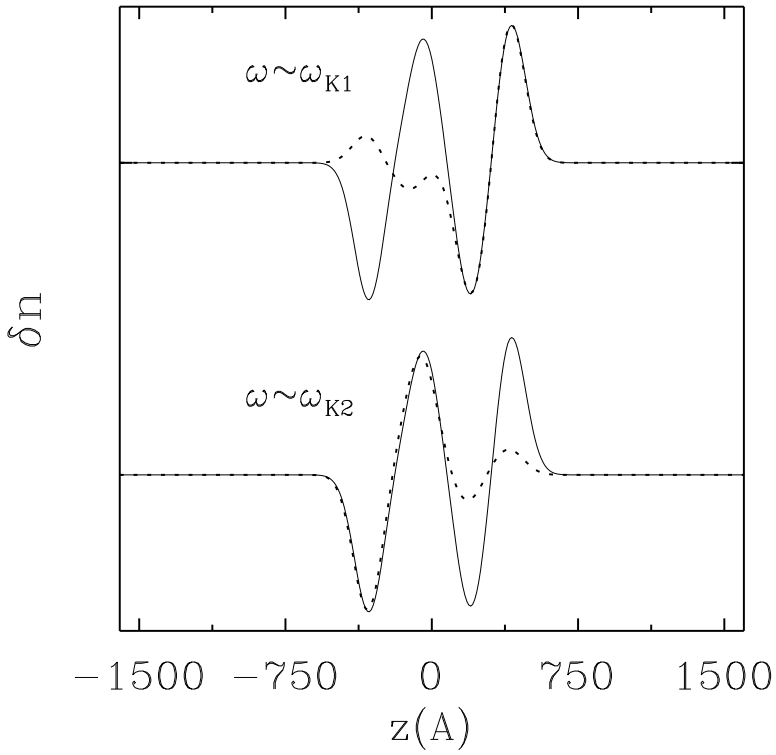

Figure 3.8: Density fluctuations $\delta n(z)$ (dotted lines) associated with the two absorption peaks at $N_s = 7.5 \times 10^{10}\ cm^{-2}$ shown in Fig. 3.7, and the derivative of the ground-state electron density $dn(z)/dz$ (solid lines). The partial agreements between $\delta n(z)$ and $dn(z)/dz$ show that the density fluctuations of each mode correspond to rigid oscillations of the electron slab on each half of the asymmetric well, in analogy to the center-of-mass mode present in perfect parabolic wells.

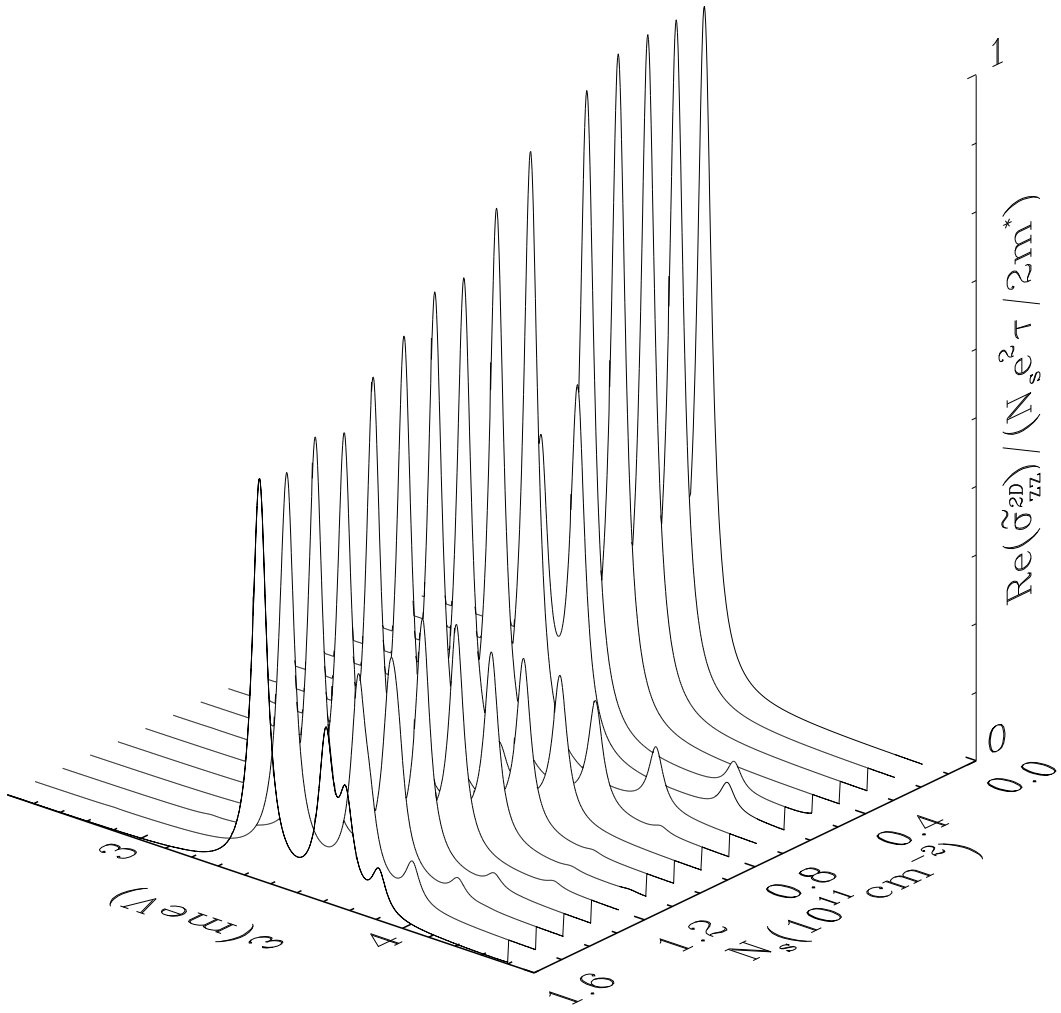

Figure 3.9: Calculated absorption spectra for the asymmetric parabolic quantum well without magnetic field for various sheet densities N_s. At high N_s the resonances agree with the curvatures of the well, $\omega_1 = 3.41\ meV$ and $\omega_2 = 3.76\ meV$.

and density dependent scattering time, or through a laborious calculation on a grid of magnetic field values. Also, a theory including finite temperatures and a treatment of exchange-correlation that takes into account explicitly the presence of the strong magnetic field may be necessary. From our calculations and the experimental results of Ref. [11], we conclude that asymmetric parabolic quantum wells are a simple but interesting departure from perfect parabolic quantum wells, where many-body effects show up in the FIR optical absorption spectra in a non-trivial way. Due to the simplicity of their spectra they constitute good systems to test the validity of different theoretical approaches to the inhomogeneous electron gas. At zero magnetic field, the general trends of the spectra are similar to those of the Voigt geometry results. We propose experimental measurements of the optical spectra at zero magnetic field, which would be useful to compare the accuracy of the LDA approximation with and without magnetic field (a grating coupler should be employed to induce intersubband transitions in the perpendicular incidence geometry.)

CHAPTER 4

Parabolic quantum wells with δ-planar perturbations

4.1 Introduction

An interesting application [16] of the idea of using a wide PQW to study the properties of a 3D electron gas in a strong magnetic field is the recent measurement of FIR spectra of samples with controlled δ-planar perturbations (thin layers of $Al_xGa_{1-x}As$ with a different concentration of aluminum which produce small spikes in the otherwise parabolic potential). Besides the expected Kohn mode, additional peaks appeared in the spectra, which, interpreted as collective excitations with a certain transversal wavevector q_z (to be suitably defined), permitted the construction of a "three dimensional" magnetoplasmon dispersion relation. The result showed a minimum around $q_z = 2/\ell_c$ ($\ell_c \equiv$ magnetic length) in agreement with the magneto-roton minimum predicted by the 3D calculation in the single-mode approximation [16]. In this chapter we apply the insight provided by a microscopic quantum mechanical calculation that takes into account the exact geometry of the experimental samples to test the validity of the assumptions underlying the interpretation of the experimental data made in Ref. [16] [15].

In that experimental study, the magneto-optical spectra of a quasi-2D electron gas confined in wide PQWs with δ-planar perturbations were obtained [16]. The

perturbations, deliberately grown in the PQW samples to "violate" the generalized Kohn theorem, allowed the coupling of long-wavelength radiation to the internal modes of oscillation of the electron gas. By assigning wavevectors $q_z = \frac{N\pi}{W}$, or $q_z = \frac{2\pi}{a}$ (W = width of the electron slab, a = spikes separation in δ-arrays samples), corresponding to dimensional resonances in the direction of confinement, it was possible to construct a dispersion relation for the magnetoplasma excitations in the electron gas. In this way, in Ref. [16] the experimental data were interpreted as the observation of a 3D magneto-roton minimum in the magnetoplasmon dispersion of a quasi-2D electron gas. We emphasize the important conceptual distinctions between our calculations and the theoretical interpretation used in the original work of Ref. [16]. We consider the *actual* experimental system which is a PQW quasi-2D electron gas with only a few quantum subbands occupied in the zero field (and only *one* magneto-subband populated under the magnetic field values used in the experiment) whereas in Ref. [16] the system was taken to be a purely 3D electron gas. We feel that the 3D approximation could apply [43] only when many subbands are occupied, and more importantly, only if our quasi-2D calculations support such a 3D picture. Our calculation is a fully self-consistent quasi-2D time-dependent local-density-approximation (TDLDA) which takes into account the detailed electronic structure of the system (including the δ-function or the superlattice perturbations) whereas in Ref. [16] a 3D single-mode-approximation was used. Finally, and this is a significant but subtle difference, our calculation is in the quasi-2D long-wavelength limit (because the wavevector associated with the incident far infrared radiation is effectively zero) whereas in Ref. [16] the bulk collective mode is taken to be excited at a finite 3D wavevector defined by the dimensional resonance $q_z = \frac{N\pi}{W}$, etc. Note that for the

confined quasi-2D PQW system q_z is not a well-defined concept for the collective modes.

The purpose of our study, thus, is twofold. On one hand, we intend to compare FIR absorption spectra calculated within the TDLDA with experimental results for parabolic wells with controlled superimposed perturbations in the electrostatic confining potential. This complements other theoretical studies of different types of deviations from perfect parabolicity available in the literature [58, 56, 44]. On the other hand, we examine the validity of constructing a 3D magnetoplasmon dispersion relation from the information provided by the confined intersubband excitations. We do so by calculating the microscopic density fluctuations associated with the various observable collective modes, and using them to introduce a simple definition of the "fictitious" wavevectors q_z. Ours is a generalization to the magnetic field case of the method of Teich and Mahler [43], whose results provided the heuristic basis for the analysis of the experimental data employed in Ref. [16].

4.2 Magneto-optical absorption spectra

In Fig. 4.1(a) we show our model bare potential for the PQW sample with a single δ-planar perturbation studied experimentally in Ref. [16]. The peak in the middle of the well is taken to have a Gaussian shape, and its strength is about six times larger than the value specified for the real sample. Also shown in Fig. 4.1(a) are the self-consistent potentials for the minimum and maximum areal densities used in the experiment, $N_s = 1.64 \times 10^{11}\text{cm}^{-2}$, and $2.24 \times 10^{11}\text{cm}^{-2}$, with an applied in-plane magnetic field of B = $5.4T$. Given that the location of the δ-peak is known in the experiment only within a 10% of the well width

[60], we also consider a PQW with a slightly off-centered δ-planar perturbation. The model PQW with a perturbation slightly displaced from the center of the well is shown in Fig. 4.1(c). The displacement is 130Å, somewhat larger than the magnetic length $\ell_c = (\frac{\hbar c}{eB})^{1/2} \approx 110$Å, but less than 10% of the well width. The ground state self-consistent electronic densities corresponding to our two model potentials are shown in Figs. 4.1(b) and (d). These self-consistent density profiles and the self-consistent effective potentials are calculated following the method described in Section 2.3.

The absorption spectra for the PQW with a centered spike, obtained employing the techniques described in Section 2.4, are shown in Fig. 4.2. At both densities we observe a strong peak corresponding approximately to the CM mode (Kohn mode) of frequency ω_K characteristic of perfect PQWs, in agreement with experiment. In our calculation the frequencies of these resonances are shifted away from ω_K, but the analogy with the CM mode is corroborated by the shape of their density fluctuations, which are approximately proportional to the derivative of the ground-state density $\frac{dn}{dz}$ (see Fig. 4.3(a)) as occurs in the center-of-mass motion. To decide whether the positions of the secondary resonances agree with experiment we need to consider that while our results are shown as functions of the resonant frequency, the transmission experiments were performed sweeping the magnetic field at a constant radiation frequency. Since the resonant frequencies increase monotonically with magnetic field (approximately as $\omega \approx (\omega_0^2 + \omega_c^2)^{1/2}$), an absorption peak falling on the low frequency side of the CM resonance in the calculated spectrum corresponds to a transmission peak on the high magnetic field side of the CM resonance in the experimental spectrum. We therefore verify that the relative positions

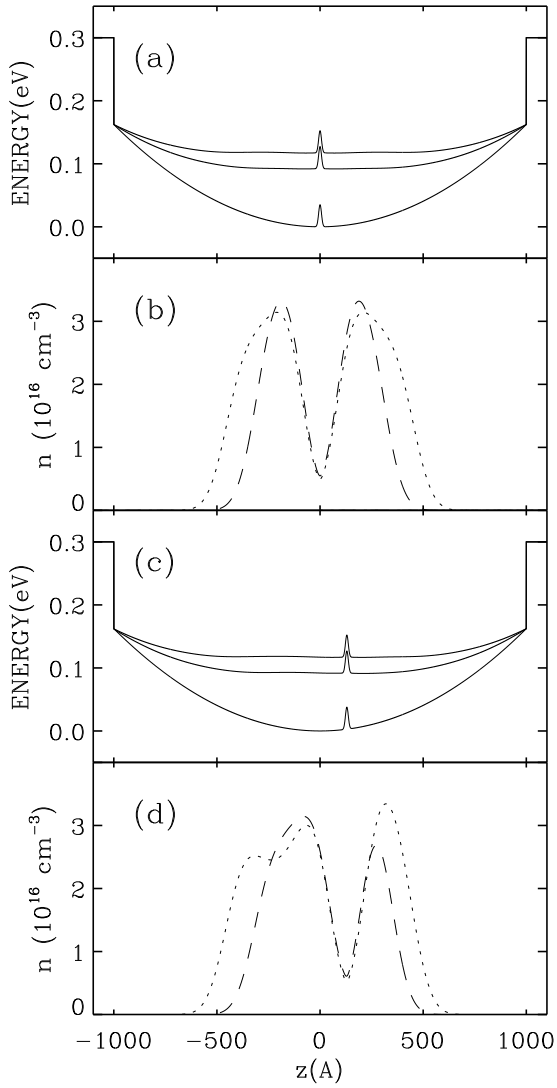

Figure 4.1: Model bare potential of the parabolic well with (a) a centered and (c) an off-centered δ-planar perturbation (bottom line), and calculated self-consistent potentials with an in-plane magnetic field of $B = 5.4T$, for $N_s = 1.64$ (middle line), and $2.24 \times 10^{11}\, cm^{-2}$ (top line); (b) and (d) show the calculated self-consistent densities corresponding to the potentials of Figs. (a) and (c), respectively, for $N_s = 1.64$ (dashed line) and $2.24 \times 10^{11}\, cm^{-2}$ (dotted line).

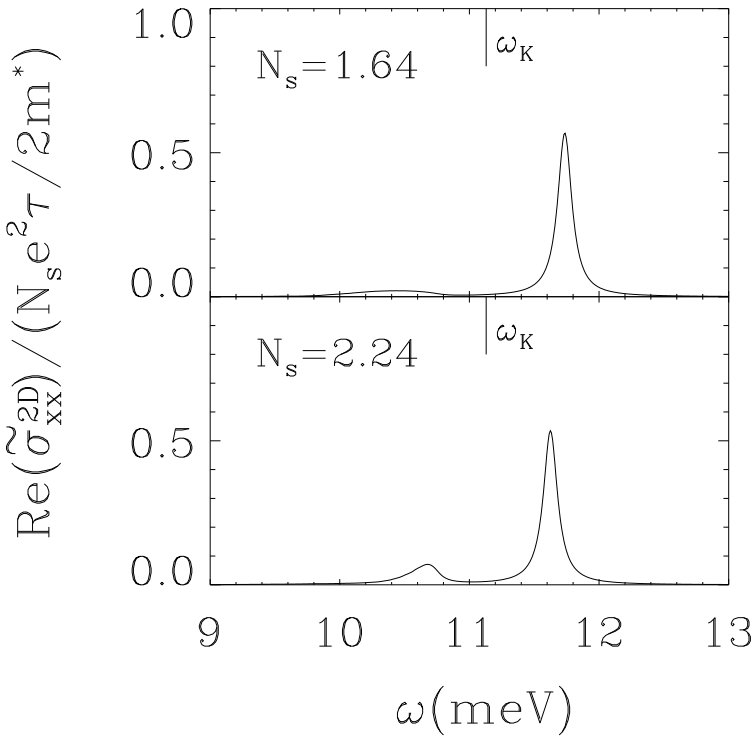

Figure 4.2: Calculated absorption spectra for the parabolic well with a centered δ-planar perturbation, with a magnetic field $B = 5.4T$ in the Voigt geometry for two different areal densities N_s (given in units of $10^{11}\,cm^{-2}$). The "Kohn" frequency $\omega_K = (\omega_0^2 + \omega_c^2)^{1/2}$ associated with the curvature of the well is shown as a reference.

of the secondary resonances in our calculation agree with those of the experiment. There is also agreement in the fact that both in theory and experiment the separation between the main and the secondary peaks decreases with increasing N_s. However, the theoretical separations, $\triangle\omega_{\rm calc} = 1.32$ and 1.0 meV for $N_s = 1.64$ and $2.24 \times 10^{11}{\rm cm}^{-2}$, respectively, are about a factor three larger than the experimental values $\triangle\omega_{\rm exp} = 0.48$ and 0.32 meV. Another discrepancy appears in the intensities of the secondary resonances: in the calculation, the secondary resonance at low N_s has less oscillator strength than the one at higher N_s, contrary to the experimental finding. A better agreement on these points will be found with the model potential with an off-centered spike.

Our calculations of the dynamical conductivity for the PQW with a centered δ-planar perturbation show a collective mode whose frequency lies between the two resonances observed in the spectra of Fig. 4.2, but with zero oscillator strength. This collective mode does not give rise to power absorption because the density fluctuations associated with it are symmetric with respect to $z = 0$, as shown in Fig. 4.3(b) (the density fluctuations shown in Fig. 4.3 are calculated using Eq. 2.84), and therefore cannot couple to long-wavelength radiation. In the model potential with an off-centered δ-planar perturbation the symmetry of the Hamiltonian is broken, and therefore such collective modes become visible in the absorption spectrum. The middle peaks in Fig. 4.4 correspond to the formerly forbidden symmetric modes, as can be verified from the form of their density fluctuation profiles (Fig. 4.3(b)). A comparison of the separations between the main resonance and the secondary ones gives now a substantially better agreement than with the centered perturbation. For $N_s = 1.64 \times 10^{11}{\rm cm}^{-2}$, $\triangle\omega_{\rm calc} = 0.43$ meV, whereas $\triangle\omega_{\rm exp} = 0.48$ meV, and for $N_s = 2.24 \times 10^{11}$ cm^{-2}, $\triangle\omega_{\rm calc} = 0.22$ meV

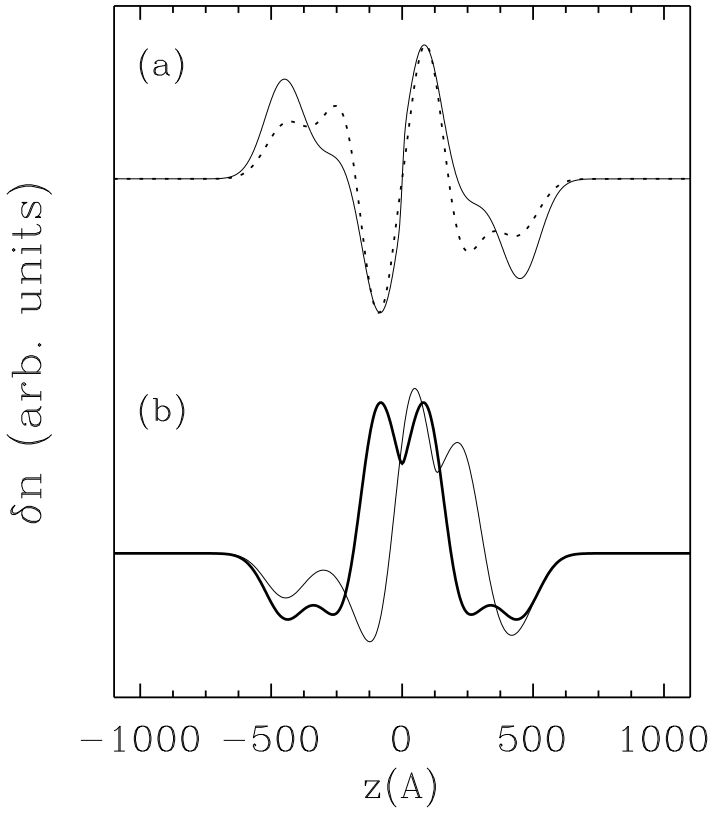

Figure 4.3: (a) Density fluctuations $\delta n(z)$ (dotted line) associated with the shifted "Kohn mode" for the potential with a centered δ-function perturbation, at $N_s = 2.42 \times 10^{11}\, cm^{-2}$, and the derivative of the equilibrium density $\frac{dn}{dz}$ (solid line). (b) The symmetry disallowed mode of the centered δ-function potential (thick line) and the corresponding resonant mode for the off-centered δ-function potential (thin line).

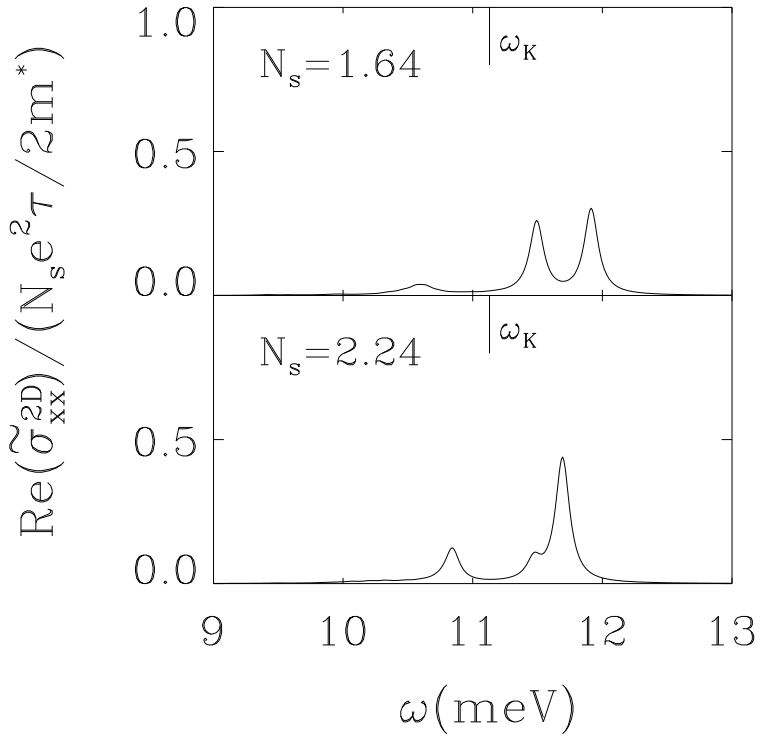

Figure 4.4: Calculated absorption spectra for the parabolic well with an off-centered δ-planar perturbation, with a magnetic field $B = 5.4T$ in the Voigt geometry for two different areal densities N_s (given in units of $10^{11}\,cm^{-2}$). The "Kohn" frequency $\omega_K = (\omega_0^2 + \omega_c^2)^{1/2}$ associated with the curvature of the well is shown for reference.

for the first peak and 0.86 meV for the second one, whereas $\triangle\omega_{\rm exp} = 0.32$ meV, and 0.71 meV, respectively.

We have also performed calculations of optical absorption spectra for a parabolic well with a periodic array of δ-planar perturbations with a distance between spikes $a = 300$Å. Using spike strengths ten times larger than in the experiment, we obtain a broad secondary peak whose energy is approximately equal to the cyclotron energy for two different areal densities. Consequently, its separation to the Kohn mode is independent of N_s, in qualitative agreement with the experimental spectra. However, this resonance is weaker than the experimental one, and its energy difference with the Kohn mode is somewhat larger than in the experiment. For a parabolic well with a periodic array of δ-planar perturbations with a distance between spikes $a = 200$Å, we also obtain a broad resonance around the cyclotron frequency. It should be emphasized, however, that the precise form of the perturbations in the experimental samples are, in general, unknown and, under the circumstances, our approximately quantitative agreement with experiment is all we can hope for.

4.3 Construction of a magnetoplasmon dispersion relation

In this section we use the theoretical results presented in Section 4.2 to examine the basic assumption made in the interpretation of the experimental data of Ref. [16], which made possible the construction of a "bulk" dispersion relation out of the measured energies of the confined intersubband collective excitations. This connection was established by assuming that the different resonances observed experimentally correspond approximately to sinusoidal standing waves in the electron density with wavevectors $q_z = \frac{N\pi}{W}$, or $q_z = \frac{2\pi}{a}$, where $W = N_s/n_0$

is the approximate width of the electron slab (n_0 is the design density of the parabolic well), N is an even integer, and a is the periodicity of the array of δ-spikes in the confining potential. This picture was motivated by the following points: (i) the fact that for perfect parabolic wells the ground state density profile is very uniform over most of the extent of the electron slab, and the assumption that such a uniform equilibrium density would not be substantially altered by the introduction of small perturbations; (ii) RPA calculations in square wells without magnetic fields, which show a remarkable agreement between the bulk plasmon dispersion relation and a dispersion relation constructed from intersubband excitation energies in a similar fashion; (iii) a hydrodynamic model calculation for perfect parabolic quantum wells in the presence of a magnetic field [61].

We employed the density fluctuations (see Eq. (2.84)) associated with the various secondary resonances described in the previous section, whose energies show a semiquantitative agreement with experiment, to construct a dispersion relation with two different definition of transverse wavevector q_z. (An example of such density fluctuations is shown in Fig. 4.3(b).) We introduce a simple definition of the wavevector in the z-direction, $q_z = 2\pi/\lambda$, where $\lambda \equiv 2W_{\delta n}/(M+1)$, $W_{\delta n}$ is the width of the density fluctuations and M is the number of nodes. The resulting dispersion relation is shown as empty symbols in Fig. 4.5. We plot the same data points with q_z defined as in Ref. [16] as solid symbols. As a caveat we mention that the four points with smaller q_z have been shifted down in energy by an amount equal to the displacement of the Kohn modes from their theoretical values. This correction seems justified since we verified that the same potentials with smaller spikes do not have their Kohn modes displaced from the expected values. The solid line is the 3D RPA magnetoplasmon dispersion [62]. It can be seen that the

two definitions of q_z give a reasonable agreement with each other and with the bulk RPA result. It should be mentioned that within our TDLDA calculation we expect qualitative agreement with the RPA dispersion relation, and not with the one obtained in the single-mode approximation [16], since the vertex corrections included in TDLDA are q-independent, and therefore cannot change the dispersion relation of the collective modes. For this reason, the roton-minimum feature obtained in the single-mode approximation is not expected to appear in our constructed dispersion relation. Rather, our main conclusion is that, in the presence of a magnetic field, the intersubband collective modes can be interpreted as bulk magnetoplasma modes by assigning to them suitable wavevectors, and the dispersion relation obtained in this fashion agrees qualitatively with the bulk result obtained if the same theoretical scheme (in our case, the RPA with local vertex-corrections) is used in the bulk calculation. Our resuls can be taken as a generalization of the work of Teich and Mahler [43] (which treats the connection between intersubband plasmons and bulk plasmons without magnetic field) to the magnetic field case, within the random-phase approximation. Therefore, our analysis supports, at least qualitatively, the method used in Ref. [16] to relate the FIR absorption data to the 3D single-mode approximation calculation. However, we feel that this type of interpretation of the long wavelength quantum confined quasi-2D collective intersubband charge density excitation modes, should be taken with caution, due to the ambiguity in the definition of the transverse wavevectors q_z. At this stage we can say, at most, that such an interpretation would be meaningful only if it is supported by a microscopic calculation that takes into account the exact geometry of the problem, like the one presented here.

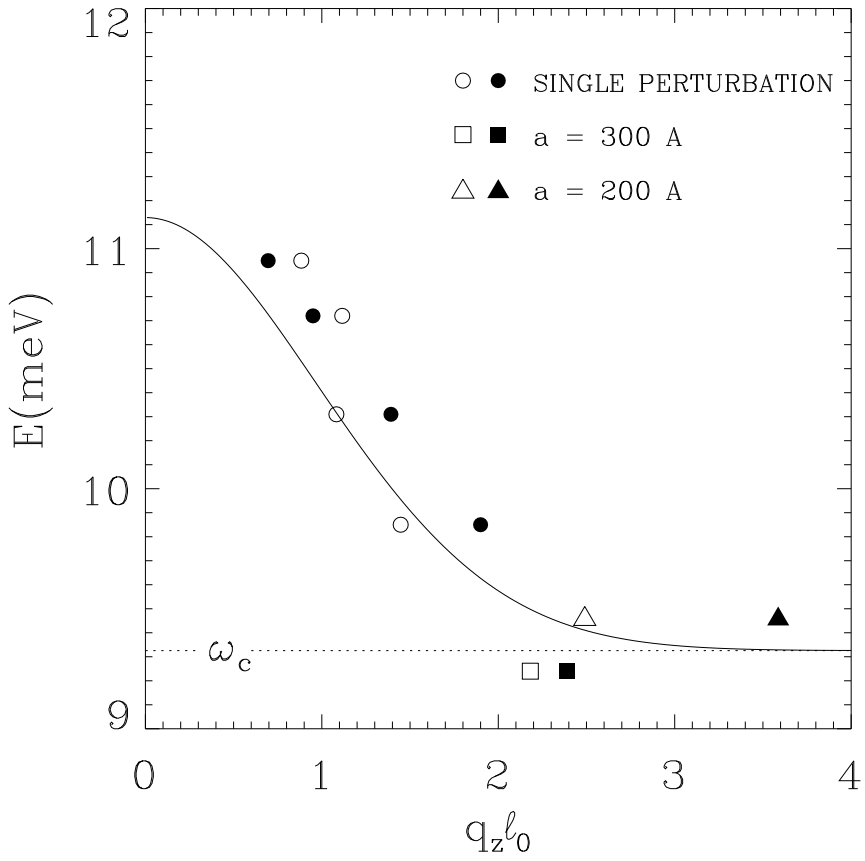

Figure 4.5: Magnetoplasmon dispersion relation constructed by assigning simply defined transverse wavevectors q_z to the intersubband charge density excitations of various PQW with δ-planar perturbations. Open symbols correspond to the q_z extracted from the calculated density fluctuations, and solid symbols correspond to the definitions of q_z used in Ref. [16] (see text). The solid line gives the bulk RPA magnetoplasmon dispersion at a 3D density equal to the design density of the PQW.

4.4 Summary

In this chapter we have studied theoretically within the TDLDA formalism the properties of the collective modes of parabolic wells with δ–planar perturbations, as manifested in long-wavelength magneto-optical absorption experiments. Our TDLDA calculations of the spectra for parabolic PQW with a small perturbation in the middle of the well are in good semi-quantitative agreement with experiment. This agreement is considerably improved if the perturbation is placed slightly off-centered, in which case formerly symmetry disallowed modes appear in the spectra. This interpretation could be further investigated experimentally if the position of the δ-planar perturbation is varied systematically around the center of the well, thus controlling the strength of the symmetric mode. We constructed a magnetoplasmon dispersion relation by assigning transverse wavevectors q_z to the inter-Landau level resonances, which displays a reasonable qualitative agreement with the bulk RPA result. This analysis provides some support for the interpretation of experimental results as the observation of a magneto-roton feature in the magneto-plasmon dispersion relation of a 3D electron gas predicted by a single-mode approximation calculation [16].

CHAPTER 5

Theory of resonant inelastic light-scattering in quasi-two dimensional systems

In this chapter we introduce the theoretical description of inelastic-light-scattering experiments in semiconductor quantum wells. This theory will be applied in Chapters 6 and 7 to coupled double-quantum-well systems. We will present briefly the basic equations that describe light scattering by a free electron gas, and the crucial band-structure effects in bulk systems. Once this background is layed out, we will present the calculation of the appropriate response functions which describe the many-body effects of electronic light scattering in quasi-two dimensional systems. The latter is the part of the light scattering analysis that contains the physics of electronic intersubband transitions we are interested in.

5.1 Light scattering by a free electron gas

First we consider the case of light scattering by a free electron gas. The Hamiltonian of a free electron gas coupled to an electromagnetic field $\mathbf{A}$ is

$$\begin{aligned} H_{TOTAL} &= \sum_i \frac{\left(\mathbf{p}_i - \frac{e}{c}\mathbf{A}_i\right)^2}{2m^*} + \frac{1}{2}\sum_{i\neq j}\frac{e^2}{\epsilon\, r_{ij}} \\ &\equiv \quad H - \frac{e}{2m^*c}\sum_i \mathbf{p}_i\cdot\mathbf{A}_i - \frac{e}{2m^*c}\sum_i \mathbf{A}_i\cdot\mathbf{p}_i + \frac{e^2}{2m^*c^2}\sum_i A_i^2, \end{aligned} \quad (5.1)$$

where we have explicitly separated the electron-photon coupling terms. There are linear coupling terms, of the form $\mathbf{p}_i \cdot \mathbf{A}_i$, and quadratic ones, of the form $\mathbf{A}_i^2$. It can be shown that [63] for the free electron system the A_i^2 terms are the dominant ones, because the $\mathbf{p} \cdot \mathbf{A}$ terms cancel each other to order v/c, where v is the electron velocity. Once the negligible terms in the perturbation Hamiltonian are removed, one calculates the scattering cross section of light by applying time-dependent perturbation theory, that is, the Fermi Golden Rule. In the case of light scattering by a single free electron (non-relativistic Compton scattering), keeping only the $|A|^2$ term, the scattering cross section reduces to

$$\frac{d\sigma}{d\omega} = \left(\frac{e}{m^* c^2}\right)^2 (\boldsymbol{\epsilon_1} \cdot \boldsymbol{\epsilon_2})^2, \tag{5.2}$$

where $\boldsymbol{\epsilon_1}$ and $\boldsymbol{\epsilon_2}$ are the polarization vectors of the incident and scattered light waves, of frequency ω_1 and ω_2, and momentum $\mathbf{k_1}$ and $\mathbf{k_2}$, respectively. This expression is known as the Thompson formula, and can be derived in a number of different ways. For the full many-body system, when the electron-electron interactions are taken into account, the differential cross-section for scattering into a solid angle $d\Omega$ and frequency interval $d\omega$ becomes

$$\frac{d^2\sigma}{d\Omega\, d\omega} = \left(\frac{e}{m^* c^2}\right)^2 \left(\frac{\omega_2}{\omega_1}\right) (\boldsymbol{\epsilon_1} \cdot \boldsymbol{\epsilon_2})^2\, S(\mathbf{k}, \omega), \tag{5.3}$$

where $\omega = \omega_1 - \omega_2$ and $\mathbf{k} = \mathbf{k}_1 - \mathbf{k}_2$ are the energy and momentum transferred to the scatterers. The *dynamic structure factor* $S(\mathbf{k}, \omega)$ carries the information related to the interactions in the electron gas, and is defined as

$$S(\mathbf{k}, \omega) \equiv \frac{1}{2\pi} \int_{-\infty}^{\infty} dt\, e^{i\omega t} \langle n_{\mathbf{k}}(t)\, n_{-\mathbf{k}}(0) \rangle, \tag{5.4}$$

where the brackets indicate a thermal average over initial electron states,

$$n_{\mathbf{k}} \equiv \sum_i e^{-i\mathbf{k}\cdot\mathbf{r}_i} = \int_{-\infty}^{\infty} d^3r\, e^{-i\mathbf{k}\cdot\mathbf{r}}\, n(\mathbf{r}) = \sum_{\mathbf{q}\alpha} c^\dagger_{\mathbf{q}+\mathbf{k}\alpha} c_{\mathbf{q}\alpha}, \tag{5.5}$$

is the Fourier transform of the electron density operator, and

$$n_{\mathbf{k}}(t) \equiv exp(iHt)\, n_{\mathbf{k}}\, exp(-iHt) \tag{5.6}$$

is the time-dependent version of $n_{\mathbf{k}}$. The dynamic structure factor is therefore the space-time Fourier transform of the electron density-density correlation function:

$$S(\mathbf{k},\omega) = \frac{1}{2\pi}\int_{-\infty}^{\infty} dt\, e^{i\omega t}\int_{-\infty}^{\infty} d^3r\, d^3r' e^{-i\mathbf{k}\cdot(\mathbf{r}-\mathbf{r}')}\,\langle n(\mathbf{r},t)\, n(\mathbf{r}',0)\rangle. \tag{5.7}$$

Eqs. (5.3) and (5.7) indicate that electron-density fluctuations are responsible for the scattering of a light wave in a free electron gas; this is also the case in electron-beam scattering experiments [63]. If the polarizability response function $\tilde{\Pi}(\mathbf{k},\omega)$ is defined as the proportionality factor between an applied external potential $\phi_{\text{ext}}(\mathbf{k},\omega)$ and the induced charge fluctuations $\rho_{\text{ind}}(\mathbf{k},\omega)$, the fluctuation-dissipation theorem establishes the following relation between $S(\mathbf{k},\omega)$ and $\tilde{\Pi}(\mathbf{k},\omega)$ [63]:

$$e^2 S(\mathbf{k},\omega) = \frac{1}{\pi e^{-\beta\omega}-1}\, Im\left[\tilde{\Pi}(\mathbf{k},\omega)\right], \tag{5.8}$$

where $\beta = 1/k_B T$. The polarizability $\tilde{\Pi}(\mathbf{k},\omega)$, which gives the response to an *external* (as opposed to *total = external + induced*) potential, is called, in the language of many body-quantum mechanics, a *reducible* response function.

5.2 Band-structure effects

The free electron gas treatment is valid when the energy of the light is smaller than the energy gap of the semiconductor ($E_G < 2\, eV$), because only in that case virtual transitions between the valence and conduction bands can be ignored. Also, the analysis based on the free electron gas misses two important features of light scattering by electrons in a real solid: the resonant nature of the transitions

and the possibility of spin-density fluctuations. In the following, we give highlights of the theory of light scattering including the crystal band structure, which incorporates these effects. We begin by neglecting electron-electron interactions and assume that the electrons in a crystal can be described by the single particle Hamiltonian

$$H = \frac{p^2}{2m^*} + V(\mathbf{r}) + \frac{\hbar}{4m^2c^2}\left(\boldsymbol{\nabla} V \times \mathbf{p} \cdot \boldsymbol{\sigma}\right), \tag{5.9}$$

where $V(\mathbf{r})$ is the periodic crystal potential and the last term is the spin-orbit coupling [64], which includes the Pauli spin operator $\boldsymbol{\sigma} = (\sigma_x, \sigma_y, \sigma_z)$. The solutions of the Schrodinger equation

$$H\phi_{\mathbf{p},\mu} = E_\mu(\mathbf{p})\,\phi_{\mathbf{p},\mu} \tag{5.10}$$

are the Bloch waves $\phi_{\mathbf{p},\mu}$, of crystal momentum $\mathbf{p}$ in band μ, with eigenenergies $E_\mu(\mathbf{p})$. We couple the Bloch electrons to the light field $\mathbf{A}$ by replacing $\mathbf{p} \to \mathbf{p} - \frac{e}{c}\mathbf{A}$ in Eq. (5.9). As in the free electron gas case, we have linear and quadratic electron-photon interaction terms in the Hamiltonian. The $\mathbf{p} \cdot \mathbf{A}$ type of term takes the form

$$-\frac{e}{mc}\left[\mathbf{p} + \frac{h}{4mc^2}\boldsymbol{\sigma} \times \boldsymbol{\nabla} V\right] \cdot \mathbf{A} \equiv -\frac{e}{c}\mathbf{v} \cdot \mathbf{A} \tag{5.11}$$

where we introduced the velocity operator $\mathbf{v}$, and the quadratic terms are $\frac{e^2A^2}{2mc^2}$, as before. The cancellation of the $\mathbf{v} \cdot \mathbf{A}$ terms that occurred in the free electron gas persists in the Bloch-electron problem in the *intraband* transitions, but not in the *interband* matrix elements. The essential features we are interested in can be found in a simplified two-band model, where the conduction band and a lower-lying valence band, separated by the energy gap E_G, are kept. Within this two-band model, the total matrix element for light scattering, including the

interband terms and the A^2 terms is given by [63]

$$M \simeq \left(\frac{e}{c}\right)^2 \frac{2\pi\hbar c^2}{\sqrt{\omega_1\,\omega_2}} \left\{ \frac{\boldsymbol{\epsilon_1}\cdot\boldsymbol{\epsilon_2}}{m^*} \left[\left(\frac{E_G^2}{E_G^2-\omega_1^2}\right)\left(\frac{1}{m^*}-\frac{1}{m}\right)+\frac{1}{m}\right] + \left(1-\frac{m_s}{m}\right)\left(\frac{\omega_1 E_G}{E_G^2-\omega_1^2}\right)\frac{\boldsymbol{\sigma}\cdot(\boldsymbol{\epsilon_1}\times\boldsymbol{\epsilon_2})}{m_s}\right\} \tag{5.12}$$

where an effective mass m^* depending on the full band structure, and the spin mass m_s (related to the g factor by $|g| = \frac{2m}{m_s}$) have been introduced. Equation (5.12) has the two interesting features we are looking for: (i) the matrix element is enhanced by the resonant factor $E_G^2/(E_G^2-\omega_1^2)$ for incident light with frequency $\omega_1 \sim E_G$. This enhancement is the key to the observability of light scattering from semiconductor heterostructures, where the number of scatterers is much smaller than in bulk semiconductors; (ii) the spin-dependent term in M that suggests the possibility of spin-flip light scattering. The two terms of Eq. (5.12), being proportional to $\boldsymbol{\epsilon_1}\cdot\boldsymbol{\epsilon_2}$ and $\boldsymbol{\epsilon_1}\times\boldsymbol{\epsilon_2}$, give rise to the two types of spectra that are usually measured in inelastic light-scattering experiments. *Polarized* spectra are obtained with the incident and scattered light polarizations parallel to each other, and are interpreted as *charge-density excitations*. In *depolarized* spectra, the two polarizations are perpendicular to each other, and were interpreted for the first time as *spin-density excitations* by Hamilton and McWhorter [65, 66, 67, 68, 69].

So far, our discussion of light scattering in the presence of a crystal lattice was restricted to noninteracting electrons. To understand the origin and to calculate the spectrum of charge-density and spin-density excitations we need to include electron-electron interactions. In our discussion of light scattering by a free electron gas including interactions we saw that the scattering mechanism was related to the coupling of light with the electron density operator $n_{\mathbf{q}} = \sum_{\mathbf{k}} c^\dagger_{\mathbf{k}+\mathbf{q}} c_{\mathbf{k}}$. When the semiconductor band structure is considered, one needs to generalize the coupling mechanisms to describe light scattering due to $|\alpha\rangle \rightarrow |\beta\rangle$ electronic

transitions, where $|\alpha\rangle$ and $|\beta\rangle$ are Bloch states. Momentum and spin are included in α and β.

It is possible to combine the treatment of the $\mathbf{p}\cdot\mathbf{A}$ and $|A|^2$ type of terms of the Hamiltonian (see Eq. (5.1)) by defining a generalized density operator as [67]

$$N = \sum_{\alpha\beta} \gamma_{\alpha\beta}\, c^{\dagger}_{\beta}\, c_{\alpha}, \tag{5.13}$$

$$\begin{aligned}\gamma_{\alpha\beta} &= (\boldsymbol{\epsilon_1}\cdot\boldsymbol{\epsilon_2})\,\xi_{\alpha\beta} + \\ &+\frac{1}{m}\sum_{\beta'}\frac{\langle\alpha|\boldsymbol{\epsilon_2}\cdot\mathbf{p}e^{-\mathbf{k}_2\cdot\mathbf{r}}|\beta'\rangle\langle\beta'|\boldsymbol{\epsilon_1}\cdot\mathbf{p}e^{-\mathbf{k}_1\cdot\mathbf{r}}|\beta\rangle}{\hbar\omega_1 + E_\beta - E_{\beta'}} + \\ &+\frac{1}{m}\sum_{\beta'}\frac{\langle\alpha|\boldsymbol{\epsilon_1}\cdot\mathbf{p}e^{-\mathbf{k}_1\cdot\mathbf{r}}|\beta'\rangle\langle\beta'|\boldsymbol{\epsilon_2}\cdot\mathbf{p}e^{-\mathbf{k}_2\cdot\mathbf{r}}|\beta\rangle}{E_\beta - E_{\beta'} - \hbar\omega_2},\end{aligned} \tag{5.14}$$

where $|\beta'\rangle$ are intermediate states, E_β and $E_{\beta'}$ are one electron energies and $\xi_{\alpha\beta} = \langle\alpha|exp(-i\mathbf{q}\cdot\mathbf{r})|\beta\rangle$. The first term of $\gamma_{\alpha\beta}$ is the only one we kept in the analysis of light scattering by a free electron gas, and the remaining terms describe the *virtual* transitions, both intra- and inter-band. As an aid for the visualization of the resonant light scattering process we illustrate in Fig. 5.1 *virtual interband* transitions that enter in the calculation of $\gamma_{\alpha\beta}$; note that, however, the complete process illustrated amounts to an *intra-*(conduction)*band* transition. It is very difficult to evaluate $\gamma_{\alpha\beta}$ exactly because it depends on the details of the electron energy level structure [70]. Hamilton and McWhorter [65] calculated it using the electron wave functions of the Kane model, obtaining [67]

$$\gamma_{\alpha\beta} = \boldsymbol{\epsilon_1}\cdot\boldsymbol{\epsilon_2}\, A\,\xi_{\alpha\beta} + i\,\boldsymbol{\epsilon_1}\times\boldsymbol{\epsilon_2}\cdot\langle s_\alpha|\boldsymbol{\sigma}|s_\beta\rangle\, B\,\xi_{\alpha\beta} \tag{5.15}$$

where s_α and s_β are spin indices, and A and B are factors that contain the momentum matrix elements and resonant denominators of the form $(E_G^2 - \omega_1^2)$ (A and B are scalars if the valence bands are isotropic. For brevity, we will not write them down here [67]).

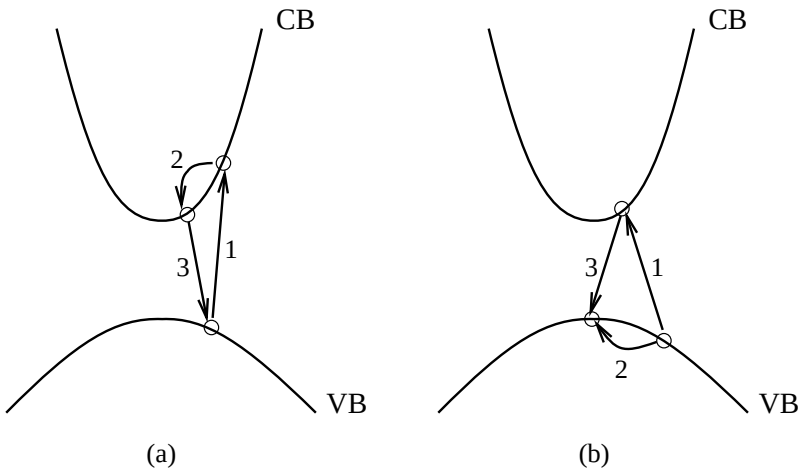

Figure 5.1: Schematic diagram of interband and intraband transitions which play a role in *two-band* Raman processes. The numbers indicate the order of the electronic transitions. (From Ref. [71].)

In terms of N one can define an effective perturbation Hamiltonian

$$H_{\text{eff}} = \frac{e^2}{2m}\,\mathcal{A}(\omega_1)\,\mathcal{A}(\omega_2)\,N, \tag{5.16}$$

where $\mathcal{A}(\omega) = (\hbar/\varepsilon(\omega_1)V\omega_1)$, V is the volume, and $\varepsilon(\omega)$ is the dielectric constant at ω. Employing H_{eff} the differential light-scattering cross section becomes

$$\frac{\partial^2\sigma}{\partial\Omega\partial\omega} = \left(\frac{\hbar}{mc^2}\right)\left(\frac{\omega_2}{\omega_1}\right)V^2\,G(\omega), \tag{5.17}$$

$$G(\omega) \equiv \frac{1}{2\pi}\int_{-\infty}^{\infty} dt\, e^{i\omega t}\,\langle N(t)\,N^{\dagger}(0)\rangle. \tag{5.18}$$

These two expressions are a generalization of Eqs. (5.3) and (5.4). The first term of $\gamma_{\alpha\beta}$ (Eq. (5.15)) gives rise to a component of the correlation function G, and hence, of the cross section, which is associated with charge-density fluctuations. This contribution is analogous to the cross section given in Eq. (5.3) for the free electron gas case. Similarly, it is possible to apply to the present case the

fluctuation-dissipation theorem to show that the cross section is proportional to the imaginary part of the polarizability response function of the electron gas. The second term of $\gamma_{\alpha\beta}$ (Eq. (5.15)) is the one responsible for changes in the electron spin and gives rise to spin-density excitations. For light incident with wavevector $\mathbf{k}_1 \parallel \hat{\mathbf{z}}$ (a common situation in experiments of scattering by 2-dimensional systems), we have $\boldsymbol{\epsilon_1} \times \boldsymbol{\epsilon_2} \parallel \hat{\mathbf{z}}$, and therefore only σ_z appears in Eq. (5.15). The effective Hamiltonian originating from the spin-dependent term of $\gamma_{\alpha\beta}$ is in this case [67]

$$H_{\text{eff}}^{\text{spin}} = i\,\frac{e^2V}{2m}\,(\boldsymbol{\epsilon_1} \times \boldsymbol{\epsilon_2}) \cdot \hat{\mathbf{z}} \left(\frac{N_\uparrow(\mathbf{q}) - N_\downarrow(\mathbf{q})}{2}\right) \mathcal{A}(\omega_1)\,\mathcal{A}(\omega_2). \tag{5.19}$$

The spin-density fluctuations operator $\frac{1}{2}(N_\uparrow(\mathbf{q}) - N_\downarrow(\mathbf{q}))$, where $N_\uparrow(\mathbf{q})$ and $N_\downarrow(\mathbf{q})$ are the electron-density fluctuations operators for each value of spin, indicate that $H_{\text{eff}}^{\text{spin}}$ gives rise to light scattering by spin-density fluctuations. This can also be seen by substituting the second term of Eq. (5.15) for $\gamma_{\alpha\beta}$ in the definition of N Eq. (5.13). We obtain

$$N = i\,B\,(\boldsymbol{\epsilon_1} \times \boldsymbol{\epsilon_2}) \cdot \sum_{\alpha\beta} \langle\alpha|e^{-i\mathbf{q}\cdot\mathbf{r}}\,\boldsymbol{\sigma}|\beta\rangle c_\beta^\dagger\, c_\alpha. \tag{5.20}$$

With this expression for N, the correlation function G is seen to be a Pauli paramagnetic susceptibility, which, in many-body diagrammatic language can be expressed as the *irreducible* polarization diagram [26].

5.3 Response functions

In the previous section we saw that the light-scattering intensity in the *polarized* and *depolarized* configurations are proportional to the *reducible* and *irreducible* polarizability functions of the electron gas, respectively. In this dissertation, we calculate the response functions of the electron gas in the so-called

time-dependent local-density approximation, which corresponds to calculating the irreducible polarizability function including a static and q-independent vertex correction in the ladder diagram approximation [27]. (Many-body diagrams describing our calculational scheme are given in Appendix B.) Within this approximation, the vertex integral equation for the irreducible polarizability $\Pi(q,\omega)$ can be solved exactly and gives

$$\Pi(q,\omega) = \frac{\Pi^0(q,\omega)}{1 + U_{xc}\,\Pi^0(q,\omega)}, \tag{5.21}$$

where $\Pi^0(q,\omega)$ is the leading-order polarizability function and U_{xc} is the static and q-independent vertex function (below we give expressions for these functions in the subband representation). From Dyson's equation for the effective Coulomb interaction [25] one obtains the reducible polarizability function

$$\tilde{\Pi}(q,\omega) = \frac{\Pi(q,\omega)}{1 - U_c(q)\,\Pi(q,\omega)}, \tag{5.22}$$

where $U_c(q)$ is the Fourier transform of the bare Coulomb interaction. Combining Eqs. (5.21) and (5.22) we obtain

$$\tilde{\Pi}(q,\omega) = \frac{\Pi^0(q,\omega)}{1 - (U_c(q) - U_{xc})\,\Pi^0(q,\omega)}. \tag{5.23}$$

In a confined electron gas system, where the confinement discretizes the single particle energy levels, the collective excitations have to be calculated in the generalized dielectric function formalism [72]. In this context, the functions U_{xc} and $U_c(q)$ are replaced by matrices where the indices label the different subbands. Within TDLDA we have

$$U^{XC}_{ij,mn} = -\int dz \int dz' \phi_i(z)\,\phi_j(z) \frac{\partial v_{xc}}{\partial n}(z) \delta(z-z')\,\phi_m(z')\,\phi_n(z') \tag{5.24}$$

and

$$U^{H}_{ij,mn}(q) = \frac{2\pi e^2}{\epsilon q} \int dz dz' \phi_i(z)\,\phi_j(z)\,e^{-q|z-z'|}\,\phi_m(z')\,\phi_n(z'). \tag{5.25}$$

$U^H_{ij,mn}$ is the matrix element of the Coulomb interaction in the subband representation, corresponding to $U_c(q)$ in Eq. (5.22), and ϵ is the background dielectric constant. The reducible polarizability function $\tilde{\Pi}(\mathbf{q}, q_z, \omega)$, whose imaginary part is proportional to the spectrum of the charge-density excitations and the Raman intensity in the polarized configuration is given by [73]:

$$\tilde{\Pi}(\mathbf{q}, q_z, \omega) = \int dz \int dz' e^{-iq_z(z-z')}\, \tilde{\Pi}(z, z'; \mathbf{q}, \omega), \tag{5.26}$$

where

$$\tilde{\Pi}(z, z'; \mathbf{q}, \omega) = \sum_{i,j,k,l} \phi_i(z)\, \phi_j(z)\, \tilde{\Pi}_{ij,kl}(\mathbf{q}, \omega)\, \phi_k(z')\, \phi_l(z'), \tag{5.27}$$

$$\tilde{\Pi}_{ij,kl}(\mathbf{q}, \omega) = \Pi^0_{ij}(\mathbf{q}, \omega)\, \delta_{ik}\, \delta_{jl} + \sum_{m,n} \Pi^0_{ij}(\mathbf{q}, \omega)\, U_{ij,mn}(q)\, \tilde{\Pi}_{mn,kl}(\mathbf{q}, \omega), \tag{5.28}$$

$$U_{ij,mn}(\mathbf{q}) = U^H_{ij,mn}(\mathbf{q}) - U^{XC}_{ij,mn}, \tag{5.29}$$

and

$$\Pi^0_{ij}(\mathbf{q}, \omega) = 2 \sum_{\mathbf{k}} \frac{f(E_j(\mathbf{k}+\mathbf{q})) - f(E_i(\mathbf{k}))}{E_j(\mathbf{k}+\mathbf{q})) - E_i(\mathbf{k})) - \hbar(\omega + i\gamma)}. \tag{5.30}$$

In these equations, subscripts are the subband indices, vectors $\mathbf{q}$ and $\mathbf{k}$ are two-dimensional in-plane wavevectors, and ϕ_j and ε_j are the LDA-calculated subband wavefunctions and energies. Π^0_{ij} is the leading-order polarizability function for the transition $i \to j$, and $E_j(\mathbf{k}) = \varepsilon_j + \frac{\hbar^2 k^2}{2m^*}$, and $f(E)$ is the Fermi factor. We also introduced an inverse phenomenological scattering time γ. We note that the random-phase approximation (RPA) is obtained in the subband representation by removing the vertex correction $U^{XC}_{ij,mn}$ in Eq. (5.29). As mentioned earlier, the imaginary part of the irreducible polarizability function Π is proportional to the spin-density excitation spectrum and the Raman-scattering intensity in the depolarized configuration. In the subband representation, the irreducible polarizability function Π is calculated exactly like $\tilde{\Pi}$ above, but setting $U^H_{ij,mn} = 0$

in Eq. (5.29), as can be seen by comparison with Eqs. (5.21) and (5.22). Setting $U^H_{ij,mn} = 0$ amounts to physically eliminating the dynamic screening which originates in electron-density fluctuations, which are absent in the spin-density excitations.

The CDE and SDE energies are given by the poles of $\tilde{\Pi}$ and Π, respectively, which occur where the determinant $|\Pi^0_{ij}U_{ij,mn} - \delta_{ij,mn}|$ vanishes. Keeping only subbands 1 and 2, the condition for intersubband transitions is

$$(\Pi^0_{12} + \Pi^0_{21})U_{12,12} = 1 \tag{5.31}$$

For $q \to 0$, this condition gives the resonance energies in the familiar form of Ando [40] (derived in Section 2.1 and given in Eq. (2.47))

$$\hbar^2\tilde{\omega}^2_{21} = \varepsilon^2_{21} + 2\varepsilon_{21}U_{12,12}(n_1 - n_2), \tag{5.32}$$

where $U_{12,12}$ contains the depolarization shift term and the excitonic vertex-correction term in the case of the CDE, and only the excitonic vertex-correction term in the case of the SDEs. To conclude, we mention that the formalism presented in this section employs the same approximations used in the theory of optical absorption introduced in Section 2.2. The only important difference is that in this section we calculate the response functions of the confined electron gas for nonzero in-plane wavevector of the excitations, whereas the optical absorption theory described in Section 2.2 is valid only in the long-wavelength limit $q = 0$.

CHAPTER 6

Absence of spin-density excitations in coupled double-quantum-wells at high electron densities

6.1 Introduction

In an interesting recent experimental Raman scattering study, Decca *et al.* reported [32] the observation of the suppression of the collective intersubband spin density excitation (SDE) in a coupled double quantum well (DQW) structure in the high electron density (N_s) limit when the two low-lying DQW subbands, the so-called symmetric (S) and antisymmetric (AS) levels with a single-particle energy gap $\Delta_{SAS} < E_F$ (where E_F is the two dimensional Fermi energy) separating them, are both densely occupied. In this section we provide a detailed quantitative calculation of the elementary excitation spectra of the coupled DQW system discussing in particular the recent inelastic light scattering experimental observations [33]. We find excellent agreement between our theoretical results and experimental data for both the charge density excitation (CDE) and the SDE spectra except for the samples with highest N_s where the subband filling parameter $\eta \equiv \Delta_{SAS}/E_F \lesssim 0.25$. Our main interest in this section, following Ref. [32], is to investigate the strong-coupling two-component situation $\eta < 1$ when the S and AS subbands are both occupied by electrons. Around a small critical

value of η (≈ 0.1), the experimental SDE abruptly merges with the single particle excitation (SPE) spectra, whereas our calculated SDE merges with the SPE monotonically as a continuous function of η as η approaches zero without showing any sudden collapse around $\eta \approx 0.1$. Aside from this important qualitative difference associated with the abrupt disappearance of the experimental vertex correction (the energy difference between the SPE and the SDE arises from the excitonic vertex correction) around $\eta \approx 0.1$, our theoretical results agree very well (within 0.5 meV) with the experimental measurements.

6.2 Results

A typical DQW structure used in our calculation is shown in Fig. 6.1, where the electron gas is taken to be confined in the translationally invariant x-y plane and the growth direction is the z-axis. We can see that the energy levels are grouped in doublets, which become degenerate for infinite well separation. By definition, $\Delta_{SAS} = E_2 - E_1$ is the energy difference between the lowest two subbands of the DQW, the symmetric and antisymmetric levels. In this chapter and the next, we concern ourselves with intersubband transitions between these two subbands. Following the experimental work of Decca *et al.* [32] we have used in our calculations several different DQW structures with varying N_S and well parameters so as to have many different values of Δ_{SAS} and the occupancy parameter η ($\equiv \Delta_{SAS}/E_F$).

Our calculation, which was described in detail in Chapter 5, involves three steps. First, we carry out a self-consistent local-density-approximation (LDA) calculation (Section 2.1) of the DQW subband energy levels E_i and wavefunctions $\phi_i(z)$ (a typical example being shown in Fig. 6.1). Then we calculate the

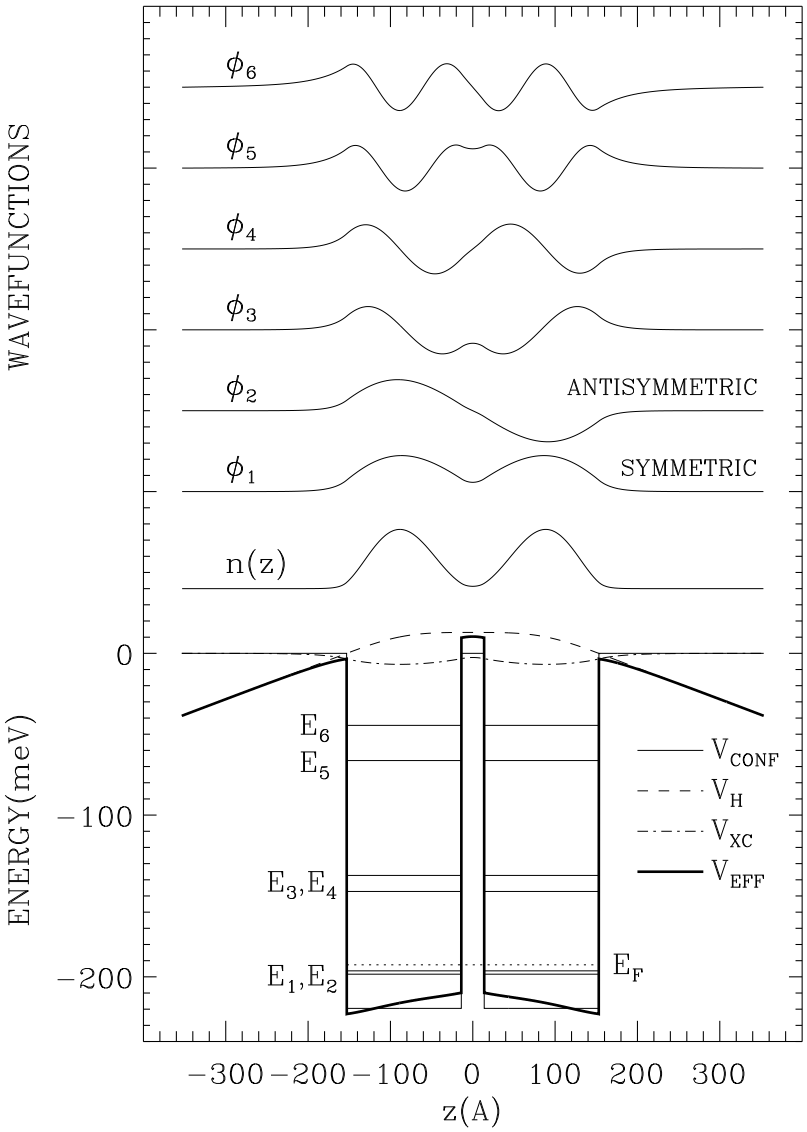

Figure 6.1: A typical double quantum well structure, given by the bare confining potential V_{CONF}, used in the experimental study of Ref. [32], and its self-consistent LDA subband energy levels E_i, eigenfunctions ϕ_i, electron density $n(z)$, Fermi energy E_F, and effective, Hartree, and exchange-correlation potentials V_{EFF}, V_H, and V_{XC}. The areal density is $N_s = 2.68 \times 10^{11}\ cm^{-2}$.

irreducible (Π) and the reducible ($\tilde{\Pi}$) polarizability functions of the electron layer confined in the DQW structure using the self-consistent LDA subband energies and wavefunctions in a linear response theory (Chapter 5). The irreducible and the reducible response functions are formally connected by the matrix relation $\tilde{\Pi} = \Pi\varepsilon^{-1}$ where $\varepsilon = 1 - V\Pi$ is the tensor representing the subband dielectric function with V as the direct Coulomb interaction. The irreducible response function Π is connected to the bare LDA polarizability function Π_0 (which is just the two-dimensional Lindhard function using LDA energies and wavefunctions) through the vertex correction $\Pi = \Pi_0(1 + U_{xc}\Pi)^{-1}$ where U_{xc} represents the LDA exchange-correlation induced vertex correction. Thus Π_0, Π, and $\tilde{\Pi}$ are respectively the "bare" polarizability bubble (including, however, renormalized LDA quasiparticle energies), the vertex corrected polarizability, and the screened polarizability. Once Π_0, Π, and $\tilde{\Pi}$ are calculated their respective poles (or, peaks) immediately give us the SPE, the SDE, and the CDE energies. The third step of our calculation involves directly obtaining the Raman scattering spectra for the SDE and the CDE which are given respectively by the spectral strengths $Im\ \Pi$ and $Im\ \tilde{\Pi}$. For the purpose of comparison we also calculate the SPE spectral strength given by $Im\ \Pi_0$, which according to the simple linear response theory, should not be accessible to Raman scattering experiments [32]. Some typical calculated Raman spectra are shown in Fig. 6.2, and are discussed below. The self-consistent linear response integral equations connecting the dynamical polarizability functions $\Pi_0(z, z')$, $\Pi(z, z')$, $\tilde{\Pi}(z, z')$, are solved in the subband representation. In the rest of this section we discuss our numerical results comparing critically with the experimental data [32]. All our calculations assume the effective mass approximation for the GaAs $-$ $Al_xGa_{1-x}As$ $-$ GaAs DQW structures

and we use GaAs conduction band parameters [21] in our LDA calculations. The DQW well parameters and electron gas densities are taken from Ref. [32].

In Fig. 6.2 we show calculated results for the spectral weights of the SDE and SPE modes for several values of the wavevector transfer q for a sample with $N_S = 6.35 \times 10^{11} cm^{-2}$ and $\eta = 0.12$. When confronted with Fig. 2 of Ref. [32], this figure shows that the collapsed SDE and SPE experimental peaks show a wavevector dependent lineshape that agrees better with the theoretical lineshape of the SPE than with that of the SDE. Aside from the results shown in Fig. 6.2, in this section we will only discuss results corresponding to the experimental backscattering geometry with very small wavevector transfer in the plane of the electron layer, $q \simeq 0.1 \times 10^4 cm^{-1}$, as used in the experimental set-up [32]. (All the elementary excitation energies presented in this section correspond essentially to the long wavelength, i.e. $q \approx 0$, limit for the mode wavevector in the x-y plane because this is the situation reported in the work of Ref. [32]). The results of this section correspond to *intersubband* elementary excitations (associated with the quantized z-motion of the electron gas) arising from transitions between the symmetric and the antisymmetric energy levels (i.e. the lowest two energy levels shown in Fig. 6.2) — the elementary excitations associated with transitions to the higher subbands are at considerably higher energies and were not studied in Ref. [32]. Thus, the SPE peak corresponding to the pole in Π_0 always occurs at the energy $E = \Delta_{SAS}$ corresponding to the (LDA-renormalized) symmetric-antisymmetric gap between the lowest two levels. Note that in our calculations of the spectral weight functions ($Im\ \Pi_0$, $Im\ \Pi$, $Im\ \tilde{\Pi}$ corresponding respectively to SPE, SDE, and CDE) we use a small collisional broadening $\Gamma \approx 0.1 meV$ taken from the experimental mobility values.

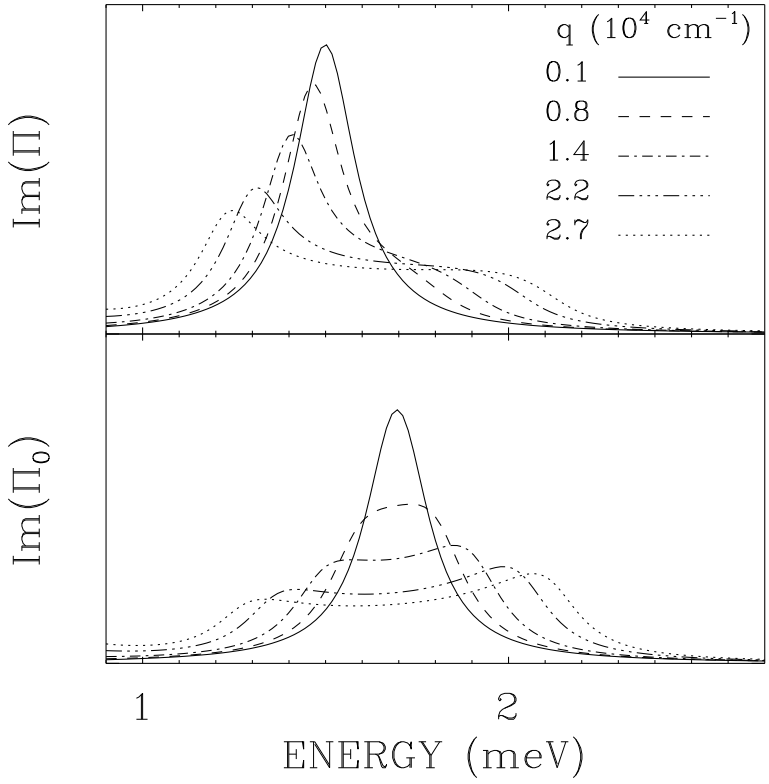

Figure 6.2: Calculated Raman spectra for the spin-density excitation (SDE), and the single particle excitation (SPE), given by $Im\ \Pi$ and $Im\ \Pi_0$, respectively, for several values of the in-plane wavevector transfer q. The DQW sample has well width $d_w = 139$Å, barrier width $d_b = 28$Å, density $N_S = 6.35 \times 10^{11} cm^{-2}$ and subband occupancy parameter $\eta = 0.12$.

It is traditional to write the intersubband elementary excitation energies as [40, 29, 27, 18, 30, 74]

$$E_{CDE}^2 = E_{SDE}^2 + 2E_{SPE}(n_S - n_{AS})\alpha^* \tag{6.1}$$

$$E_{SDE}^2 = E_{SPE}^2 - 2E_{SPE}(n_S - n_{AS})\beta^* \tag{6.2}$$

where $n_{S(AS)}$ are the occupancies of the symmetric (antisymmetric) subbands (i.e. $N_S = n_S + n_{AS}$), $E_{SPE} \equiv \Delta_{SAS}$, and α^*, β^* are parameters (which depend on E_i, $\phi_i(z)$, V, and U_{xc}) which determine the depolarization shift and the vertex correction, respectively. Note that the definitions of the depolarization shift (α^*) and the vertex correction (β^*) shifts as given in Eqs. (1) and (2) above explicitly incorporate the occupancy factor dependence (i.e. the $n_S - n_{AS}$ factor) arising from the Pauli principle, thus eliminating the trivial dependence of both the depolarization shift and the vertex correction on the occupancy difference as both (S and AS) subbands are occupied. Following references [40, 29, 27, 18, 30, 74] one could define $\alpha = (n_S - n_{AS})\alpha^*$ and $\beta = (n_S - n_{AS})\beta^*$, which are more appropriate in the extreme quantum limit ($\eta > 1$) when only the lowest subband is occupied, making $\alpha = N_S\alpha^*$ and $\beta = N_S\beta^*$. When both subbands are occupied ($\eta < 1$) it is appropriate to eliminate the trivial Pauli principle-induced occupancies factor from the definitions of α and β as was done in Ref. [32]. Any dependence of the depolarization shift and the vertex correction parameters α^* and β^* on the subband occupancy factor η (where $\eta < 1$ means both subbands are occupied) necessarily arises from nontrivial screening and exchange-correlation corrections and *not* as a trivial manifestation of the Pauli principle. Following the experimental procedure of Ref. [32], we calculate the α^* and β^* parameters by obtaining E_{SPE} (poles of $Im\ \Pi_0$, i.e. the LDA energy levels), E_{SDE} (poles of

$Im\ \Pi$ including vertex corrections), and E_{CDE} (poles of $Im\ \tilde{\Pi}$) from our time-dependent LDA-linear response calculations. (The occupancies n_S and n_{AS} are known from our LDA calculations.)

In Figs. 6.3 and 6.4 we show a direct comparison between our theoretical calculations and experimental measurements for β^* and α^* as functions of the filling parameter η (Fig. 6.3) and the total electron density N_S (Fig. 6.4) for all seven samples employed by Decca *et al.* [32]. In general, β^* goes down with decrease (increase) in η (N_S) both in experiment and theory, showing very good agreement (better than 0.3 meV in absolute energies of $\Delta_{SAS} - E_{SDE}$) except for one qualitative difference, namely, in theory β^* decreases monotonically with decreasing (increasing) η (N_S) whereas in experiment β^* seems to go abruptly to zero around $\eta \approx 0.1$ (i.e. the vertex correction vanishes around $\eta \approx 0.1$ making the SDE and SPE indistinguishable). Note that even around $\eta \approx 0.1$, the actual energetic difference between our theoretically predicted SDE peak and the experimental "SDE" peak ($\equiv$ "SPE" with $\beta^* = 0$) is typically small ($\sim$ 0.2–0.3 meV). For the depolarization shift (α^*) experiment and theory, in general, agree very well (except again for $\eta \lesssim 0.25$ there is some quantitative difference with the experimental CDE energies being typically 0.5 meV below the theoretical calculations). The important point to note about the depolarization shift is that α^* is reasonably insensitive to variation in η (or, N_S), changing little over an almost order of magnitude change in electron density, both in experiment and theory.

For obvious reasons (namely, that it is not possible to vary N_S or η in a single DQW sample—each sample comes with its fixed N_S and η values) the experimental results (and the corresponding theoretical results) are for seven

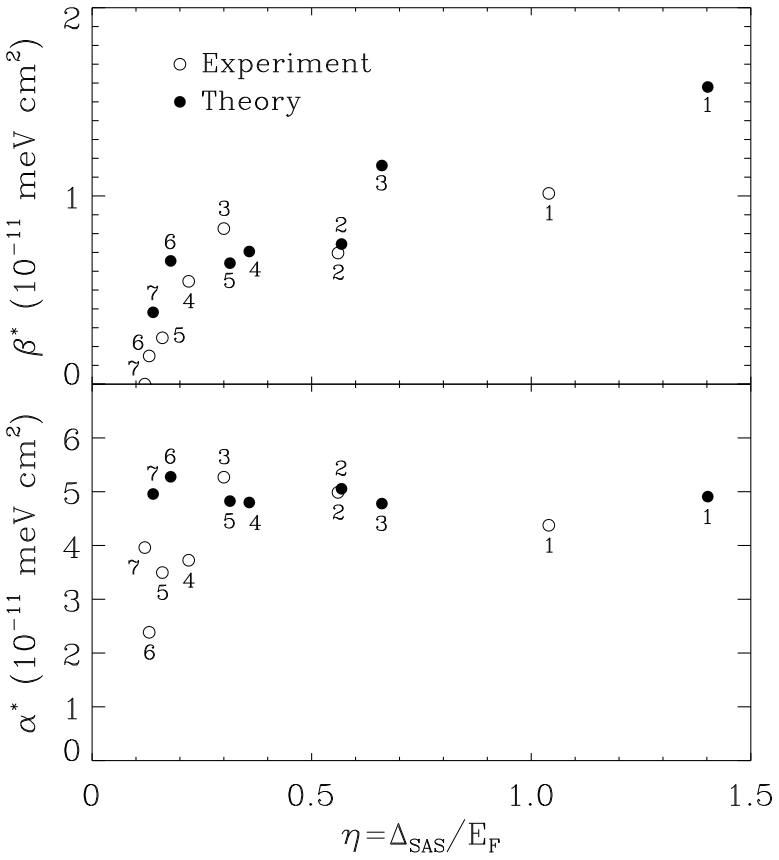

Figure 6.3: Calculated and experimentally measured depolarization shift and excitonic vertex correction parameters α^* and β^* as functions of the filling parameter $\eta \equiv \Delta_{SAS}/E_F$, for the different DQW samples studied in the experiments of Ref. [32].

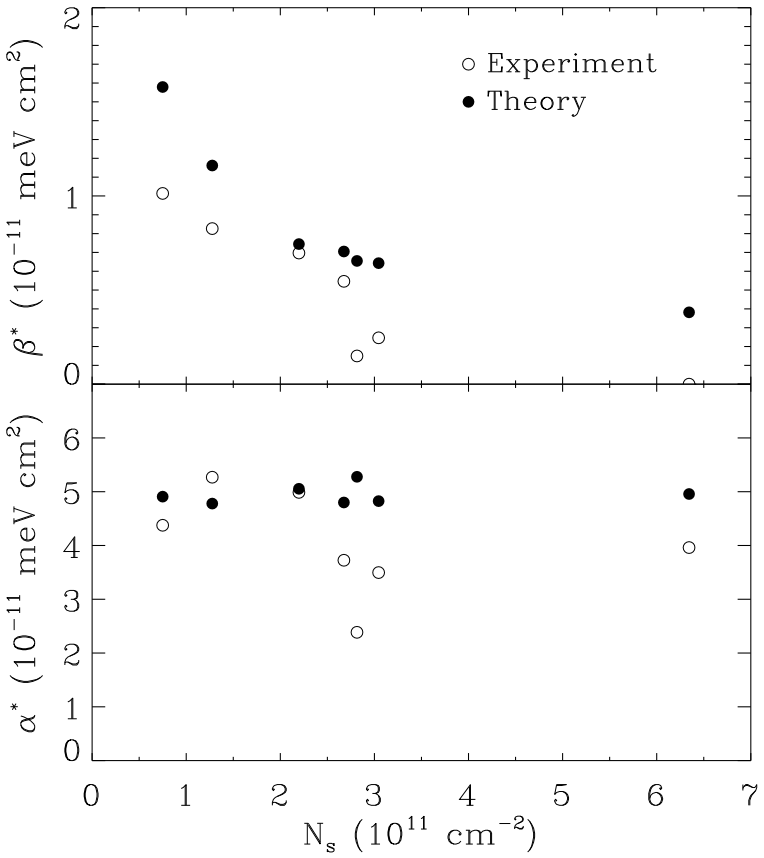

Figure 6.4: Calculated and experimentally measured depolarization shift and excitonic vertex correction parameters α^* and β^* as functions of the total electron density N_S, for the different DQW samples studied in the experiments of Ref. [32].

different DQW samples corresponding to the seven different data points shown in Figs. 6.3 and 6.4. Theoretically, of course, we can vary η continuously in a fixed sample by changing N_S continuously in our calculations. Results of such a calculation for a fixed sample are shown in Fig. 6.5 as continuous functions of N_S (main figures) and η (insets). (For completeness, in Fig. 6.5 we show β^* calculated using both local-charge-density and local-spin-density exchange-correlation potentials [74]. The difference between the two curves is less than the experimental errors for the range of η under consideration.) These results clearly demonstrate (without the necessary numerical scatter of Figs. 6.3 and 6.4 which arise from using different samples) that: (i) The vertex correction β^* decreases monotonically with decreasing (increasing) η (N_S), becoming very small as η approaches zero; (ii) The calculated β^* does not agree well with experiment for $\eta \lesssim 0.25$, and most notably, it does not go abruptly to zero for a finite value of η, as it does in the experiment for $\eta \approx 0.1$; (iii) The depolarization shift α^* is essentially insensitive to η (or N_S) remaining a constant over a broad range of density and occupancy values.

6.3 Summary

In this chapter we calculated the lowest intersubband SDE and CDE energies in a strongly-coupled two-component DQW structure where both the symmetric and the antisymmetric subbands are occupied, finding, in good agreement with a recent experiment [32], that the vertex correction β^* decreases monotonically with decreasing subband occupancy parameter $\eta \equiv \Delta_{SAS}/E_F$ or increasing the electron density N_S whereas the depolarization shift α^* is insensitive to changing η and N_S. In contrast to the experimental finding that $\beta^* \approx 0$ abruptly around $\eta \approx$

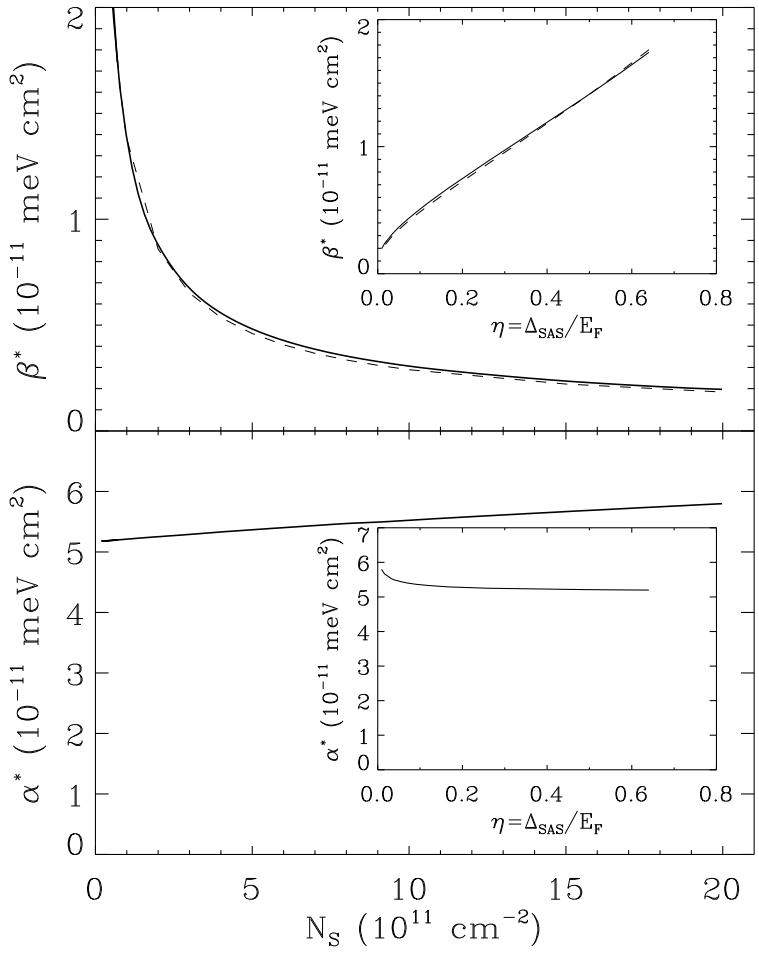

Figure 6.5: Calculated depolarization shift and excitonic vertex correction parameters α^* and β^* as functions of areal density N_S, for a DQW structure of well width 139Å and barrier width 40Å. Insets: α^* and β^* for the same DQW as functions of the filling parameter $\eta \equiv \Delta_S AS/E_F$. The solid and dashed lines give β^* calculated using local-charge-density and local-spin-density exchange-correlation potentials, respectively.

0.1, β^* decreases monotonically in our theory with decreasing (increasing) η (N_S) becoming very small for small η. Thus, while our time-dependent LDA theory correctly describes the broad quantitative features of experiment quite well, the abrupt collapse of the vertex correction must be arising from higher order vertex diagrams (as discussed in Ref. [32]) not included in the ladder vertex corrections [27] of our time-dependent-LDA theory. Our results for β^* can be meaningfully understood as the screening out of the excitonic correction in the high density limit which makes the vertex correction vanish. While the excitonic correction arising from exchange interaction is screened, the direct Coulomb interaction leading to the depolarization shift is obviously unscreened, and, therefore, α^* remains unchanged as N_S increases.

CHAPTER 7

Intersubband spin-density excitonic instability

7.1 Introduction

Two dimensional (2D) electron gas systems confined in semiconductor space charge layers (e.g. Si inversion layers, GaAs heterojunctions, and quantum wells) have provided for the last twenty years an ideal laboratory for studying various electron-electron interaction induced many body exchange-correlation effects under almost textbook conditions (albeit in two dimensions) of an effective mass approximation jellium background. This is particularly true in the ultrapure modulation-doped $GaAs - Al_xGa_{1-x}As$ structures where effects of impurity scattering are substantially reduced by spatially separating the 2D electrons from the dopant ions which produce them. In the presence of a strong external magnetic field which quenches the electronic kinetic energy, a 2D electron gas shows [75, 76, 77, 78, 79, 80, 81, 82] a variety of strongly correlated quantum phases (eg. the fractional quantum Hall liquid). When additional degrees of freedom associated with spin, layer or subband index are introduced, the 2D electron gas in the presence of a strong external magnetic field is known to have an extremely rich quantum phase diagram [79]. This phase diagram consists of many different compressible and incompressible phases, and quantum phase transitions between some of them have been experimentally observed [80, 81]. In contrast to this

strong-field situation, where the 2D electron system is generally considered to be a strongly correlated many-body quantum liquid, the *zero* magnetic field situation has attracted relatively little attention from a many-body strong correlation physics viewpoint. In this chapter we show that at low but experimentally accessible electron density ($\sim 0.7 \times 10^{11}\ cm^{-2}$) there is a novel exchange-correlation driven *zero-field* electronic phase transition in a double quantum well (DQW) system where the *intersubband* spin density excitation (SDE) gap vanishes because the excitonic vertex correction becomes larger than the single-particle symmetric-antisymmetric energy gap (Δ_{SAS}) in the system, giving rise to the collapse of the normal "metallic" Fermi liquid phase of the system as it becomes unstable to the spontaneous formation of zero-energy SDEs, or, equivalently, many-body triplet exciton pairs [34]. We emphasize that this electronic phase transition to a spin density-triplet excitonic phase occurs spontaneously at zero magnetic fields as the electron density (N_S) of the DQW system is lowered to a critical density (N_C) with the SDE energy vanishing at $N_S = N_C$ and the excitonic phase being stable for $N_S < N_C$. Our predicted transition should be observable in depolarized inelastic light scattering experiments where the vertex correction-driven suppression of Δ_{SAS} should show up with the SDE energy becoming vanishingly small at $N_S \leq N_C$.

There has been substantial recent experimental and theoretical interest in DQW structures because the extra (two coupled layers instead of a single 2D layer) degree of freedom associated with intersubband transitions between the symmetric and the antisymmetric levels introduces a new energy scale into the problem which competes with the intrasubband (i.e. 2D) kinetic correlation energies [79]. In particular, competition among the symmetric-antisymmetric energy

gap, the intralayer, and the interlayer Coulomb correlation effects leads to interesting quantum phase transitions in the strong magnetic field limit including the disappearance of odd-integer quantized Hall steps and the appearance of even-integer denominator fractional quantized Hall steps. While correlation effects in DQW structures have been extensively studied [79, 80, 81, 82] in the presence of strong external magnetic fields (motivated by the physics of quantum Hall effect), there have been only a few corresponding studies [83, 73, 84] of DQW systems in the zero field limit. These few studies do indicate, however, that the introduction of the second layer into the problem substantially enhances [84] the importance of exchange-correlation many-body effects and, in particular, the elementary excitation spectra of the DQW system could be substantially affected by many-body effects. In a very recent experimental work, Decca *et. al.* [32] showed that the excitonic shift or the vertex correction to the intersubband SDE energy (the excitonic shift is roughly the difference between the intersubband SDE and the intersubband uncorrelated electron-hole single-particle excitation, SPE, energies) vanishes in a DQW system in the *high density limit*, making the SDE and SPE indistinguishable when both the symmetric and the antisymmetric levels are densely populated (See Chapter 6 and Ref. [33]). In this chapter, we show that in a *lower density* regime, on the other hand, the vertex correction induced excitonic shift is greatly enhanced in a DQW structure and, in fact, may exceed the symmetric-antisymmetric single-particle gap Δ_{SAS} at a critical density $N_S \approx 0.7 \times 10^{11}\ cm^{-2}$, leading to an instability of the usual Fermi liquid ground state of the system for electron densities $N_S \leq N_C$. We emphasize that the work reported here is in the experimentally accessible *intermediate* density regime ($N_S \sim 0.7 \times 10^{11}\ cm^{-2}$) in contrast to earlier works in the very low density

regime ($< 10^{10}\ cm^{-2}$) [84] and the high density regime ($\gtrsim 10^{11}\ cm^{-2}$) [32, 33].

7.2 Results

A typical GaAs – $Al_xGa_{1-x}As$ DQW structure considered in this chapter is shown in Fig. 6.1— it is similar to the existing experimental samples [32]. We are only concerned with the lowest intersubband gap, $\Delta_{SAS} =\mid E_2 - E_1 \mid$, where $E_{1,2}$ are the two lowest subband bottom energies as shown in Fig. 6.1, for motion along the z-direction (the x-y plane being the plane of 2D confinement). The lowest intersubband gap is the symmetric (S)-antisymmetric (AS) gap Δ_{SAS}. As we discussed in Chapter 5, there are three different types [66, 27] of possible intersubband excitations in the system: the single particle excitations (SPE) which are just the uncorrelated intersubband electron-hole pair excitations in the S and AS levels, the SDE which are collective spin density excitations, and the collective charge density excitations (CDE). The SDEs correspond to the poles (or peaks) of the full *irreducible* polarizability function of the system whereas the CDEs are given by the full *reducible* polarizability function. Since, by definition, the SPEs are given by the poles of the zeroth order uncorrelated polarizability function without any vertex corrections, the SDEs are shifted below the SPEs by the excitonic vertex corrections. The CDE, which is just the intersubband collective charge density plasma oscillation of the system, is dynamically screened by the direct Coulomb interaction (through the usual series of bubble diagrams which connect the reducible response function to the irreducible one) and is, therefore, shifted above the SDE by the depolarization shift. The SDE is unaffected by the depolarization shift because the Coulomb interaction, being spin conserving, does not screen the spin-density fluctuations. We refer to the SDE collective

mode as a triplet exciton (correspondingly, the CDE is a singlet exciton) with the understanding that we are talking about an *intersubband* exciton rather than the usual interband exciton — the word "exciton" signifies that the vertex correction or the final state interaction between the intersubband electron-hole pair is included in our calculation. We calculate the renormalized energies of the SDE, SPE, and the CDE modes for the $S \rightarrow AS$ transitions in DQW structures using the fully self-consistent time-dependent-local density-approximation (TDLDA) (Chapter 5). The results given in this paper are for zero temperature calculations, which suffice to establish the existence of the instability. Similar calculations [27, 74, 30] have been extremely successful in describing quantitatively the collective intersubband excitations in single quantum wells, heterojunctions, and inversion layers. Our SDE calculation uses the spin-polarized LDA potential whereas the SPE and the CDE calculations employs the usual spin unpolarized LDA functional [46, 74].

In Fig. 7.1 we show our calculated long wavelength SAS intersubband collective mode energies as a function of N_S. There are three striking features in this figure: (1) E_{SDE} goes to zero at a critical density $N_C \approx 0.7 \times 10^{11}\ cm^{-2}$; (2) there is a re-entrant behavior with E_{SDE} becoming finite again at a lower critical density of about $0.1 \times 10^{11}\ cm^{-2}$; (3) E_{CDE} becomes less than $\Delta_{SAS} \equiv E_{SPE}$ around $N_S \approx 0.2 \times 10^{11}\ cm^{-2}$. The third prediction, originally made on Ref. [27] and recently verified experimentally [31] in a single quantum well structure, will not be further discussed here.

We concentrate in this chapter on the vanishing energy of the SDE mode around $N_C \approx 0.7 \times 10^{11}\ cm^{-2}$. The normal system with a "metallic" Fermi surface is clearly unstable at N_C (or, below) because it can spontaneously create

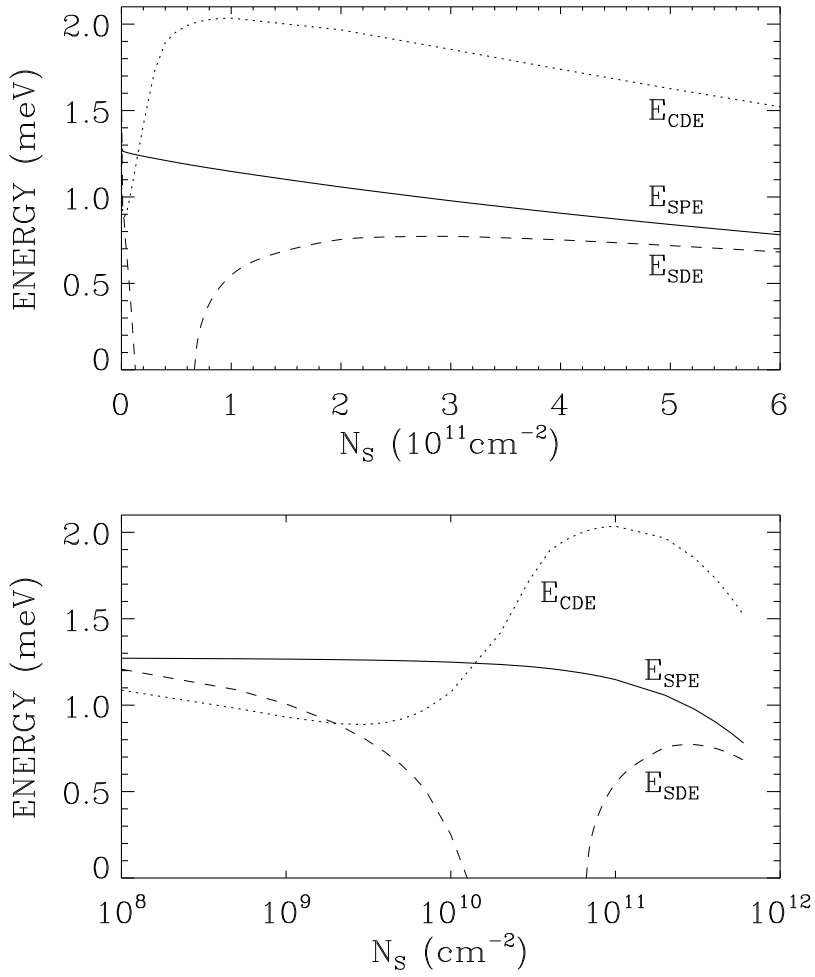

Figure 7.1: The calculated intersubband charge density excitation E_{CDE}, spin density excitation E_{SDE}, and the single particle excitation $E_{SPE} \equiv \Delta_{SAS}$ energies as a function of 2D electron density N_S for a DQW structure with barrier width $d_B = 40$Å and well width $d_W = 139$Å. The critical density for the instability $N_C \approx 0.69 \times 10^{11}\ cm^{-2}$. The bottom figure shows an expanded density range making obvious the re-entrant behavior of the instability.

spin-reversed intersubband electron-hole pairs (i.e. triplet excitons) at no cost of energy. We, therefore, surmise that at N_C there is a phase transition from the normal 2D electron liquid to a triplet intersubband exciton liquid with a re-entrance of the normal phase at a still lower density. The electronic phase transition at N_C is driven purely by exchange-correlation effects which make the vertex correction or the excitonic shift to be larger than the Δ_{SAS} gap, causing the collapse of the SAS gap. The re-entrance at a still lower density can be easily understood as a manifestation of the fact that the vertex correction must vanish as $N_S \to 0$, and, therefore, the normal Fermi liquid phase again becomes stable at some lower densities. (There can be transitions [84, 85] to Wigner crystal phases which occur at much lower N_S values than those considered in this chapter.)

By carrying out our calculation for many different DQW samples with different densities and barrier widths we can obtain an approximate phase diagram for the DQW system which is shown in Fig. 7.2. (As an inset of Fig. 7.2, we show the phase diagram in standard dimensionless units.) For very small barrier widths, the Δ_{SAS} gap is large and the excitonic vertex correction can never overcome it (even at very low densities), making the normal phase the only stable phase. At larger values of the barrier width we see the re-entrant behavior whereas for very large barrier widths Δ_{SAS} is exponentially small, and the low density normal phase is pushed down to unphysically low N_S values. Of course, for such exponentially small Δ_{SAS} (for large barrier widths), the critical temperature for our predicted instability is exponentially low, making the phase transition physically unobservable [86]. In Fig. 7.3 we show the calculated behavior of the Raman scattering spectra in the cross-polarization geometry [32, 66, 74, 30] (which directly probes the SDE mode), approaching the spin density excitonic instability

from above ($N_S > N_C$). As N_S approaches N_C, the spectral peak shifts towards zero energy and the line narrows. We mention that for $N_S < N_C$, the theoretical mean-field SDE energy is imaginary and there is no SDE mode until the re-entrant point is reached. We suggest experiments to be carried out to directly probe the behavior shown in Fig. 7.3.

As additional evidence supporting the predicted transition we show as an inset of Fig. 7.3 the usual mean-field vertex correction $\mid U_{xc}\chi^0_{12} \mid$ where U_{xc} is the (spin-polarized) exchange-correlation induced vertex correction and χ^0_{12} is the intersubband SAS polarizability without the vertex correction (corresponding to SPE peaks), as a function of 2D electron density. The vertex-corrected response function, $\chi^0_{12}[1 - U_{xc}\chi^0_{12}]^{-1}$, clearly has an instability in a finite range of density where the ordinate exceeds unity. Remembering that the usual mean-field criterion (the "Stoner" criterion) for an electronic phase transition is $\mid U_{xc}\chi^0_{12} \mid \geq 1$, we conclude that, at least within the mean-field theory, there is an electronic phase transition to a triplet excitonic phase in the intermediate density range where $\mid U_{xc}\chi^0_{12} \mid$ exceeds one.

The last aspect of the intersubband spin-density-excitation in coupled DQWs that we will analyze is their dispersion relation, or dependence with in-plane momentum transfer. Employing the formalism described in Chapter 5 we calculated such dispersion relation, which is shown in Fig. 7.4 for several sheet densities N_s. The most important feature is that the SDE mode becomes soft at a finite value of the in-plane momentum transfer, q_c, at a critical density somewhat higher than the critical density found at zero in-plane momentum transfer. This indicates that the excitonic instability occurs first at a finite value of in-plane q, and this fact should be taken into account in a future study of the new electronic phase.

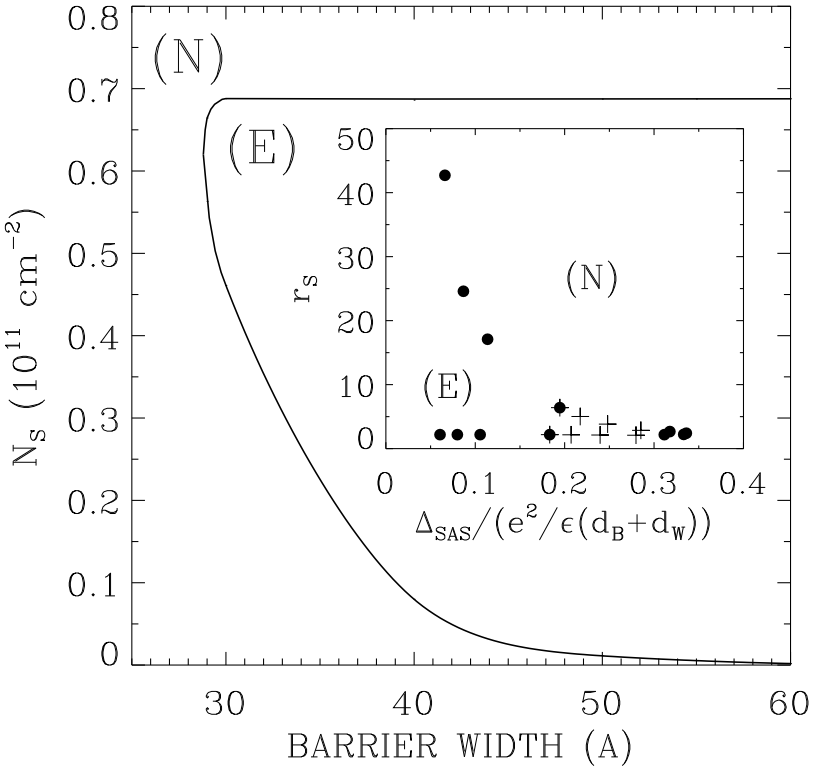

Figure 7.2: The calculated zero temperature quantum phase diagram for $d_W = 139$Å. The normal (N) and the triplet excitonic (E) phases are shown. Inset: phase diagram in terms of the two-dimensional r_s parameter and the "dimensionless" Δ_{SAS} where d_B (d_W) are barrier (well) widths. Solid circles correspond to $d_W = 139$Å and various d_B, and crosses to $d_B = 40$Å and various d_W.

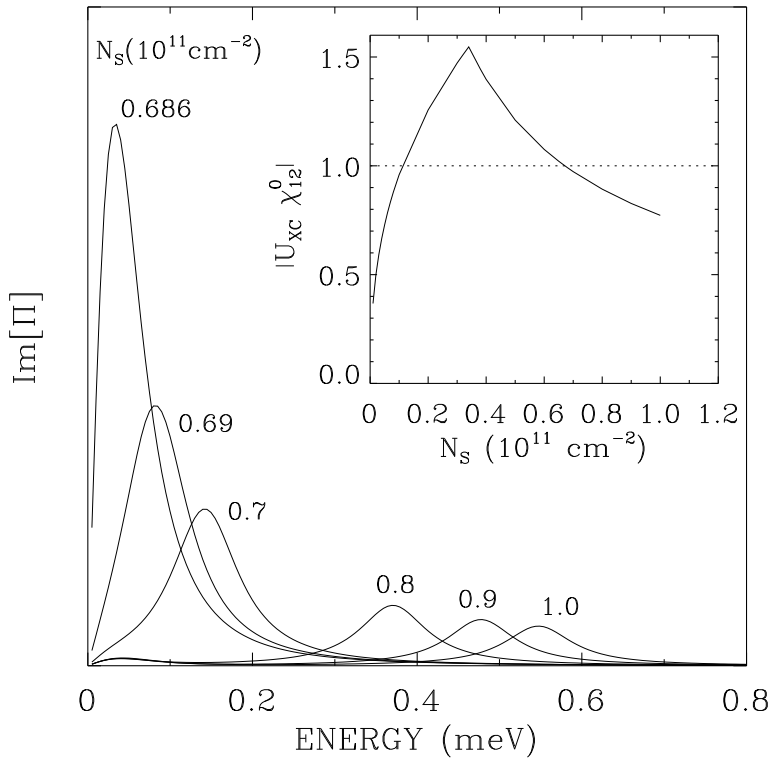

Figure 7.3: Calculated SDE Raman scattering spectra in the cross-polarization geometry showing the approach to the instability from above ($d_W = 139$Å, $d_B = 40$Å). Inset: mean-field vertex correction versus areal density; the electron gas is unstable (the "Stoner" criterion) in the range of density where $\mid U_{xc}\chi^0_{12} \mid \geq 1$.

For example, the new ground state could be characterized by a spin-density wave where the critical q_c sets a characteristic length in the problem. The approach to the critical momentum transfer q_c at a given density could be observed in inelastic light-scattering experiments, by varying the angle of incidence of the light. In Fig. 7.5 we present the calculated Raman spectra at $N_S = 0.7 \times 10^{11} cm^{-2}$, for various values of q. Such experiments would constitute additional evidence of the strong possibility of an electronic phase transition in coupled DQW systems.

Finally, we mention that the instability discussed here for DQWs can also happen in wide *single* quantum wells, where the effective potential develops a barrier in the center at moderate densities becoming analogous to a DQW [79]. This phenomenon can be seen in Fig. 7.6; notice that the electron density profile is similar to the one characteristic of the DQW system (Fig. 6.1). In this effective double well system the separation between the two lowest lying subbands is small ($\sim 0.2meV$) as in the coupled DQWs, and the possibility of an excitonic suppression of the intersubband gap arises. A calculation of the SDE energies shows that this is indeed the case, as can be seen in Fig. 7.7. For the wide square well considered, whose width is $d_W = 1000$Å, the region of imaginary SDE energy is somewhat smaller than for our DQW of barrier width $d_B = 40$Å, but it is in the same density region $\sim 0.4 \times 10^{11}\, cm^{-2}$. Hence, inelastic-light-scattering experiments should be able to observe the approach to the instability in wide square wells also.

7.3 Summary and final remarks

We have calculated spin-density and charge-density excitations in coupled double-quantum-well systems within the TDLDA at densities below $10^{11}\, cm^{-2}$,

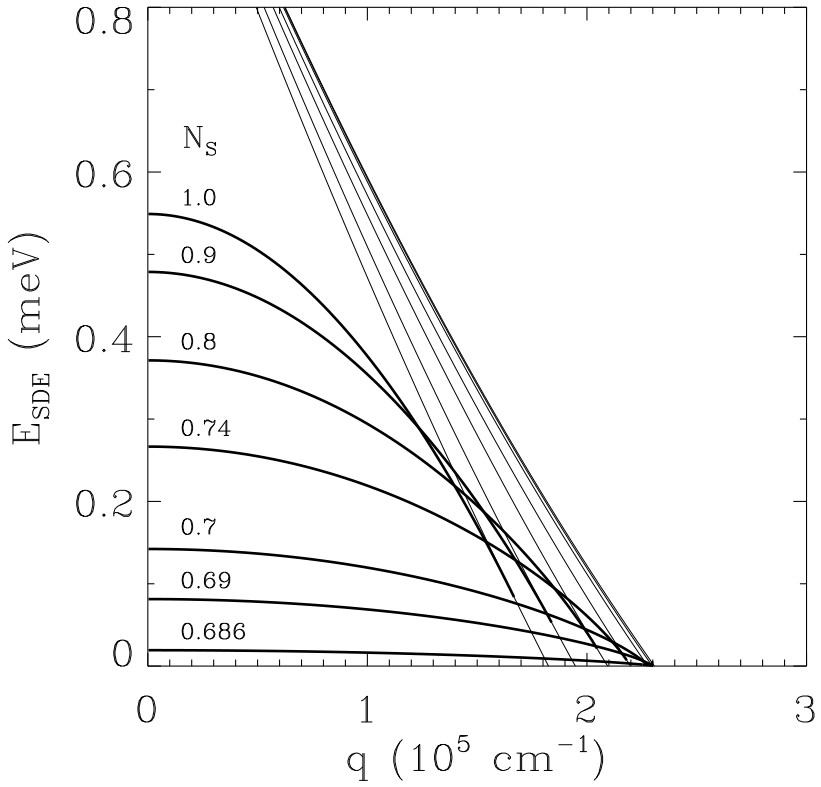

Figure 7.4: Dispersion relation of the intersubband spin-density excitations for a coupled double-quantum-well system, with $d_W = 139$Å and $d_B = 40$Å, for decreasing densities approaching the critical density $N_C \simeq 0.686 \times 10^{11}\, cm^{-2}$ (thick lines) (The densities N_S are given in units of $10^{11}\, cm^{-2}$.) The thin lines give the lower boundary of the particle-hole continuum, above which the collective excitations are Landau damped.

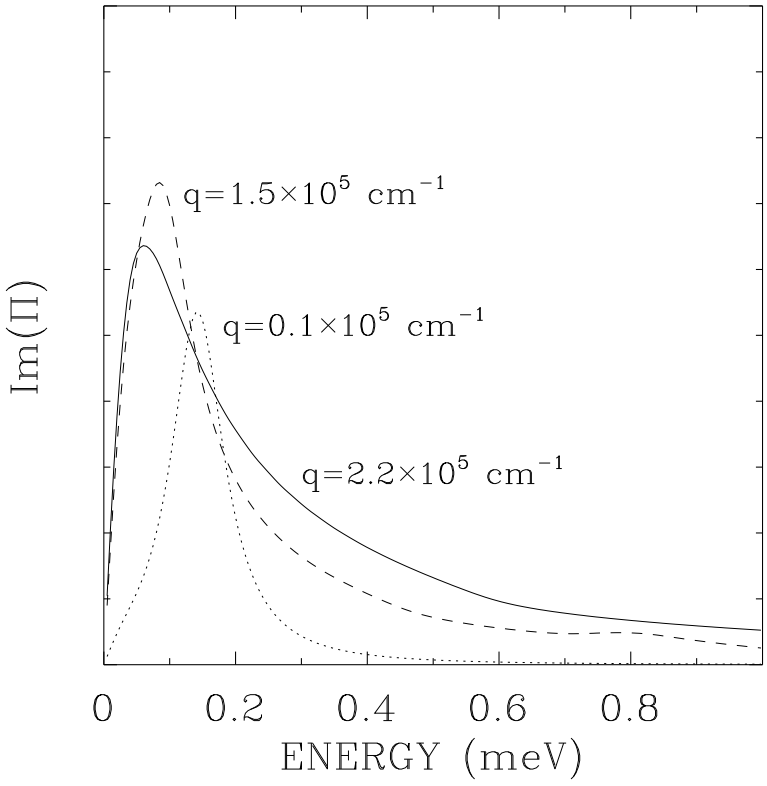

Figure 7.5: Calculated SDE Raman scattering spectra in the cross-polarization geometry showing the approach to the instability at constant density $N_S = 0.7 \times 10^{11} cm^{-2}$ and increasing the wavevector transfer q ($d_W = 139$Å, $d_B = 40$Å).

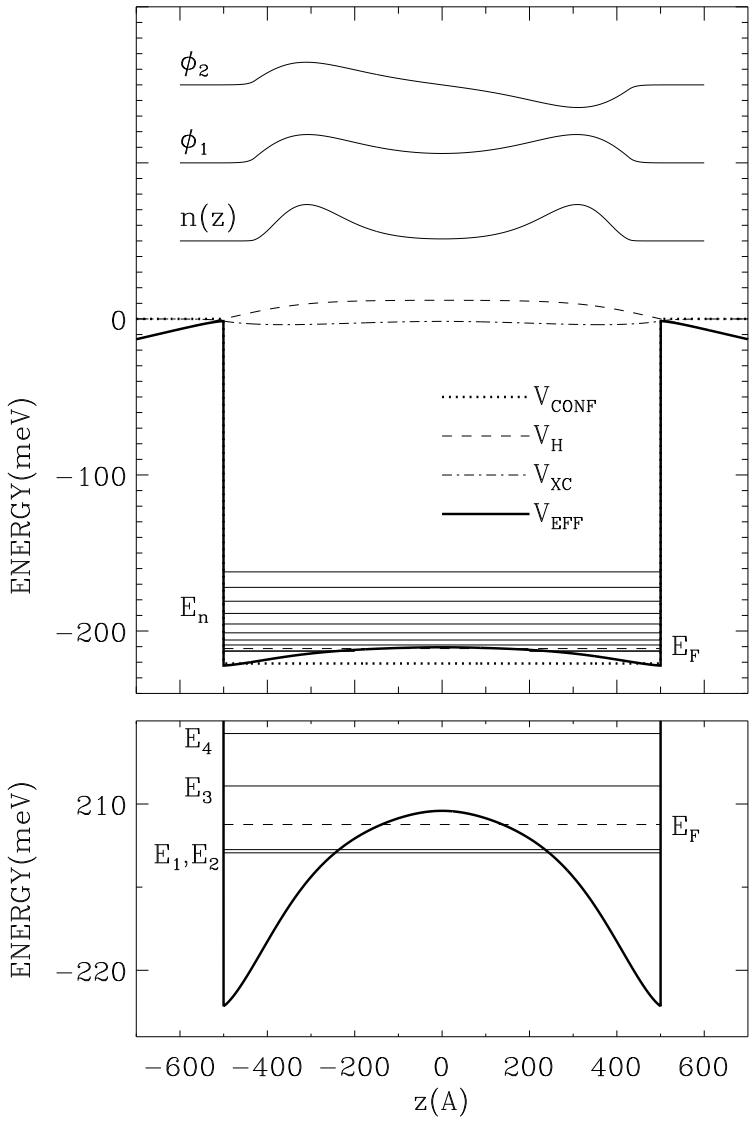

Figure 7.6: A typical wide square quantum well structure, given by the bare confining potential V_{CONF}, and its self-consistent LDA subband-energy-levels E_n, eigenfunctions ϕ_n, electron density $n(z)$, Fermi energy E_F, and effective, Hartree, and exchange-correlation potentials V_{EFF}, V_H, and V_{XC}. The areal density is $N_s = 0.9\times10^{11}\,cm^{-2}$. The figure shows how the electronic density profile becomes localized on the sides of the well and similar to the profile in a double quantum-well system. Bottom: energies in expanded scale.

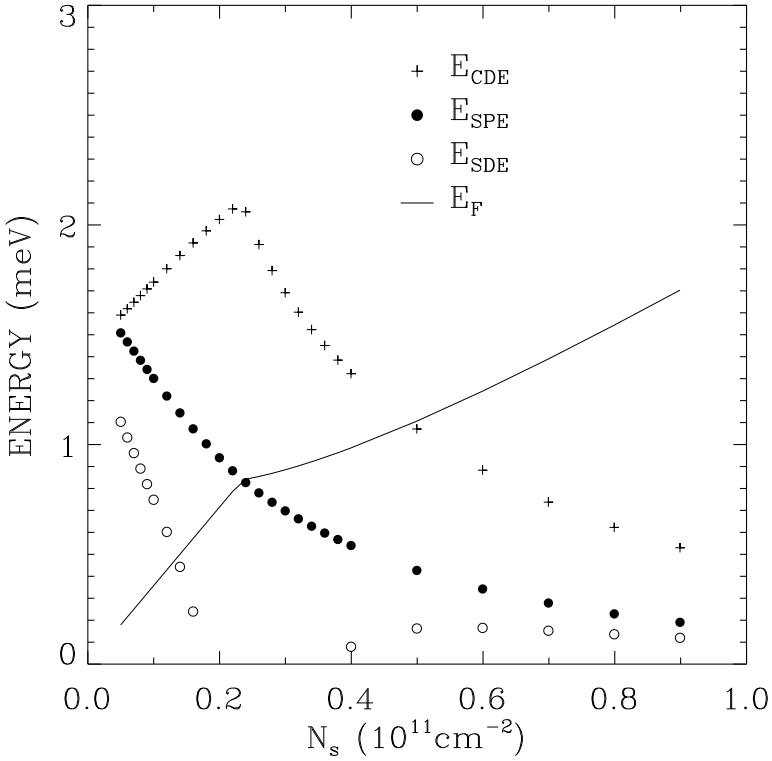

Figure 7.7: The calculated intersubband charge density excitation E_{CDE}, spin density excitation E_{SDE}, and the single particle excitation $E_{SPE} \equiv \Delta_{SAS}$ energies as a function of 2D electron density N_S for a wide square-well structure with well width $d_W = 1000$Å.

and found that the lowest intersubband SDE energy vanishes within a window of areal densities. Thus, our mean-field approach indicates that the normal Fermi liquid ground state of a DQW system is unstable towards the formation of a triplet (spin density) exciton liquid at a critical density of $0.7 \times 10^{11}\ cm^{-2}$, which at still lower density ($\sim 0.1 \times 10^{11}\ cm^{-2}$) may have a re-entrance back into the normal phase. Raman scattering experiments should be able to detect this predicted electronic phase transition by observing the vanishing of the SDE energy as N_S approaches N_C from above. The transition may also manifest itself in intersubband transport properties as a metal-insulator transition (with the excitonic phase expected to be an insulator), but a detailed investigation of the properties of the excitonic phase is left for the future.

The quantitative validity of our spin-polarized TDLDA-based mean-field calculation is difficult to assess because of inherent difficulties associated with estimating the validity of density functional calculations. The two-dimensional r_s–parameter (cf. Fig. 7.2 inset) at the predicted transition is in the range of 2-6 where our choice of exchange-correlation potential should be very good [27, 74]. In general, TDLDA calculations give very good quantitative agreement with experiment for quantum well CDEs and SDEs [33, 74, 30, 48]. Similar mean-field "Stoner" criteria calculations in other contexts have been extremely successful [87] in predicting magnetic transitions in Fe, Co, and Ni, etc. Based on all of this we believe that our calculated phase diagram should be at least qualitatively valid, even though the exact density values for the transition may be 10-20% off. Inclusion of higher order vertex corrections beyond TDLDA is a formidable task which has not been attempted in a consistent manner in any problem.

CHAPTER 8

Ferromagnetic instability in the quasi-two dimensional electron gas

8.1 Introduction

The phases of an electron gas have attracted a great deal of attention since Wigner [88] suggested the possibility that the electron gas would crystallize at sufficiently low density and temperature in order to minimize its potential energy. On the other hand, at high density the kinetic energy dominates and the electron gas becomes and ideal Fermi gas in order to minimize its kinetic energy. At intermediate densities, Bloch [89] suggested that a polarized state with all the spins aligned would have lower energy than the normal fluid. Other possible ground-states, such as spin-density waves have also been proposed [90]. In Chapter 7 we found that the electron gas confined in a coupled double-quantum-well structure has an instability, as indicated by the vanishing of the energy of the intersubband spin-density excitations. Our main goal in this chapter is to establish whether this instability corresponds to a phase transition from the normal spin-unpolarized (or paramagnetic) ground state to a spin-polarized (ferromagnetic) one. To this end, we perform a calculation of the electronic ground-state in a coupled double-quantum well employing the so-called local-spin-density (LSD) approximation. This is a generalization of the local-density approximation (LDA) and was first formally justified by von Barth and Hedin [91] and Pant and Rajagopal [92], and

is suitable to study systems in the presence of an external magnetic field [42], as well as spontaneous magnetization in the absence of a magnetic field. As we will see later in this chapter, our LSD-based study of a coupled DQW system shows that it is not possible to identify the excitonic instability with a ferromagnetic transition, since their critical densities differ by at least an order of magnitude.

Our second goal in this chapter is to employ the LSD formalism to study the ferromagnetic phase transition in single square quantum wells. In particular, we are interested in the dependence of the critical density on the well width, as it would reveal a new aspect (complementary to that explored in Chapter 3) of the crossover from two- to three-dimensional behavior of the electron gas. We will find that as the electron gas is widened the transition density decreases (the ferromagnetic phase becomes less favorable) which agrees with the fact that the influence of the Coulomb interaction is stronger for lower dimensionality. A similar problem to the spin polarization of the ground-state in quantum wells is the problem of "valley condensation" in Si-SiO_2 systems, where instead of spin variables, the electrons can occupy different valleys of the Brillouin zone, and which was studied in the past [93] with similar techniques to the ones employed here.

In the following we summarize the theoretical and numerical evidence that the uniform electron gas in two and three dimensions embedded in a uniform positive background (jellium model) undergoes a ferromagnetic transition below a certain critical density.

Let us consider a uniform polarized electron gas in which $N_\pm$ denotes the number of electrons with spin up (+) and down (-). The ground-state energy can be calculated exactly in the Hartree-Fock approximation, that is, to first order in

the Coulomb interaction, as a function of $N = N_+ + N_-$ and the magnetization $m = (N_+ - N_-)/N$ [25]. The result is

$$\begin{aligned} E_{HF}^{3D} &= E^{(0)} + E^{(1)} \\ &= \sum_{\mathbf{k}\lambda} \frac{\hbar^2 k^2}{2m} \langle \Psi_0 | a_{\mathbf{k}\lambda}^\dagger a_{\mathbf{k}\lambda} | \Psi_0 \rangle \\ &\quad + \frac{e^2}{2V} {\sum_{\mathbf{kpq}}}' \sum_{\lambda_1 \lambda_2} \frac{4\pi}{q^2} \langle \Psi_0 | a_{\mathbf{k}+\mathbf{q}\,\lambda_1}^\dagger a_{\mathbf{p}-\mathbf{q}\,\lambda_2}^\dagger a_{\mathbf{p}\lambda_2} a_{\mathbf{k}\lambda_1} | \Psi_0 \rangle \\ &= \frac{Ne^2}{2a_0} \frac{3}{10} \left(\frac{9\pi}{2}\right)^{2/3} \frac{1}{r_s^2} \left[\left(\frac{1+m}{2}\right)^{5/3} + \left(\frac{1-m}{2}\right)^{5/3} \right] \\ &\quad - \frac{Ne^2}{2a_0} \frac{3}{4\pi} \left(\frac{9\pi}{2}\right)^{2/3} \frac{1}{r_s} \left[\left(\frac{1+m}{2}\right)^{4/3} + \left(\frac{1-m}{2}\right)^{4/3} \right], \end{aligned} \tag{8.1}$$

where $|\Psi_0\rangle$ is the noninteracting many-body ground-state, $a_0 = \hbar^2/me^2$ is the Bohr radius, and $r_s = (3V/4\pi N)^{1/3}/a_0$. $E^{(0)}$ is the kinetic energy term. Notice that in $E^{(1)}$, one has two possible nonvanishing terms

$$\begin{aligned} \langle \Psi_0 | a_{\mathbf{k}+\mathbf{q}\,\lambda_1}^\dagger a_{\mathbf{p}-\mathbf{q}\,\lambda_2}^\dagger a_{\mathbf{p}\lambda_2} a_{\mathbf{k}\lambda_1} | \Psi_0 \rangle &= \langle \Psi_0 | a_{\mathbf{k}\lambda_1}^\dagger a_{\mathbf{p}\lambda_2}^\dagger a_{\mathbf{p}\lambda_2} a_{\mathbf{k}\lambda_1} | \Psi_0 \rangle \\ &\quad + \langle \Psi_0 | a_{\mathbf{p}\lambda_1}^\dagger a_{\mathbf{k}\lambda_2}^\dagger a_{\mathbf{p}\lambda_2} a_{\mathbf{k}\lambda_1} | \Psi_0 \rangle. \end{aligned} \tag{8.2}$$

The first term gives the *direct* Coulomb energy, which, since it corresponds to $q = 0$, is not included in the summation—it has been already included in the total energy and canceled out by the background-background and electron-background interactions. Thus, to first order, we are left only with the *kinetic* and *exchange* energies. Now we can compare the energies of the ferromagnetic state (m=1) and the unpolarized state (m=0) to first order in the interaction, and we find that the polarized state has the lowest energy if $r_s > 5.45$. This means that although the polarized state clearly has larger kinetic energy, the decrease in the exchange energy associated with aligning all the spins offsets the kinetic energy

gain as long as the density is low enough. An analogous Hartree-Fock analysis of a two-dimensional electron gas gives the following ground-state energy:

$$\begin{aligned} E_{HF}^{2D} &= E^{(0)} + E^{(1)} \\ &= \sum_{\mathbf{k}\lambda} \frac{\hbar^2 k^2}{2m} \langle \Psi_0 | a_{\mathbf{k}\lambda}^\dagger a_{\mathbf{k}\lambda} | \Psi_0 \rangle \\ &\quad + \frac{e^2}{2A} \sum_{\mathbf{kpq}}{}' \sum_{\lambda_1 \lambda_2} \frac{2\pi}{q} \langle \Psi_0 | a_{\mathbf{k}+\mathbf{q}\,\lambda_1}^\dagger a_{\mathbf{p}-\mathbf{q}\,\lambda_2}^\dagger a_{\mathbf{p}\lambda_2} a_{\mathbf{k}\lambda_1} | \Psi_0 \rangle \\ &= \frac{Ne^2}{a_0} \left\{ \frac{1+m^2}{r_s^2} - \frac{4\sqrt{2}}{3\pi r_s} \left[(1+m)^{3/2} + (1-m)^{3/2} \right] \right\}. \end{aligned} \tag{8.3}$$

In this case, the condition for a polarized ground-state, $E_{HF}^{2D}(r_s, m = 1) < E_{HF}^{2D}(r_s, m = 0)$, is satisfied if $r_s > 2.84$. This shows that, within the Hartree-Fock approximation, a polarized state is more favorable in two than in three dimensions.

The correlation energy of the electron gas (the contributions to the ground state energy beyond the exchange energy) can only be calculated approximately, and therefore the critical ferromagnetic density cannot be found exactly. Ceperley [46] calculated the ground-state energy of an electron gas in two and three dimensions employing a variational Monte Carlo (VMC) technique. He found that both in two and three dimensions there is an intermediate density regime where a fully polarized state has the lowest energy compared to the unpolarized quantum liquid and the Wigner crystal. In 3D, the polarized phase is stable for $26 < r_s < 67$, and, in 2D, for $13 < r_s < 33$. (Additional unpublished results [94] seem to indicate that there is a transition to a partially polarized liquid at $r_s \approx 20$ and to a fully polarized phase at $r_s \approx 50$). Eleven years later, Tanatar and Ceperley [85] recalculated the ground-state properties of the electron gas in two dimensions employing the VMC technique and the more accurate fixed-node Green's-function Monte Carlo (GFMC) technique. The VMC technique

predicted again a transition from the unpolarized to the polarized liquid at r_s between 10 and 20, consistent with Ceperley's results. The more accurate GFMC technique predicted a transition from the unpolarized liquid to the Wigner crystal at $r_s = 37$, without an intermediate polarized phase. However, the authors point out that near the transition density the polarized phase has an energy very close to the energy of the other phases, and due to finite size effects and errors associated with their approximation method, their conclusion should not be taken as definite. This leaves open the possibility of a stable, fully-polarized phase in the two-dimensional electron gas.

8.2 Local-spin-density theory

In this section we introduce the local-spin-density (LSD) formalism to calculate the ground-state electronic structure of semiconductor quantum wells. The LSD formalism is a generalization of the LDA scheme introduced in Section 2.1, which allows different populations of the two possible spin orientations, or, in other words, a finite spin polarization. The method is also based on the self-consistent solution of the Schrodinger-like Kohn-Sham equation, coupled with the Poisson equation, and the local exchange-correlation potential. The main technical difference between LSD and LDA is that in LSD the effective exchange-correlation potential depends on the local spin polarization as well as in the electron density. Therefore, one has to solve two Kohn-Sham equations, which contain spin dependent effective potentials, for the two components of the spinor wavefunction. Recently, the LSD has been employed to study spin effects in wide parabolic quantum wells in the presence of a perpendicular magnetic field [95].

After factorizing the complete single-electron wavefunction as was done in Eq.

(2.3), we write down the z-dependent Kohn-Sham equation:

$$\left(-\frac{\hbar^2}{2m^*}\frac{d^2}{dz^2} + V_C(z) + V_H(z) + V_{XC}^{\sigma}(z)\right)\phi_n^{\sigma}(z) = \varepsilon_n^{\sigma}\phi_n^{\sigma}(z), \tag{8.4}$$

where n is the subband index, which takes the value 1 for the symmetric level (S), and 2 for the antisymmetric level (AS); the symbol σ denotes the spin orientation, which can be up(+) or down(-). Altogether we need to consider a maximum of four components: ϕ_1^+, ϕ_1^-, ϕ_2^+, ϕ_2^-, and the corresponding energies (we are assuming that no more than two subbands are populated). The density associated to each subband and spin orientation is given by

$$n_n^{\sigma}(z) = N_n^{\sigma}\,|\phi_n^{\sigma}(z)|^2, \tag{8.5}$$

where N_n^{σ} is the occupancy of each level, which at zero temperature is given by

$$N_n^{\sigma} = \frac{m^*}{2\pi\hbar^2}\,(\varepsilon_F - \varepsilon_n^{\sigma})\,\Theta(\varepsilon_F - \varepsilon_n^{\sigma}). \tag{8.6}$$

The total electron density is then

$$n(z) = \sum_{n\,\sigma} n_n^{\sigma}(z). \tag{8.7}$$

We define the spin polarization of the electron gas as

$$m(z) \equiv \frac{n_1^+(z) + n_2^+(z) - n_1^-(z) - n_2^-(z)}{n(z)}. \tag{8.8}$$

In the LSD formalism, the exchange-correlation potential depends on both the density $n(z)$ and the spin polarization $m(z)$. In our calculations we use the expression for V_{XC} obtained by Gunnarson and Lundqvist [96], slightly modified by Das Sarma and Vinter [97] (see Appendix A):

$$V_{XC}^{\pm}(n(z), m(z)) = -\left(\frac{2}{\pi}\right)\left(\frac{9\pi}{4}\right)^{1/3}\frac{1}{r_s}\left(\beta(r_s) \pm \frac{1}{3}\,\delta(r_s)\,\frac{m}{1 \pm 0.3m}\right), \tag{8.9}$$

where

$$\beta(r_s) = 1 + 0.0862\, r_s\, ln\left(1 + \frac{15.24}{r_s}\right), \tag{8.10}$$

$$\delta(r_s) = 1 - 0.0125\, r_s - \frac{0.404\, r_s}{1 + 0.59\, r_s}, \tag{8.11}$$

and r_s is the dimensionless interparticle distance, $r_s = r_0/a^*$, where a^* is the effective Bohr radius. In a quasi-2D system, two possible definitions of r_0 may be relevant. A 2D r_0 can be defined as $r_0 = (\pi N_S)^{-1/2}$, and, for a 3D definition, we need to introduce a characteristic bulk density n_0. Choosing $n_0 \equiv N_S/d_W$, where d_W is the width of the quantum well, we can use the usual definition $r_0 \equiv (3/4\pi n_0)^{1/3}$. The Hartree potential $V_H(z)$ is calculated as in the unpolarized formalism described in Section 2.1. It satisfies Poisson equation, Eq. (2.6), and is given by Eq. (2.7). Finally, the Fermi level E_F is implicitly determined by the condition

$$E_F = \int_{-\infty}^{\infty} dz\, n(z) = \sum_{n\,\sigma} N_n^\sigma. \tag{8.12}$$

The self-consistent solution proceeds exactly like for the LDA case, with the difference that now, in each iteration, one has to solve two Kohn-Sham equations, Eq. (8.4), for the two spinor components of the wavefunctions, ϕ_n^σ. This concludes the self-consistent calculation of the electronic structure in the LSD approximation. In the next section we apply this formalism to coupled double-quantum-wells, and to single square quantum wells.

8.3 Results

The first goal of our study of spin-polarized systems within the local-spin-density (LSD) formalism was to determine whether the excitonic instability studied in Chapter 7 could be explained in terms of a ferromagnetic transition, that

is, a transition from the usual spin-unpolarized ground state to a partially or fully polarized one. We concentrated on a coupled double-quantum-well system, where each individual square well is 139Å wide, and the well separation is 40Å—this is the main sample studied in Chapter 7. Like in the better-known 3D case, a fully polarized phase is expected at low density, and a normal, unpolarized phase at high density. To determine the spin polarization of the system at a given areal density N_S with the iterative self-consistent LSD method, it should be enough, in principle, to introduce a sligth asymmetry in the initial choice of spin densities. If the correct ground state were unpolarized, the initial asymmetry would rapidly disappear in the iteration process. One the other hand, if a polarized state were expected, the initial small polarization would increase until convergence to the fully polarized is achieved. However, since the solution of the self-consistent set of equations of the LSD-approximation method is affected by numerical inaccuracies, in practice our method is sensitive to the initial conditions (initial guess of spin density profiles). Therefore, we employed the following method to determine the ground-state polarization of the system. For a given density N_S (assuming, for example, that only one subband is occupied), we solved the self-consistent algorithm starting with spin densities given by $n_1^+(z) = \eta\, n_u(z)$, $n_1^-(z) = (1-\eta)\, n_u(z)$, and we took two different values of η, $\eta = 0.55$ and 0.95. Here $n_u(z)$ is the density in the unpolarized calculation, performed within the LDA. With this method we searched the phase diagram of spin polarization as a function of N_S for the coupled DQW defined above. For small N_S in the range 1–4 $\times 10^9\, cm^{-2}$, the calculation converges to a fully polarized state, regardless of the initial choice of spin densities. In the range N_S = 5–7 $\times 10^9\, cm^{-2}$, the solution is polarized for the choice $\eta = 0.95$, and unpolarized for $\eta = 0.55$, and

for $N_S > 7 \times 10^9\, cm^{-2}$ the solution is always unpolarized.

Therefore, our first conclusion is that, within the LSD approximation, *there is a ferromagnetic transition* as a function of the electron density N_S in a coupled DQW system, and for our particular choice of parameters it happens around $N_S = 6 \times 10^9\, cm^{-2}$ at zero temperature. On the other hand, this ferromagnetic transition occurs at a density N_S which is an order of magnitude smaller than the critical density N_C where the excitonic transition of Chapter 7 is predicted. (a calculation with the Ceperley-Alder exchange-correlation potential introduced later would give an even smaller critical density). Moreover, it does not seem to show a re-entrant behavior at lower density like the excitonic transition. Based on these differences, we conclude that *the ferromagnetic transition cannot be identified as the excitonic phase transition* that we studied in Chapter 7.

Next we present our results for single square wells. Here the goal was to determine the ferromagnetic-transition critical density as a function of the well width, and therefore make a first step in the study of the evolution of this transition as a function of the dimensionality of the electron gas. The analytical results for two and three dimensions summarized in Section 8.1 indicate that in two dimensions the exchange energy is more important than in three dimensions, and therefore the critical density is higher than in three dimensions. If this tendency is obeyed in the case of quasi-2D systems as well, we expect that in our calculations the ferromagnetic critical density should decrease as the well width is increased.

Employing the method described above, we searched for the ferromagnetic transition in four single square wells of widths d_W = 139Å, 318Å, 500Å, and 800Å. The resulting phase diagram is presented in Fig. 8.1 in terms of N_S versus well width, and also in terms of the 2D and 3D r_s and well width. As

expected, we see that the critical density decreases with increasing well width. However, the limiting values of r_s for narrow and wide wells cannot be directly compared with the pure two- and three-dimensional Hartree-Fock values for two reasons. The first reason is that the analytical results are obtained in the jellium model, whereas in our quantum well calculations the positive charges of the ionized donors are located far away from the electron gas, which should produce an important change in the direct coulomb energy, and therefore affect the ferromagnetic critical density as well. The second reason to expect differences is that our calculation includes correlation effects which go beyond the exchange interaction, even though they are treated in a local and static approximation.

Several authors have proposed different parametrizations of the exchange-correlation potential, which are based on different calculations of the 3D-electron-gas ground-state energy, and therefore differ somewhat from each other. Thus, we have confirmed the existence of the ferromagnetic transition in single square quantum wells by using the parametrization of the exchange-correlation potential proposed by Ceperley and Alder [46] (see Appendix A) which predicts weaker exchange-correlation effects than the one by Das Sarma and Vinter. In Fig. 8.2 we compare several different self-consistent exchange-correlation potentials for a given sample and a value of N_S such that the ground-state is unpolarized. Since the Das Sarma-Vinter potential is larger in absolute value than the Ceperley-Alder one, we expect that using the latter would shift the ferromagnetic critical density down, or possibly suppress the ferromagnetic phase altogether. We have found that, for the square well of width $d_W = 139$Å, the Ceperley-Alder potential predicts a phase transition as well, although it gives a critical density of $N_S = 2 \times 10^9\, cm^{-2}$, down from the $N_S = 1.2 \times 10^{10}\, cm^{-2}$ value obtained with

the Das Sarma-Vinter expression. Therefore, we can be fairly confident that a ferromagnetic transition is indeed present in the confined electron gas. However, the value of the critical transition density cannot be accurately determined with the LSD technique, especially due to the uncertainty in the exchange-correlation potential; the exchange-correlation potential is obtained from the ground-state energy of a uniform electron gas, which necessarily needs to be calculated within some approximation scheme.

8.4 Summary

In this chapter we introduced the local spin-density (LSD) formalism, which generalizes the LDA by allowing the study of spin-polarized systems. We employed the LSD approximation to investigate the possibility of ferromagnetic transitions in double-quantum-well and single-square-well systems. We found that, for a coupled double-quantum-well that shows the excitonic instability studied in Chapter 7, there is also a ferromagnetic transition. An identification of these two instabilities is ruled out on the basis that the ferromagnetic transition occurs at a critical density which is at least an order magnitude smaller than the excitonic critical density. The study of single square wells provides additional evidence in favor of a spin-polarized phase of the electron gas, which would lie between the Wigner crystal phase (at very low density) and the unpolarized quantum liquid (at high density). The critical ferromagnetic density decreases with increasing well width, showing that exchange-correlation effects are stronger in lower dimensions, as expected from purely two- and three-dimensional results.

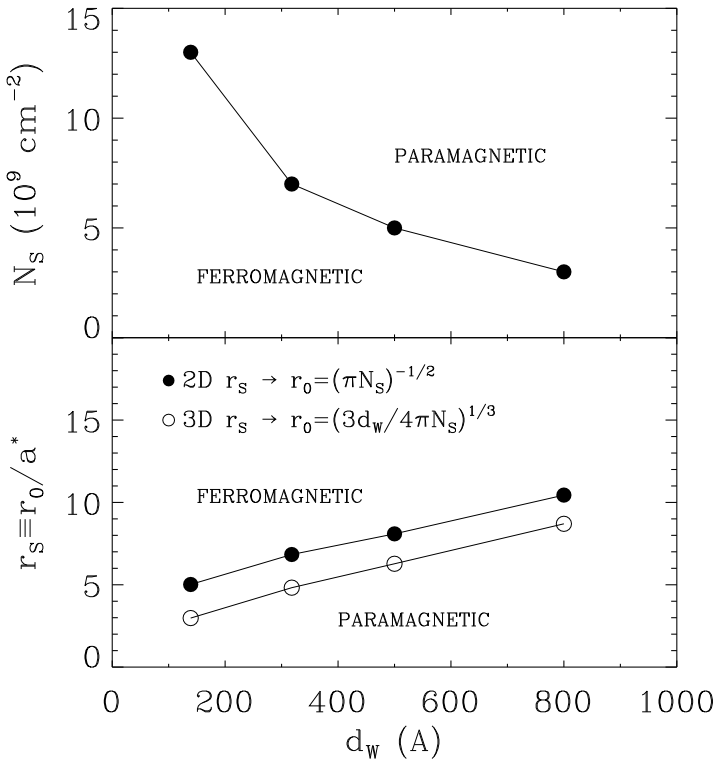

Figure 8.1: Spin-polarization phase diagram of single square wells obtained in the local-spin-density approximation.

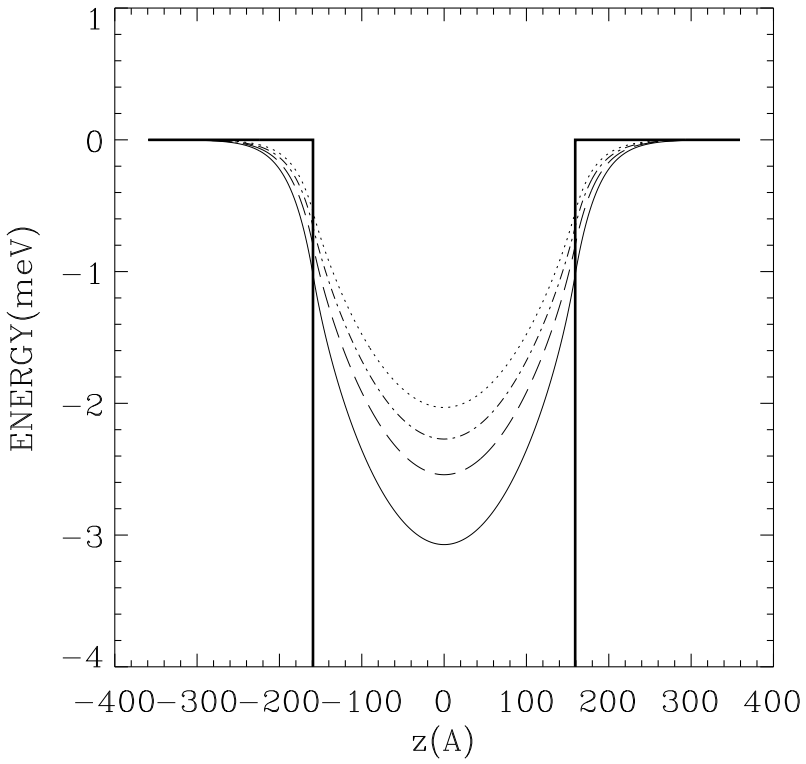

Figure 8.2: Comparison of several exchange-correlation potentials in a single square well sample of width $d_W = 318$Å. The top of the sample potential is shown by thick solid lines. The exchange-correlation potentials are: Das Sarma-Vinter (LSD) (thin solid line), Hedin-Lundqvist (LDA) (dashed line), Ceperley-Alder (LSD) (dash-dotted line), and exchange only (dotted line). The areal density is $N_S = 10^{10}\, cm^{-2}$.

Appendix A

Exchange-correlation potentials

In this Appendix we collect the different parametrizations of the exchange-correlation potentials that we have used in this thesis. We present both the unpolarized potentials, used in the standard local-density-approximation (LDA) calculations, as well as the polarized ones necessary in the local-spin-density (LSD) approximation. The only potentials that have not been given elsewhere in the text are the polarized Gunnarson-Lundqvist (which we have not used but give it here for completeness) and the polarized Ceperley-Alder ones. Ceperley and Alder have used Monte Carlo techniques to calculate the energy of a uniform electron gas over a wide range of densities [46]. The exchange and correlation contributions to these energies have been parametrized by Ceperley [46], and we employ those parametrizations to find the exchange-correlation contribution to the chemical potential of the uniform electron gas, which appears as a potential energy term in the Kohn-Sham equation (see Eqs. (2.4,2.5,8.4). Let us assume that n is the density of a uniform electron gas. We define the interparticle distance r_s and the spin polarization m,

$$r_s = (3/4\pi n)^{1/3}/a_0, \tag{A.1}$$

$$m = (n^+ - n^-)/n. \tag{A.2}$$

In the following we present the different exchange-correlation potentials.

Unpolarized

(1) Hedin-Lundqvist [45]

$$V_{XC}(z) = -\left(\frac{2}{\pi}\right)\left(\frac{9\pi}{4}\right)^{1/3}\frac{1}{r_s}\left(1+0.0368\,r_s\ln\left(1+\frac{21}{r_s}\right)\right) \tag{A.3}$$

(2) Ceperley and Ceperley-Alder [46]

$$V_{XC}(z) = \frac{-1.2145}{r_s} + \gamma\,\frac{\left(1+\frac{7}{6}\beta_1\sqrt{r_s}+\frac{4}{3}\beta_2 r_s\right)}{\left(1+\beta_1\sqrt{r_s}+\beta_2 r_s\right)^2} \tag{A.4}$$

Ceperley: $\gamma = -0.1471$, $\beta_1 = 1.1581$, and $\beta_2 = 0.3446$

Ceperley-Alder: $\gamma = -0.1423$, $\beta_1 = 1.0529$, and $\beta_2 = 0.3334$

Polarized

(1) Gunnarsson-Lundqvist [96]

$$V_{XC}^{\pm}(n(z),m(z)) = -\left(\frac{2}{\pi}\right)\left(\frac{9\pi}{4}\right)^{1/3}\frac{1}{r_s}\left(\beta(r_s)\pm\frac{1}{3}\,\delta(r_s)\,\frac{m}{1\pm 0.297m}\right) \tag{A.5}$$

$$\beta(r_s) = 1+0.0545\,r_s\,ln\left(1+\frac{11.4}{r_s}\right) \tag{A.6}$$

$$\delta(r_s) = 1-0.036\,r_s-\frac{1.36\,r_s}{1+10\,r_s} \tag{A.7}$$

(2) Gunnarsson-Lundqvist modified by Das Sarma-Vinter [97]

$$V_{XC}^{\pm}(n(z),m(z)) = -\left(\frac{2}{\pi}\right)\left(\frac{9\pi}{4}\right)^{1/3}\frac{1}{r_s}\left(\beta(r_s)\pm\frac{1}{3}\,\delta(r_s)\,\frac{m}{1\pm 0.3m}\right) \tag{A.8}$$

$$\beta(r_s) = 1+0.0862\,r_s\,ln\left(1+\frac{15.24}{r_s}\right) \tag{A.9}$$

$$\delta(r_s) = 1-0.0125\,r_s-\frac{0.404\,r_s}{1+0.59\,r_s} \tag{A.10}$$

(3) Ceperley-Alder [46]

$$\epsilon_{xc}^{i} = \frac{c^i}{r_s} + \frac{\gamma^i}{1 + \beta_1^i \sqrt{r_s} + \beta_2^i \, r_s}, \tag{A.11}$$

where $i = U$ (unpolarized, $m = 0$) or $i = P$ (polarized, $m = 1$). The exchange-correlation contribution to the chemical potential is

$$\begin{aligned} V_{xc}^{i} &= (1 - \frac{r_s}{3}\frac{d}{dr_s})\,\epsilon_{xc}^{i} \\ &= \frac{d^i}{r_s} + \gamma^i \, \frac{1 + \frac{7}{6}\,\beta_1^i \sqrt{r_s} + \frac{4}{3}\,\beta_2^i \, r_s}{(1 + \beta_1^i \sqrt{r_s} + \beta_2^i \, r_s)^2} \end{aligned} \tag{A.12}$$

The parameters in the previous expressions, as obtained by Ceperley and Alder [46] are, $c^U = -0.9163$, $c^P = -1.1540$, $d^U = -1.2218$, $d^P = -1.5393$, $\gamma^U = -0.1423$, $\gamma^P = -0.0843$, $\beta_1^U = 1.0529$, $\beta_1^P = 1.3981$, $\beta_2^U = 0.3334$, and $\beta_2^P = 0.2611$. For intermediate polarization (i.e. $0 < m < 1$) we use an interpolation formula proposed by von Barth and Hedin [91], in which the correlation energy has the same polarization dependence as the exchange energy:

$$\begin{aligned} \epsilon_{xc}(r_s, m) &= \epsilon_{xc}^{U}(r_s) + f(m)\left(\epsilon_{xc}^{P}(r_s) - \epsilon_{xc}^{U}(r_s)\right) \\ V_{xc}^{\sigma}(r_s, m) &= V_{xc}^{U}(r_s) + f(m)\left(V_{xc}^{P}(r_s) - V_{xc}^{U}(r_s)\right) + \\ &\qquad \left(\epsilon_{xc}^{P}(r_s) - \epsilon_{xc}^{U}(r_s)\right)(\mathrm{sgn}(\sigma) - m)\,\frac{df}{dm} \end{aligned} \tag{A.13}$$

where

$$f(m) = \frac{(1+m)^{4/3} + (1-m)^{4/3} - 2}{2^{4/3} - 2}. \tag{A.14}$$

In Figs. A.1 and A.2 we compare the various exchange-correlation potentials in the unpolarized ($m = 0$) and polarized ($m = 1$) cases, respectively.

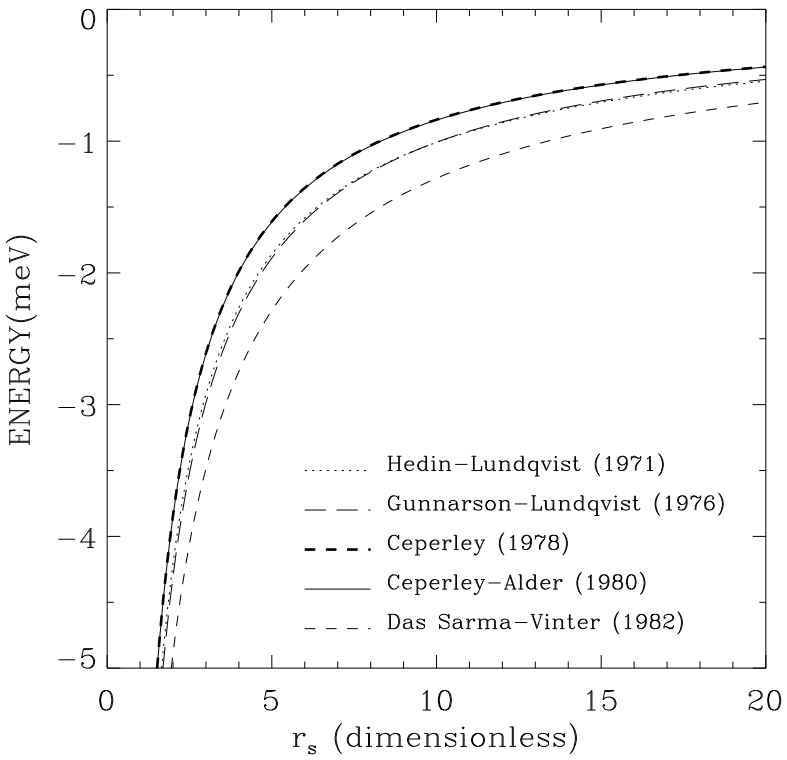

Figure A.1: Comparison of several exchange-correlation potentials in the spin-unpolarized case ($m = 0$).

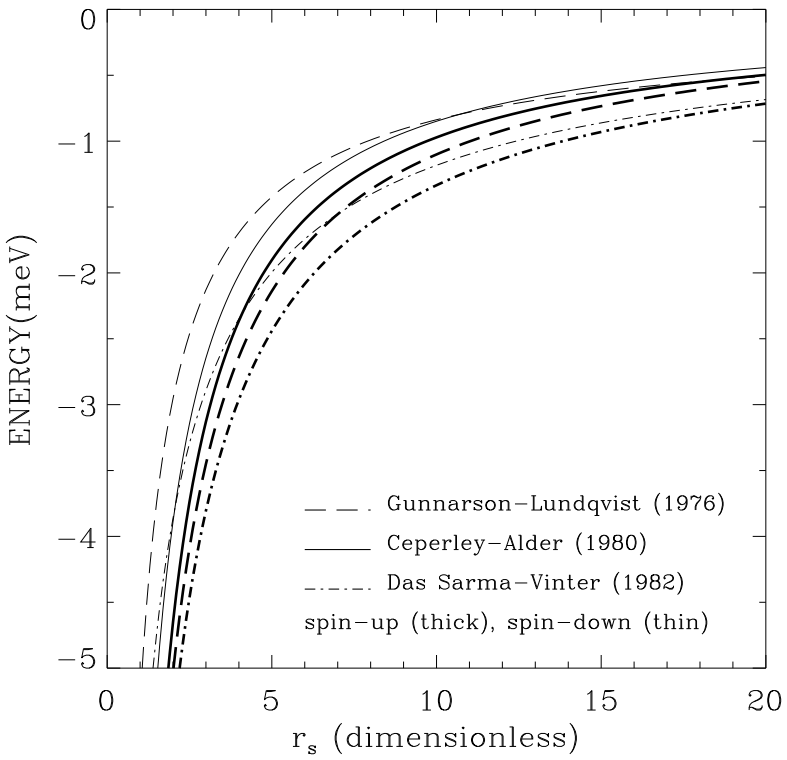

Figure A.2: Comparison of several exchange-correlation potentials in the spin-polarized case ($m = 1$, all spins-up).

Appendix B

Limitations of the Local-Density Approximation

In this Appendix we discuss the validity and limitations of the theoretical techniques employed in this dissertation, i.e. the density-functional theory in the local-density approximation (LDA) and the time-dependent local-density approximation (TDLDA). The LDA is designed to calculate the ground-state of systems with a slowly varying density. Therefore, even though it has been found to work surprisingly well in systems beyond this limit, we first need to determine whether this condition is met in our problem of an electron gas confined in a semiconductor quantum well. The application of density-functional theory to a system with slowly varying density was first analyzed by Hohengerg and Kohn [37]. They showed that an expansion of the energy in terms of the gradient of the electron density $n(\mathbf{r})$ is justified if the relative variations of $n(\mathbf{r})$ over a distance of the order of the inter-electron separation are small,

$$\frac{1}{k_F(n)}\frac{|\nabla n|}{n} \ll 1. \tag{B.1}$$

A more detailed analysis [98, 41] shows that the condition for the corrections to LDA to be small is the weaker one

$$\eta \equiv \frac{1}{6k_F(n)}\frac{|\nabla n|}{n} \approx \frac{1}{18}\frac{|\nabla n|}{n^{4/3}} \ll 1. \tag{B.2}$$

As a test of the applicability of LDA to our problem we computed the quantity η for the double quantum well shown in Fig. 6.1. The result is shown in Fig. B.1. The condition $\eta \ll 1$ is satisfied only in the centers of the individual wells, where the density is maximun and its derivative goes to zero, and it is "weakly" violated ($\eta \approx 2$) near the edges of the wells. Outside the well, where the density is exponentially decaying, and therefore η is exponentially growing (see the third term of Eq. (B.2)) the condition $\eta \ll 1$ is strongly violated. However, since the density in this region is many orders of magnitude smaller than inside the well, this violation of the LDA condition is not expected to give rise to serious errors. Thus, from these considerations we conclude that the use of the LDA to calculate the ground state properties of the electron gas in quantum wells is not strictly justified, but reasonable results can be expected. It would be interesting to employ in future work refined versions of LDA which take into account the rapid variations in density by including higher order terms in the density gradient expansion [98, 41]. However, we reiterate that even though the LDA is not strictly justified in our problem, there is ample evidence that LDA calculations in semiconductor quasi-2D systems, among others, give excellent results when compared with experiment [18, 21]. Therefore, because of these empirical evidence, we consider that our results based on the LDA can be trusted beyond what the above test seems to indicate.

The local-density approximation discussed so far is used to calculate the ground-state properties of inhomogeneous many-body systems. The second important approximation employed in this dissertation has to do with the application of density-functional theory and the local-density approximation to the study of the dynamical response of the electron gas to a time-dependent radi-

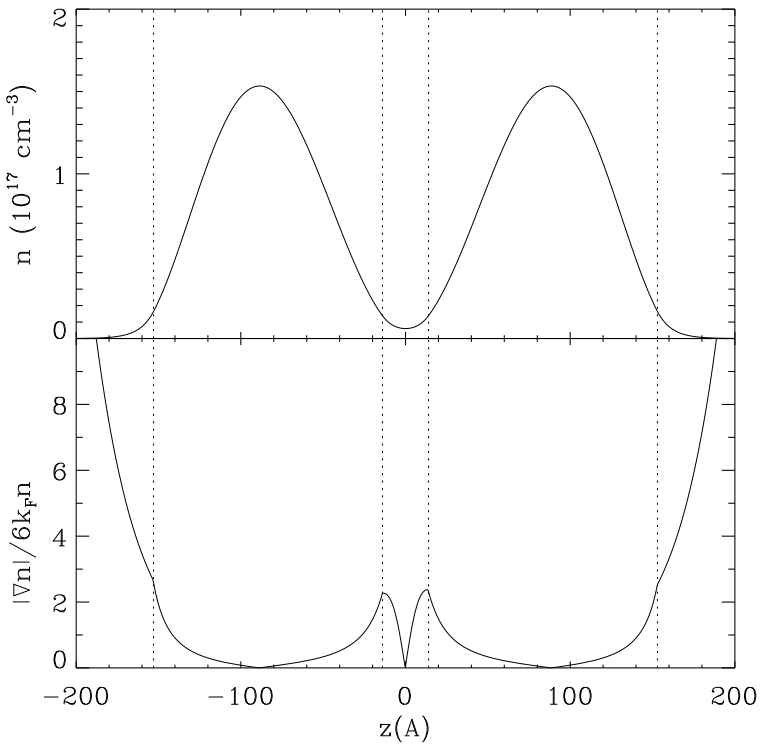

Figure B.1: Top: density profile for the double quantum-well of Fig. 6.1; Bottom: dimensionless parameter $\eta \equiv \frac{1}{6k_F(n)}\frac{|\nabla n|}{n}$ which should be $\eta \ll 1$ for the local-density approximation to be justified. The dashed lines mark the edges of the wells.

ation field. The generalization of the local-density approximation to the time-dependent problem in space-charge layers, the so-called time-dependent local-density approximation (TDLDA), which we use throughout this dissertation was introduced by Ando [40]. This theory, which was explained in detail in Section 2.2 and employed again in Section 5.3, can be expressed in many-body diagramatic language (Fig. B.2), provided the many-body interactions are re-interpreted to reflect the assumptions of the local-density approximation.

The Feynman diagrams associated with the TDLDA are shown in Fig. B.2, and defined and briefly explained in the following quotation from Ref. [27]: "(a) the intersubband leading-order polarizability (gives the quasiparticle continuum); (b) the renormalized subband Green's function with the thin line being the bare Green's function; (c) the self-energy with the leading contributions coming from the Hatree "tadpole" diagram, the "GW" diagram, and the "GWΓ" diagram including the first-order vertex correction; (d) the interacting irreducible intersubband polarizability (gives the collective spin-density excitations) and the ladder series of vertex corrections; (e) the ladder integral equation for the vertex function; and (f) the reducible intersubband polarizability (gives the collective charge-density excitations) as sum of the ring diagrams. The dashed and the wiggly lines are the (unscreened) direct intersubband Coulomb interaction, and the (dynamically screened) exchange-correlation interaction, respectively. (In the TDLDA, one approximates the wiggly line as a static, local interaction.) In the RPA, one neglects all vertex corrections (i.e., uses (a) for the irreducible polarizability) and includes only the Hartree self-energy diagram (the first diagram, the tadpole, in (c))."

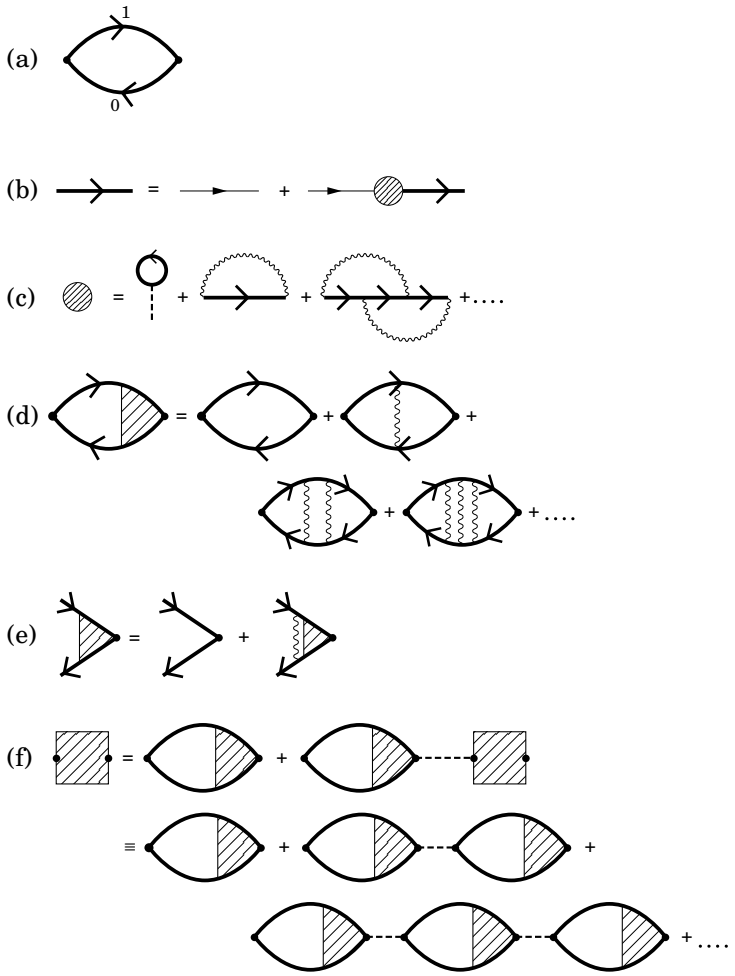

Figure B.2: Many-body diagrams for the intersubband elementary excitations. See the explanations of the different diagrams in the text. (From [27].)

As mentioned in the previous quotation, the TDLDA is an approximate scheme for calculating many-body response functions, which extends the random-phase approximation by including vertex-corrections to the irreducible response function. The TDLDA is equivalent to the ladder diagram approximation provided the exact Coulomb interaction in the vertex correction is replaced by an energy- and momentum-independent interaction, which derives from the static exchange-correlation potential employed in the subband structure determination (see Eq. (5.24). The use of a static and q-independent interaction in not too severe in the ground-state calculation, but it constitutes a more drastic approximation in the dynamic problem. However, it is found that the TDLDA compares favorably with in principle more exact approximation schemes, like the explicit solution of the Bethe-Salpeter equation (which gives the vertex-corrections in the ladder-diagram approximation exactly) performed in the context of semiconductor quantum wells [48].

Our approximation of identifying the excited state energies of the Kohn-Sham equation [38] with the actual quasiparticle energies of the quantum well structure is of course a drastic and uncontrolled approximation which can only be justified if the corresponding many-body self-energy is essentially energy independent [39]. For quasi-two-dimensional structures, in particular silicon inversion layers [93] and GaAs quantum wells [99, 100], the many-body self-energy is found to be very weakly energy dependent, and therefore it is expected that our calculated excitation energies of the Kohn-Sham self-consistent equations approximately correspond to the real excited energies of the system. Explicit comparison between calculated Kohn-Sham excited energies and many-body quasiparticle energies for silicon inversion layers shows this to be the case [93] and therefore we have some

reason to trust this uncontrolled approximation. This situation for the quasi-two-dimensional problem is different from the bulk band gap problem in semiconductors [42] and insulators where the existence of the gap in the excitation spectrum makes things difficult. The fact that there is no gap in the excitation spectrum and that the self-energy is only weakly energy dependent makes LDA and TDLDA reasonable approximations for the excitation spectra in our system. This is borne out by rather detailed agreement between the TDLDA theory and experimental results in semiconductor quantum well structures.

Bibliography

[1] *Quantum Semiconductor Structures*, C. Weisbuch and B. Vinter (Academic Press Inc., 1991), and references therein.

[2] *Wave mechanics applied to semiconductor heterostructures*, by G. Bastard (Les Editions de Physique, Cedex, France, 1988).

[3] R. Dingle, H. L. Störmer, A. C. Gossard and W. Wiegmann, Appl. Phys. Lett. **33**, 665 (1978); H. L. Störmer, J. Phys. Soc. Japan Suppl. A **49**, 1013 (1980).

[4] B. I. Halperin, Jpn. J. Appl. Phys. 26, Suppl. 26-3, 1913 (1987).

[5] M. Sundaram, A. C. Gossard, J. H. English, and R. M. Westervelt, Superlatt. Microstruct. **4**, 683 (1988); E. G. Gwinn, R. M. Westervelt, P. F. Hopkins, A. J. Rimberg, M. Sundaram, and A. C. Gossard, Phys. Rev. B **39**, 6260 (1989); E. G. Gwinn, P. F. Hopkins, A. J. Rimberg, R. M. Westervelt, M. Sundaram, and A. C. Gossard, in *High Magnetic Fields in Semiconductor Physics II.* edited by G. Landwehr (Springer-Verlag, New York, 1989).

[6] M. Shayegan, T. Sajoto, M. Santos, and C. Silvestre, Appl. Phys. Lett. **53**, 791 (1988); T. Sajoto, J. Jo, L. Engel, M. Santos, and M. Shayegan, Phys. Rev. B **39**, 10464 (1989); M. Shayegan, T. Sajoto, J. Jo, M. Santos, and H. D. Drew, *ibid.* **40**, 3476 (1989).

[7] Walter Kohn, Phys. Rev. **123**, 1242 (1961).

[8] L. Brey, N. F. Johnson, and B. Halperin, Phys. Rev. B**40**, 10647 (1989).

[9] Q. P. Li, K. Karrai, S. K. Yip, S. Das Sarma, and H. D. Drew, Phys. Rev. B **43**, 5151 (1991); S. K. Yip, Phys. Rev. B **43**, 1707 (1991).

[10] S. Das Sarma, in *Topics in Condensed Matter Physics*, edited by M. Das (Nova Science, New York, 1993), and references therein.

[11] X. Ying, K. Karrai, H. D. Drew, M. Santos and M. Shayegan, Phys. Rev. B**46**, 1823 (1992).

[12] E. L. Yuh, E. G. Gwinn, P. R. Pinsukanjana, W. L. Schaich, P. F. Hopkins, and A. C. Gossard, Phys. Rev. Lett. **71**, 2126 (1993); E. L. Yuh and E. G. Gwinn, Surf. Sci. **305**, 202 (1994).

[13] W. L. Schaich, Solid State Commun. **88**, 5 (1993).

[14] P. I. Tamborenea and S. Das Sarma, Solid State Commun. **87**, 1009 (1994).

[15] P. I. Tamborenea and S. Das Sarma, Phys. Rev. B **49**, 16593 (1994).

[16] K. Karrai, X. Ying, H. D. Drew, M. Santos, M. Shayegan, S.-R. E. Yang, and A. H. Mac Donald, Phys. Rev. Lett. **67**, 3428 (1991); H. D. Drew, X. Ying, K. Karrai, M. Shayegan and M. Santos, Physica B **184**, 100 (1993).

[17] S. M. Girvin, A. H. MacDonald, and P. M. Platzman, Phys. Rev. B **33**, 2481 (1986).

[18] T. Ando, A. B. Fowler, and F. Stern, Rev. Mod. Phys. **54**, 437 (1982).

[19] *The Physics of the Two-Dimensional Electron Gas*, edited by J. T. Devreese and F. M. Peeters (Plenum, New York, 1987).

[20] T. Ando, Surf. Sci. **58**, 128 (1976); T. Ando, Phys. Rev. B **13**, 3468 (1976).

[21] F. Stern and S. Das Sarma, Phys. Rev. B **30**, 840 (1984).

[22] W. B. Chen, Y. J. Chen, and E. Burstein, Surf. Sci. **58**, 263 (1976).

[23] S. J. Allen, D. C. Tsui, and B. Vinter, Solid State Commun. **20**, 425 (1976).

[24] D. A. Dahl and L. J. Sham, Phys. Rev. B **16**, 651 (1977).

[25] *Quantum Theory of Many-Particle Systems*, A. L. Fetter and J. D. Walecka (McGraw-Hill Book Company, 1971).

[26] *Many-Particle Physics*, G. Mahan (Plenum Press, New York and London, 1981).

[27] S. Das Sarma and I. K. Marmorkos, Phys. Rev. B **47**, 16343 (1993); I. K. Marmorkos and S. Das Sarma, Phys. Rev. B **48**, 1544 (1993).

[28] T. Ando, J. Phys. Soc. Jpn. **51**, 3893 (1982).

[29] S. Katayama and T. Ando, *ibid.*, **54**, 1615 (1985).

[30] A. Pinczuk, S. Schmitt-Rink, G. Danan, J. P. Valladares, L. N. Pfeiffer, and K. W. West, Phys. Rev. Lett. **63**, 1633 (1989).

[31] S. Ernst, A. R. Goñi, K. Syassen, and K. Eberl, Phys. Rev. Lett. **72**, 4029 (1994).

[32] R. Decca, A. Pinczuk, S. Das Sarma, B. S. Dennis, L. N. Pfeiffer, and K. W. West, Phys. Rev. Lett. **72**, 1506 (1994); R. Decca, A. Pinczuk (unpublished, private communication).

[33] P. I. Tamborenea and S. Das Sarma, Phys. Rev. B **49**, 16821 (1994).

[34] S. Das Sarma and P. I. Tamborenea, Phys. Rev. Lett. **73**, 1971 (1994).

[35] A. Pinczuk, private communication.

[36] L. H. Thomas, Proc. Cambridge Phil. Soc. **23**, 542 (1927); E. Fermi, Rend. Accad. Naz. Linzei **6**, 602 (1927); Z. Phys. **48**, 73 (1928).

[37] P. Hohenberg and W. Kohn, Phys. Rev. **136**, B864 (1964).

[38] W. Kohn and L. J. Sham, Phys. Rev. **140**, A1133 (1965).

[39] L. J. Sham and W. Kohn, Phys. Rev. **145** 561 (1966).

[40] T. Ando, Solid State Commun. **21**, 133 (1977); T. Ando, Z. Phys. B**26**, 263 (1977).

[41] R. O. Jones and O. Gunnarsson, Rev. Mod. Phys. **61**, 689 (1989); A. R. Williams and U. von Barth, in *Theory of the inhomogeneous Electron Gas*, edited by S. Lundqvist and N. H. March (Plenum, New York, 1983).

[42] *Density Functional Theory*, R. M. Dreizler and E. K. U. Gross (Springer-Verlag, 1990).

[43] W. G. Teich and G. Mahler, Phys. Status Solidi (b), **138**, 607 (1986).

[44] M. P. Stopa and S. Das Sarma, Phys. Rev. B **47**, 2122 (1993).

[45] L. Hedin and B. I. Lunqvist, J. Phys. C **4**, 2064 (1971).

[46] D. M. Ceperley, Phys. Rev. B **18**, 3126 (1978); D. M. Ceperley and B. J. Alder, Phys. Rev. Lett. **45**, 566 (1980); J. Perdew and A. Zunger, Phys. Rev. B **23**, 5048 (1981).

[47] *Computational physics*, by Steven E. Koonin (The Benjamin/Cummings Pub. Co., Menlo Park, California, 1986); *Numerical recipes*, by W. H. Press, S. A. Teukolsky, W. T. Vetterling, and B. P. Flannery (Cambridge University Press, Cambridge, 1992).

[48] S. L. Chuang, M. S. C. Luo, S. Schmitt-Rink, and A. Pinczuk, Phys. Rev. B **46**, 1897 (1992).

[49] T. Ando and S. Mori, J. Phys. Soc. Jpn. **47**, 1518 (1979);

[50] L. Brey, Jed Dempsey, N. F. Johnson, and B. I. Halperin, Phys. Rev. B**42**, 1240 (1990); L. Brey, N. F. Johnson, and Jed Dempsey, *ibid.*, **42**, 2886 (1990).

[51] M. P. Stopa and S. Das Sarma, Phys. Rev. B **45**, 8526 (1992).

[52] A. Kamgar, P. Kneschaurek, G. Dorda, Phys. Rev. Lett. **32**, 1251 (1974); A. Kamgar, P. Kneschaurek, W. Beinvogl, J. F. Koch, Proc. 12th Int. Conf. Semic. Phys. pp. 709-713, Stuttgart, B. G. Teubner (1974); P. Kneschaurek, A. Kamgar, J. F. Koch, Phys. Rev. B **14**, 1610 (1976).

[53] A. Tselis and J. J. Quinn, Surf. Sci. **113**, 362 (1982); K. S. Yi and J. J. Quinn, Phys. Rev. B **27**, 1184 (1983); **27**, 2396 (1983).

[54] T. Ando, J. Phys. Soc. Jpn. **39**, 411 (1975).

[55] T. Ando, J. Phys. Soc. Jpn. **44**, 475 (1978).

[56] Jed Dempsey, and B. I. Halperin, Phys. Rev. B**47**, 4674 (1993).

[57] A. Wixforth, M. Sundaram, J. H. English, and A. C. Gossard, in *Proceedings of the 20th International Conference on the Physics of Semiconductors*,

edited by E. M. Anastassakis and J. D. Joannopoulos (World Scientific, Singapore, 1990), p. 1705.

[58] Jed Dempsey, and B. I. Halperin, Phys. Rev. B**45**, 3902 (1992); **47**, 4662 (1993).

[59] L. I. Magarill and A. V. Chaplik, Pis'ma Zh. Eksp. Teor. Fiz. **40**, 301 (1984) [JETP Lett. **40**, 1089 (1984)].

[60] H. D. Drew, private communication.

[61] Jed Dempsey, and B. I. Halperin, Phys. Rev. B**45**, 1719 (1992).

[62] Norman J. Horing, Ann. Phys. **31**, 1-63 (1965); M. J. Stephen, Phys. Rev. **129**, 997 (1963).

[63] *Waves and Interactions in Solid State Plasmas*, P. M. Platzman and P. A. Wolff (Academic Press, New York and London, 1973).

[64] *Quantum Theory of Solids*, C. Kittel, second revised edition (John Wiley & Sons, 1987).

[65] D. C. Hamilton and A. L. McWhorther, in *Proc. Int. Conf. Light Scattering Spectra Solids*, p. 309 (Springer-Verlag, Berlin, New York, 1969).

[66] A. Pinczuk and G. Abstreiter, in *Light Scattering in Solids V*, edited by M. Cardona and G. Guntherodt (Springer-Verlag, Berlin, 1989), and references therein.

[67] G. Abstreiter, M. Cardona, and A. Pinczuk, in *Light Scattering in Solids IV*, edited by M. Cardona and G. Güntherodt (Springer, Berlin, Heidelberg, New York, 1984).

[68] M. V. Klein, in *Light Scattering in Solids I*, edited by M. Cardona (Springer, Berlin, Heidelberg, New York, 1983).

[69] S. S. Jha, Nuovo Cimento **58** B, 331 (1969).

[70] F. A. Blum, Phys. Rev. B **1**, 1125 (1970).

[71] A. Pinczuk and E. Burstein, in *Light Scattering in Solids I*, edited by M. Cardona (Springer, Berlin, Heidelberg, New York, 1983).

[72] S. Das Sarma, in *Light Scattering in Semiconductor Structures and Superlattices*, edited by D. J. Lockwood and J. F. Young (Plenum Press, New York, 1991) and references therein.

[73] Jainendra K. Jain and S. Das Sarma, Phys. Rev. B **36**, 5949 (1987);

[74] D. Gammon, B. V. Shanabrook, J. C. Ryan, D. S. Katzer, and M. J. Young, Phys. Rev. Lett. **68**, 1884 (1992); D. Gammon, B. V. Shanabrook, J. C. Ryan, D. S. Katzer, Phys. Rev. B **41**, 12311 (1990).

[75] D. C. Tsui, H. L. Störmer, and A. C. Gossard, Phys. Rev. Lett. **48**, 1559 (1982).

[76] R. B. Laughlin, Phys. Rev. Lett. **50**, 1395 (1983).

[77] R. J. Price, P. M. Platzman, and Song He, Phys. Rev. Lett. **70**, 339 (1993).

[78] B. I. Halperin, P. A. Lee, and N. Read, Phys. Rev. B **47**, 7312 (1993).

[79] S. He, S. Das Sarma, and X. C. Xie, Phys. Rev. B **47**, 4394 (1993), and references therein.

[80] G. Boebinger *et. al.*, Phys. Rev. Lett. **64**, 1793 (1990).

[81] J. P. Eisenstein *et. al.*, Phys. Rev. Lett. **68**, 1383 (1992); Y. W. Suen *et. al.*, Phys. Rev. Lett. **68**, 1379 (1992).

[82] H. A. Fertig, Phys. Rev. B **40**, 1087 (1989); A. H. MacDonald, P. M. Platzman, and G. S. Boebinger, Phys. Rev. Lett. **65**, 775 (1990); L. Brey, Phys. Rev. Lett. **65**, 903 (1990); X. Chen and J. J. Quinn, Phys. Rev. Lett. **67**, 895 (1991); S. He *et. al.*, Phys. Rev. B **43**, 9339 (1991).

[83] S. Das Sarma and A. Madhukar, Phys. Rev. B **23**, 805 (1981).

[84] D. Neilson *et. al.*, Phys. Rev. Lett. **71**, 4035 (1993); L. Swierkowski *et. al.*, Phys. Rev. Lett. **67**, 240 (1991); P. P. Ruden and Z. Wu, Appl. Phys. Lett. **59**, 2165 (1991).

[85] B. Tanatar and D. M. Ceperley, Phys. Rev. B **39**, 5005 (1989).

[86] We can obtain a crude estimate of the upper limit to the transition temperature T_c by putting $k_B T_c \approx \Delta_{SAS}$, which makes our theory meaningful only for $T \ll T_c \approx \Delta_{SAS}/k_B$. For $T \approx 1 - 4K$, this restricts $d_B < 45 - 50$Å.

[87] A. R. Williams and U. von Barth, in *Theory of the Inhomogeneous Electron Gas*, edited by S. Lundqvist and N. H. March (Plenum, New York, 1983).

[88] E. P. Wigner, Phys. Rev. **46**, 1002 (1934).

[89] F. Bloch, Z. Phys. **57**, 549 (1929).

[90] S. F. Edwards and A. J. Hillel, J. Phys. C **1**, 61 (1968); A. W. Overhauser, Phys. Rev. Lett. **3**, 414 (1959); Phys. Rev. Lett. **4**, 462 (1960); Phys. Rev. **128**, 1437 (1962).

[91] U. von Barth and L. Hedin, J. Phys. C**5**, 1629 (1972).

[92] M. M. Pant and A. K. Rajagopal, Solid State Commun. **10**, 1157 (1972).

[93] S. Das Sarma and B. Vinter, Phys. Rev. B **26**, 960 (1982); *ibid.* **28**, 3639 (1983).

[94] D. M. Ceperley, private communication.

[95] C. E. Hembree, B. A. Mason, J. T. Kwiatkowski, J. Furneaux, and J. A. Slinkman, Phys. Rev. B **48**, 9162 (1993).

[96] O. Gunnarsson and B. I. Lundqvist, Phys. Rev. B **13**, 4274 (1976).

[97] S. Das Sarma and B. Vinter, unpublished.

[98] D. C. Langreth and M. J. Mehl, Phys. Rev. B **28**, 1809 (1983).

[99] R. Jalabert and S. Das Sarma, Phys. Rev. B **40**, 9723 (1989).

[100] I. K. Marmorkos and S. Das Sarma, Phys. Rev. B **44**, 3451 (1991).